PSFC/RR-01-2 **DOE-ET-54512-339**

Phase Contrast Imaging on the Alcator C-Mod Tokamak

A. Mazurenko

July 2001

Plasma Science and Fusion Center
Massachusetts Institute of Technology
Cambridge, MA 02139 USA

This work was supported by the U.S. Department of Energy, Cooperative Grant No. DE-FC02-99ER54512. Reproduction, translation, publication, use and disposal, in whole or in part, by or for the United States government is permitted.

Phase Contrast Imaging on the Alcator C-Mod tokamak

by

Alexander Mazurenko

B.S.(1992), M.S.(1993), Department of General & Applied Physics,
Moscow Institute of Physics & Technology

Submitted to the Department of Physics
in partial fulfillment of the requirements for the degree of

Doctor of Philosophy

at the

MASSACHUSETTS INSTITUTE OF TECHNOLOGY

September 2001

Author .....
Department of Physics
July 11, 2001

Certified by .....
Miklos Porkolab
Professor of Physics
Thesis Supervisor

Accepted by .....
Thomas J. Greytak
Professor of Physics, Associate Department Head for Education

Phase Contrast Imaging on the Alcator C-Mod tokamak

by

Alexander Mazurenko

Submitted to the Department of Physics
on July 11, 2001, in partial fulfillment of the
requirements for the degree of
Doctor of Philosophy

Abstract

Phase Contrast Imaging (PCI) is a new diagnostic that was built for the Alcator C-Mod tokamak. It measures line-integrated (along 12 vertical chords) plasma density perturbations with good temporal (2-500 kHz) and wavenumber (0.5-12 /cm) resolution.

The Quasi-Coherent (QC) fluctuation mode was studied using the PCI and other diagnostics. The mode was found to cause fluctuation of density, electric and magnetic field in the plasma edge with typical frequency of 100 kHz and typical poloidal wavenumber of about 5/cm. The mode was found to be responsible for confinement properties of the "Enhanced D-alpha H-mode" (a particularly favorable regime of tokamak operation). Through numerical modeling, the physical origin of the fluctuations was tentatively identified as "resistive X-point" mode (a kind of resistive ballooning mode strongly affected by the X-point configuration of magnetic field lines).

The PCI system has been upgraded to detect waves in the ion cyclotron range of frequencies (ICRF, 40-80 MHz) by means of optical heterodyning – a technique based on modulation of the diagnostic laser beam near the wave frequency. The upgraded system was then used to study propagation of the Fast Magnetosonic Waves. These waves, which have never been measured in detail in past experiments, are being used to heat the tokamak plasma at the megawatt power level. The measured results were compared to the simple cold-plasma dispersion relation and to predictions of the full-wave 3D numerical modeling.

Thesis Supervisor: Miklos Porkolab
Title: Professor of Physics

Acknowledgments

I would like to thank all the people who helped me, directly or indirectly, to complete this thesis. I will do my best to acknowledge as many of them as I can.

First, it is my pleasure to thank my thesis and research advisor, Prof. Miklos Porkolab, for continuously supporting me throughout my years at MIT. I appreciate all the guidance and instruction that I received from him but also the considerable amount of freedom that he allowed me in doing this research. I especially admire his dedication to standing by his students, which made this thesis possible.

I thank all the hard-working scientists and technicians in the Alcator C-Mod group for helping me with my research, namely Steve Wukitch, Paul Bonoli, Dmitri Mossessian, Martin Greenwald, Jim Irby, Réjean Boivin, Amanda Hubbard, Joe Snipes, Steve Wolfe, Earl Marmar, Rick Murray, Joe Bosco, Yuri Rokhman, Jim Rosati and all the others. Special thanks to Yuichi Takase, who introduced me to C-Mod.

Many thanks to the people outside the MIT, who contributed to this thesis research: Gary Hallock, Romik Chatterjee and Ashley Shugart of the University of Texas at Austin; Xueqiao Xu and Bill Nevins of the Lawrence Livermore National laboratory; Stefano Coda and Henry Weisen of CRPP, Switzerland.

I would like to thank my thesis readers, Profs. Ambrogio Fasoli and George Benedek, for their comments and suggestions.

To all current and former graduate students that I have met here during our time together in the C-Mod group, namely Eric Nelson-Melby, Maxim Umansky, Jim Reardon, Peter O'Shea, Chris Rost, Kirill Zhurovich, Yijun Lin, Sanjay Gangadhara, Howard Yuh, Thomas Jennings, Rob Nachtrieb and many others: Thanks for friendship and fruitful discussions, all the best for you and your families, and good luck with you future studies and professional lives.

To all tax-paying people in the US, thanks for supporting the fusion program and for making my education at MIT possible.

Finally, sincere thanks to my parents, who always supported my passion for science, and to my fiancé, Olga, whose love and understanding inspire me in my work.

Contents

List of Figures

List of Tables

Chapter 1

Introduction

The goal of this introductory chapter is to familiarize the reader with the basic concepts of fusion science and plasma physics and confinement. The most progress in this field was achieved in *tokamaks*[1] (torus shaped magnetic devices), so a short introduction will be given to the tokamak design, and specifically to Alcator C-Mod.

This thesis is based on the research made using a new Phase Contrast Imaging (PCI) diagnostic. This diagnostic was recently installed on C-Mod and it is capable of measuring the electron density fluctuations with earlier unavailable speed and precision. Motivations for building this diagnostic will also be discussed in the chapter.

1.1 Why Do We Need Plasma Fusion?

Most energy experts agree that, as world energy consumption continues to grow, oil, coal and natural gas will either become too scarce or too polluting to rely upon after the next few decades. The demand for the world energy use, currently at 15 Terawatts, is predicted to triple by the year 2050, and only about half of this demand is expected to be met by burning conventional fossil fuels [4]. Using renewable energy sources (such as solar or water energy, etc.) cannot be relied upon either, since it is unlikely to satisfy the significant energy demand.

[1] Tokamak – a Russian acronym for *to(roidal'naya) kam(era s) ak(sial'nym magnitnym polem)* – a toroidal chamber with an axial magnetic field[3].

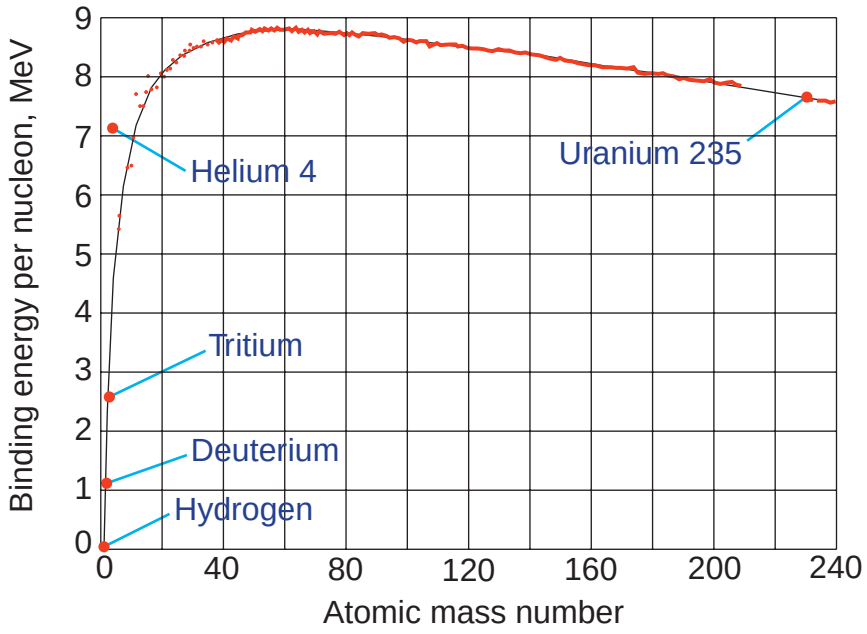

Figure 1-1: Binding energy per nucleon as a function of atomic mass number.

This leaves only the energy sources based on nuclear reactions (such fission and fusion) to supply the needed power. Since the binding energy per nucleon of very light or very heavy elements is smaller then that of the rest (Fig. 1-1), energy may be released when these elements transform into medium weight ones [5]. The process of splitting heavy atoms (typically uranium or plutonium) is called fission, and fusing lighter nuclei together is called fusion. It is fusion of deuterium that powers the sun and other stars in our universe.

Fission based powerplants are already widely acceptable, providing significant fraction of electricity of industrialized nations. However, there are drawbacks to using fission power, such as a risk of meltdowns or accidents and complicated disposal of nuclear waste. The heavy and medium weight isotopes, which are byproducts of fission, are highly radioactive and will stay so for many thousands of years. Fusion, on the other hand, will produce only small amounts of mostly short lived isotopes. Based on the most meaningful indices combining volume, radiotoxicity, and longevity, the fusion produced radioactive waste hazards can be expected to be at least 100 times and perhaps as much as 10,000 (or more) times smaller than those of fission [6]. Furthermore, fusion reactions are difficult to sustain, so any plant malfunction would

result ia a shutdown, rather than a meltdown.

1.1.1 Magnetic Confinement

Two reactions suggested for use in a fusion powerplant are

$$\mathrm{D} + \mathrm{T} \;\rightarrow\; {}^{4}\mathrm{He}(3.5\ MeV) + \mathrm{n}(14.1\ MeV)\ , \tag{1.1}$$

$$\mathrm{D} + \mathrm{D} \;\rightarrow\; {}^{3}\mathrm{He}(0.82\ MeV) + \mathrm{n}(2.45\ MeV)\ , \tag{1.2}$$

where D and T stand for two hydrogen isotopes: Deuterium (^{2}H) and Tritium (^{3}H). Unfortunately, at normal temperature the coulomb forces prevent hydrogen nuclei from getting sufficiently close to each other in order to fuse. The reaction rate becomes large enough to produce self-sustained "burning" only at temperatures at least 5 keV (about 50 million degrees K) or more. Under these condition atoms of any element become completely ionized and the medium becomes an ionized gas, or *plasma*.

To prevent contamination of the fusing plasma, it is usually formed inside a vacuum chamber which is pumped to low initial pressures before the fuel (deuterium and/ot tritium) is introduced in a solid or gaseous form. Some confinement mechanism is needed to contain the sufficiently dense hot plasma for the time long enough to produce a reasonable amount of fusion power so the burn may become self-sustaining. In the sun, a natural fusion reactor, such mechanism is provided by gravity. Here on earth, there are currently only two possibilities, namely *inertial* and *magnetic* confinement. In inertial confinement, some amount of hydrogen is imploded, typically by radiation from multiple intense laser beams, and fusion reactions may occur in sufficient quantity before the plasma expands and cools. This approach, however, is not well suited for operation in a powerplant, primarily due to its currently low yield, slow repetition rate and short lifespan of the lasers and optics.

Magnetic confinement of hot plasma, on the other hand, has a much better potential for steady state operation in a fusion reactor. This scheme is based on the property of charged particles to follow spiral paths around magnetic field lines. In a

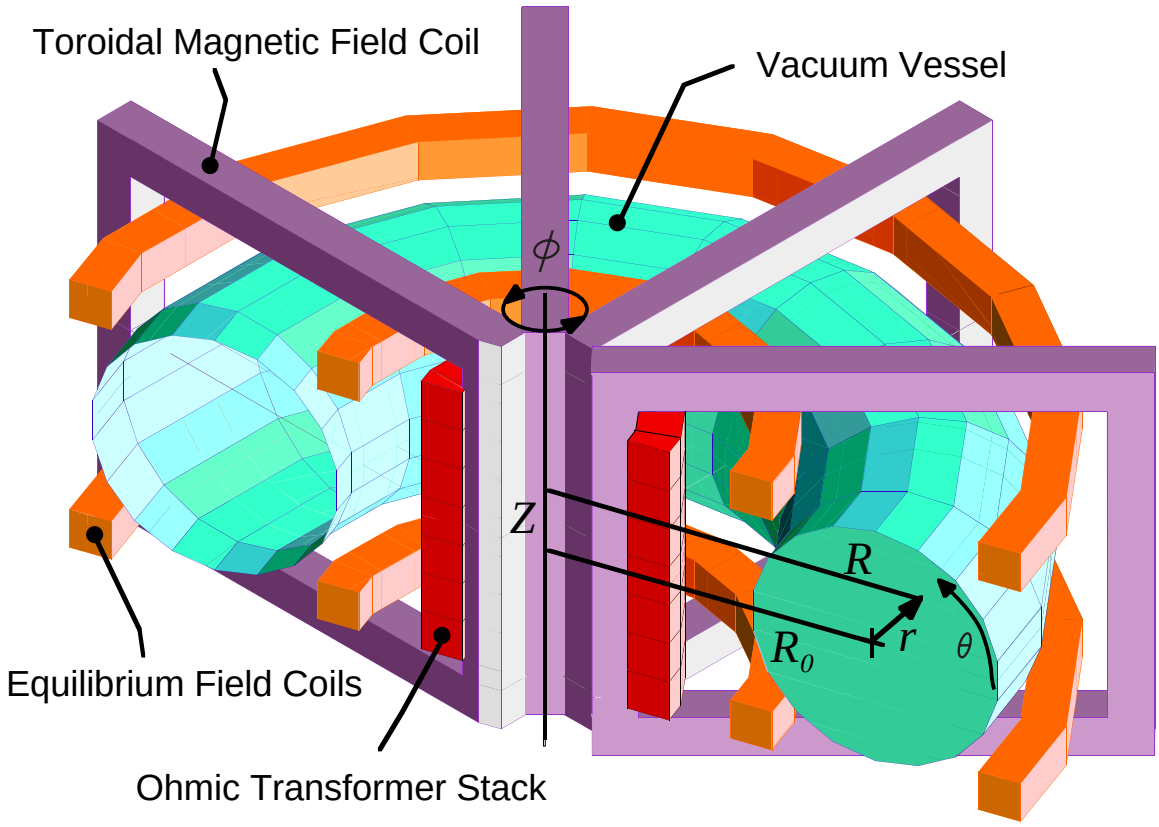

Figure 1-2: Schematic of principle components of a tokamak.

configuration where these lines never intersect the container walls, in principle, the plasma would be confined. However, there are various "drift"- (slow gyrating movements across the field lines), instability- and collision-based mechanisms that tend to diffuse particles and heat towards the chamber walls. Reducing the diffusion rate is an important role of present research and this constitutes the physics of magnetic confinement.

1.1.2 Tokamaks

Up to date, the best confinement was achieved in devices called *tokamaks* (an acronym from the Russian language, where is stands for "a toroidal chamber with an axial magnetic field"). The design of a generic tokamak is shown in Fig. 1-2. In the center of such a device there is a torus-shaped vacuum vessel containing hydrogen plasma. A set of coils creates a toroidal (i.e. along $\hat{\phi}$) magnetic field. To prevent a certain kind

of instabilities, a toroidal current must always be presents in the plasma. One of the ways to drive this current is by means of a center mounted transformer. When the current is gradually raised in the primary winding of this transformer, an electrical field is created along $\hat{\phi}$ and it drives the needed toroidal current in the plasma, which in this case serves as a secondary winding.

The presence of plasma current creates additional poloidal (i.e. along $\hat{\theta}$) magnetic field. This results in that the magnetic field lines are no longer closed. Rather, they loop continuously on what is called "flux" surfaces (a set of torus-like surfaces nested inside the vacuum vessel and each other). Since charged particles can move unrestricted along the magnetic field lines, plasma properties are usually the same everywhere on a single flux surface.

In terms of the power efficiency, the performance of a tokamak (or any other fusion device) can be expressed by means of Lawson model[7]. The power balance equation is

$$\frac{dW}{dt} = P_{fusion} + P_{heating} - P_{Bremsstrahlung} - P_{transport} \ , \tag{1.3}$$

$$P_{fusion}/P_{heating} \equiv Q \ , \tag{1.4}$$

where W represents the total energy of the plasma. Fusion generated alpha particles, as well as external heating are trying to increase W, while losses due to Bremsstrahlung radiation and energy transport reduce it. The transport losses are often expressed in terms of the energy replacement (confinement) time τ_E and the total plasma kinetic energy

$$P_{transport} = W_{kinetic}/\tau_E \ . \tag{1.5}$$

The dependencies of the fusion power rate and the Bremsstrahlung radiation are well known, and the equation for the power balance can be rearranged to be solved for $n\tau_E$ as a function of only temperature, Q and dW/dt. The goal for a fusion reactor would be to operate in steady state ($dW/dw = 0$) and to ignite ($Q = \infty$). For the 50-50 deuterium-tritium plasma mix, this would require $n\tau_E \approx 2 - 3 \times 10^{20}$ m^{-3}s at

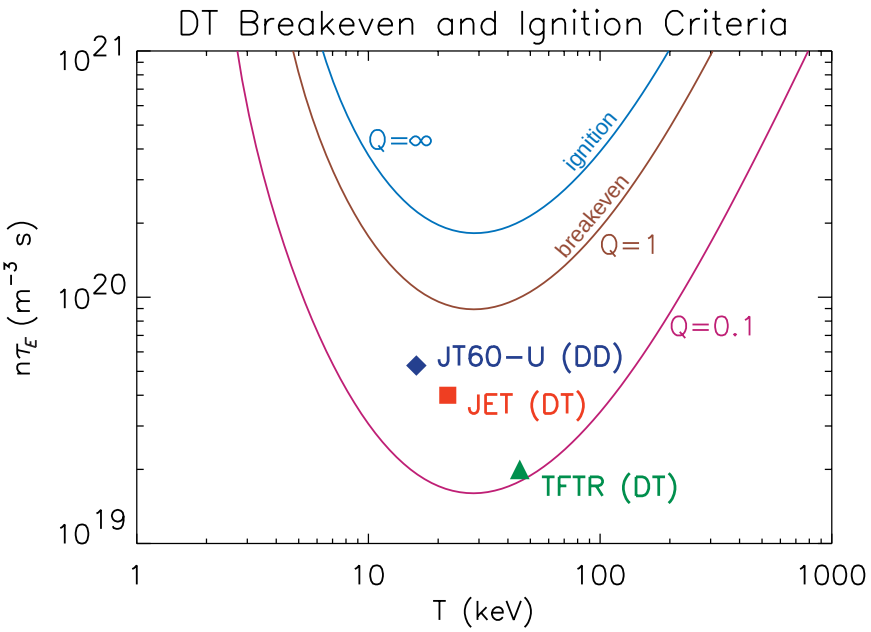

Figure 1-3: Lawson parameter $n\tau_E$ as a function of plasma temperature for different values of $Q \equiv P_{fusion}/P_{heating}$. "Breakeven" is defined as $Q = 1$; "ignition" is defined as $Q = \infty$.

some optimal temperature of $T \approx 10 - 30$ keV. It should be noted, that at other temperatures the reactor would be less effective, as can be seen in Fig. 1-3. At lower temperatures the fusion rate is just too low, and at higher temperatures the Bremsstrahlung losses become too high while the fusion rate does not increase. A significant milestone in the progress of fusion research would be reaching "breakeven", when the fusion power produced matches the external heating and $Q = 1$. Although as of this writing no fusion reactor has reached the breakeven yet, the goal is very close, as can be seen from the record values of $n\tau_E$ achieved in actual tokamak experiments, also shown in Fig. 1-3.

1.1.3 Alcator C-Mod

Alcator C-Mod, the third high-field compact tokamak in the Alcator line, has been operating at the MIT Plasma Science & Fusion Center since May 1993 [8]. Its major parameters are given in Table 1.1. Figures 1-4 and 1-5 illustrate the tokamak cross-section and conceptual drawing. All the coils used in the device are conventional

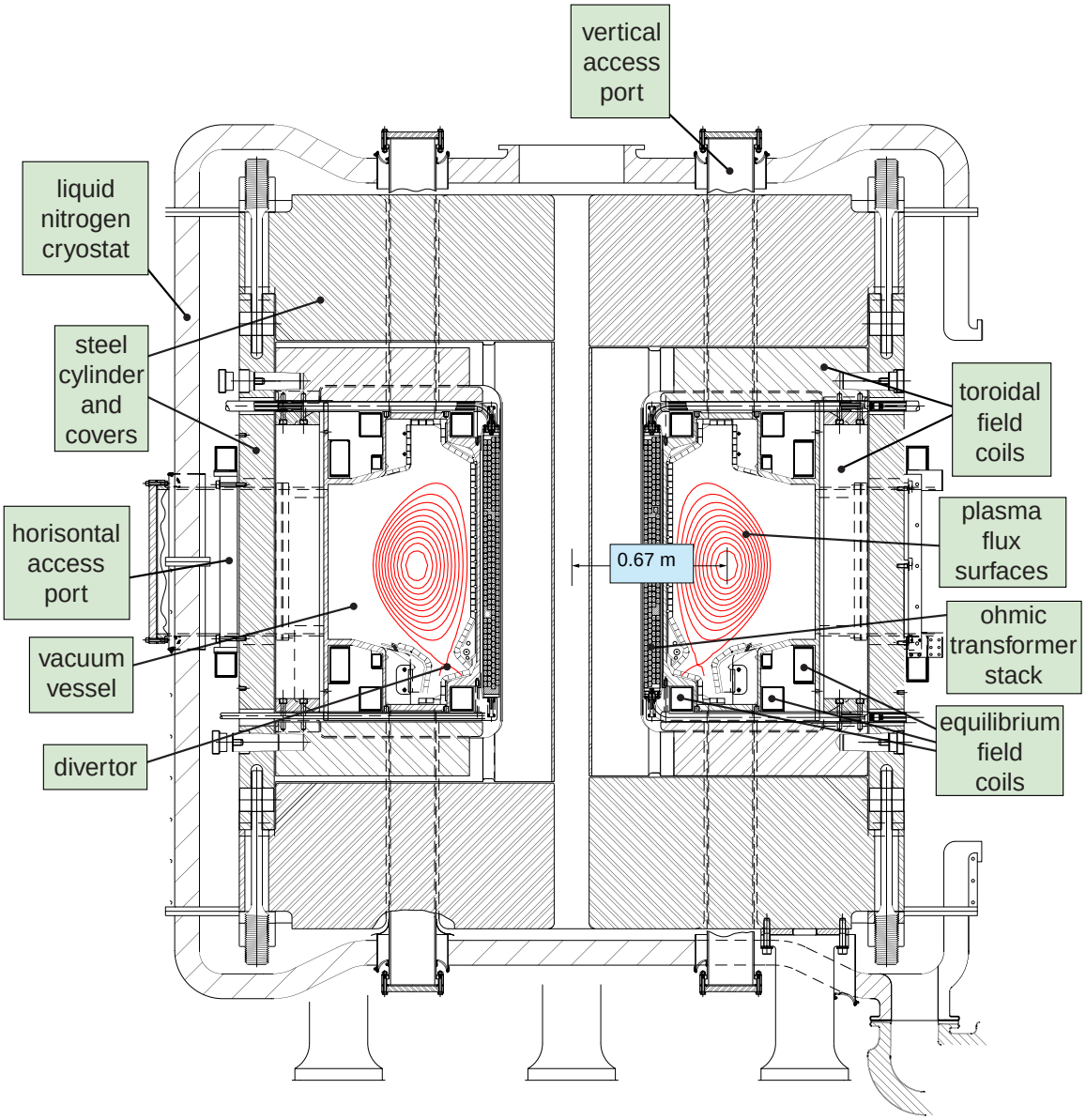

Figure 1-4: Poloidal cross-section of the Alcator C-Mod tokamak.

Major radius, R	0.67 m	
Minor radius, a	0.21 m	
Pulse duration	2 sec	
Time between pulses	15 minutes	
Toroidal magnetic field, B_t	5 T typical	8.1 T max
Plasma current, I_p	800 kA typical	1.5 MA max
Core electron density, n_e	2×10^{20} m^{-3} typical	6×10^{20} m^{-3} max
Core electron temperature, T_e	2 keV typical	5 keV max
Ohmic heating power		1.5 MW max
ICRF heating power		5 MW max
Plasma shape, elongation κ	1.6	
Plasma shape, triangularity δ	0.4	

Table 1.1: Major operation parameters of the Alcator C-Mod tokamak.

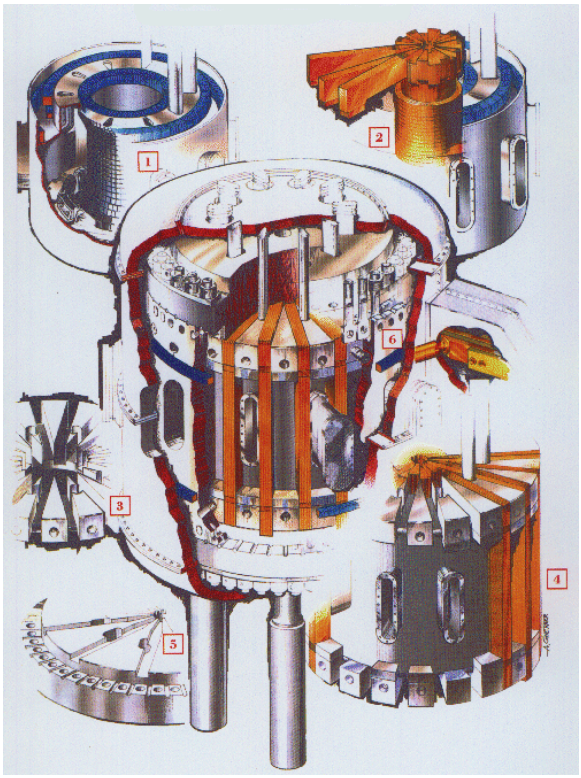

Figure 1-5: Conceptual drawing of the Alcator C-Mod tokamak.

(not superconducting) and therefore require large amounts of power (220 MW) to operate. This way the machine may only be operated in pulses. The frequency and duration of the pulses is determined by the coil heating and cooling rates and by the flywheel alternator spin-up time.

The primary source of plasma heating in C-Mod is the ICRF (ion cyclotron range of frequencies) waves, launched by the three wall mounted antennas. Ohmic heating due to the plasma current and finite resistivity also provides a substantial amount of heating power. In the next few years, these two systems are scheduled by be supplemented by a new "lower-hybrid" microwave source.

Alcator C-Mod offers reasonable port access for plasma diagnostic purposes. There are total of 10 side ports and 20 vertical access ports (see Fig. 1-4). Virtually any parameter of the plasma is measured, some by more than one diagnostic. Density profiles, for example, are reconstructed from the results of two-color interferometry, reflectometry, Thompson scattering and scanning Langmuir diagnostics. Usually, different systems provide different range, time and space resolution and work to complement each other.

Alcator C-Mod represents a newer generation of the so called "diverted" tokamaks. The outer flux surfaces in such a tokamak are open and do intersect the vessel walls. The plasma particles that diffuse through the last closed flux surface (called *separatrix*) then end up in the "divertor" (the partially enclosed small volume part of the vacuum vessel that may be pumped). Such design helps to reduce the amount of impurities that accumulate in plasma and increase radiative losses.

1.2 Motivation

For this thesis a unique diagnostic, namely *Phase Contrast Imaging* (PCI), was developed to provide non-perturbing measurements of plasma density fluctuations. The way this diagnostic is implemented on the Alcator C-Mod tokamak allows it to detect both long ($\sim$10 cm) and relatively short ($\sim$0.5 cm) fluctuations coming from almost anywhere in the plasma (core and edge). Measurements both at low ($<$500 kHz) and

high (40-80 MHz, heterodyned) frequencies are possible.

Such wide capabilities of the diagnostic allow ample opportunities for research on many topics. In this thesis, we have selected to study the "quasi-coherent" plasma fluctuations near the plasma edge, and propagation of the fast magnetosonic waves in the plasma core. The next two sections briefly introduce these two subjects and emphasize the importance of their research.

1.2.1 Quasi-Coherent Fluctuations in the Enhanced D_α H-Modes

Depending on the plasma conditions, there are several regimes of tokamak operation. "L-mode" (low-confinement mode) is the oldest known. In this mode, density and temperature just gradually fall off from the plasma core towards its edges and it corresponds to the lowest energy confinement regime observed in older, circular cross section non-diverted tokamaks. A different regime (called H-mode for "high-confinement mode") was first discovered nearly two decades ago [9]. In this regime a transport barrier forms in the plasma edge, significantly increasing energy and particle confinement times and forming steep density and temperature gradients just inside the last closed flux surface. Such improved confinement regimes are routinely observed in diverted discharges with sufficient auxiliary heating.

There are several distinct types of H-mode observed, depending on the operating conditions. One is the ELM-free (Edge Localized Mode-free) H-mode. In this regime the plasma seems to be free of any large scale MHD (magnetohydrodynamic) instabilities in the edge. However, continuous impurity accumulation eventually leads to radiative collapse of the ELM-free H-mode plasma [10]. On the contrary, ELMy H-mode plasmas are periodically cleaned from impurities, and hence may be candidates for steady state operation. However, during the occurrence of ELMs, a large fraction of the stored energy is ejected across the plasma edge, leading to undesirably large heat loads on the divertor plates.

In the high density, compact, diverted Alcator C-Mod tokamak yet another kind

of H-mode is observed, the so-called enhanced D_α (EDA) H-mode [11]. Along with emitting much more radiation in the first D_α line of the deuterium Balmer spectral series, the plasma in this regime is characterized by significantly reduced impurity confinement compared to the ELM-free H-mode, while the energy confinement time is only marginally lower. The EDA H-mode is an excellent candidate for long pulse or steady state operation owing to the absence of excessive central radiation and large ELMs, and acceptable heat loads. Discharges in Alcator C-Mod were run continuously for at least 10 energy confinement times, limited only by the available RF pulse length (0.6 sec).

Importantly, the EDA H-mode is found to be always accompanied by a continuous, high frequency ($\sim$100 kHz) "quasicoherent" (QC) fluctuation mode, localized in the edge steep density gradient region (pedestal). It is these fluctuations that are thought to be responsible for the enhanced particle transport of the EDA H-mode, and therefore understanding the physics of this phenomena is of great importance.

Fortunately, the amplitude, wavelength and frequency of the QC fluctuation mode are all within the range of the phase contrast imaging diagnostic, and a vast array of data was collected almost for every C-Mod plasma starting April 1999. A major part of this thesis is dedicated to analysing these data in order to gain a better understanding of the QC mode.

1.2.2 Fast Magnetosonic Wave Propagation

The ohmic heating of the plasma current alone is typically not sufficient to generate the temperatures needed for fusion. An auxiliary heating source is needed. On the Alcator C-Mod tokamak, three ICRF (ion cyclotron range of frequencies) antennas, operating at 78, 80 and 80.5 MHz and radiating up to $\sim$5 MW of power, are used to heat the plasma.

The antennas have been designed to launch the *fast magnetosonic wave* (often called simply the *fast wave*). This wave is a subclass of ion cyclotron waves, which exist only in magnetized plasmas at frequencies comparable to the ion cyclotron frequency. ICRF heating occurs when the energy of the wave is transferred to particle

energy, for example through Landau or cyclotron damping. In Landau damping the phase velocity of the wave parallel to the magnetic field is similar to the thermal velocity of one of the plasma species, and some of those particles are preferentially accelerated. For ion cyclotron damping to occur, the wave should possess certain lefthand circular polarization and frequency that resonantly matches the particle gyrofrequency or its harmonics. It is important to maximize the wave absorbtion in the plasma core, otherwise most of the energy would be deposited to the vacuum chamber walls or (even worse) reflected back into the antenna. A better understanding of the physics of fast wave propagation should help us to optimize plasma heating by ICRF waves.

Of large interest to the fusion research is also the ICRF *current drive*. Currently, the plasma current (which is absolutely needed for a tokamak to operate) is generated by continuous raising of current in a transformer. Such scenario, unfortunately, would be unapplicable for a steady state fusion machine, since the current in the primary winding of the transformer cannot be raised indefinitely. In the ICRF current drive, not only the energy but also the momentum of the fast magnetosonic wave is transferred to the plasma and current can be driven continuously.

Significant progress in understanding the ICRF wave physics was done using numerical simulations. However, it is often hard to evaluate the validity of certain computers codes since typically there is very little information available about the wave behavior inside the tokamak. Using optical heterodyning technique, the phase contrast imaging diagnostic is now capable of providing such information.

Under certain condition, the fast waves may convert into *Ion Bernstein waves*. Using PCI, this phenomena was studied by another C-Mod graduate student, Eric Nelson-Melby[12, 13].

1.3 Thesis Outline

This thesis is divided into six chapters.

Chapter 1, "Introduction", is the current chapter. It introduces the reader to the

concepts of plasma fusion, magnetic confinement and tokamaks. The motivation and the key experimental technique used in this thesis research are also discussed.

Chapter 2, "Experimental Setup", starts with a brief description of light-plasma interaction and scattering theory. Then, the phase contrast technique is explained and compared to other laser based methods for measuring density fluctuations. An implementation of this technique on the Alcator C-Mod tokamak is reviewed. Finally, there is a description of the system calibration and testing routines.

Chapter 3, "Quasi-Coherent Fluctuations in the Enhanced D_α H-Modes", presents experimental study of the Quasi-Coherent (QC) mode by the PCI diagnostic. The results are then compared with the resistive ballooning X-point mode predicted by the BOUT (Boundary Plasma Turbulence) numerical code.

Chapter 4, "Optical Heterodyning Upgrade of the PCI System", covers the modifications made to the diagnostic to make it sensitive to the ion cyclotron range of frequencies waves. These wave are launched by three RF antennas and used for auxiliary heating and current drive.

In Chapter 5, "Fast Wave Detection and Modeling", we discuss results of the measurements of the fast magnetosonic wave - the dominant wave launched by the ICRF antennas. The experimental data are then compared with predictions of the three dimensional full wave computer code TORIC[14].

Chapter 6, "Conclusions and Future Plans", summarizes the research done for this thesis. Suggestions are given for the PCI diagnostic upgrades as well as for new areas of experimental studies and numerical modeling.

All the equations and formulas in this thesis are written in Gaussian (or *cgs*) system of units, unless specifically noted otherwise. However, some parameters are given in customary *mks* units (like *Tesla* for magnetic field strength) – these should be converted to *cgs* units when substituting into the equations.

Chapter 2

Experimental Setup

2.1 Electromagnetic Radiation and Plasma

The phase contrast imaging diagnostic relies on the interaction of electromagnetic radiation, such as light of an infrared laser, with a plasma. Using the laser beam as a probing source has many advantages. For example, the laser does not disturb the plasma and it can penetrate all the way into the plasma core. In this section I will briefly review the physics of light-plasma interaction.

2.1.1 Coherent vs. Incoherent Scattering

When electromagnetic radiation interacts with a plasma, it applies some oscillatory force to the charged particles. This force causes them to accelerate and to emit additional electromagnetic radiation in all directions. This effect is generally referred to as *scattering*. The frequency of visible or infrared light is $\omega > 10^{14}$ rad/sec and is typically much greater than the plasma frequency ω_{pe}, or the cyclotron frequency ω_{ce}, in a tokamak:

$$\omega_{pe} = \left(\frac{4\pi n_e e^2}{m_e}\right)^{1/2} \leq 2 \times 10^{12} \text{ rad/sec} \tag{2.1}$$

and

$$\omega_{ce} = \frac{eB}{m_e c} \leq 2 \times 10^{12} \text{ rad/sec} \ . \tag{2.2}$$

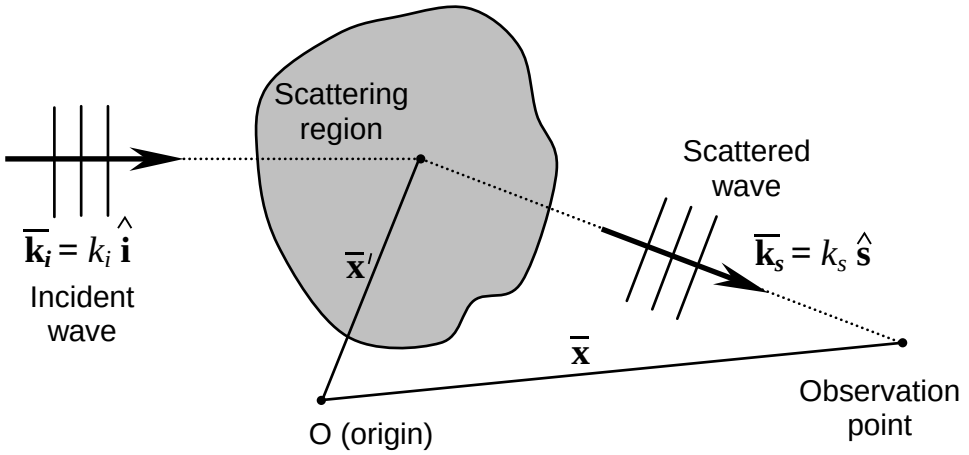

Figure 2-1: Schematic of a plane wave scattering from plasma.

Here, typical plasma parameters for the Alcator C-Mod tokamak were used, namely $n_e < 1 \times 10^{21}$ m^{-3} and $B < 8.1$ T. These two limits significantly simplify the analysis of the physics involved in the scattering.

Furthermore, only a macroscopically neutral plasma will be considered. The motion of the ions caused by the optical wave electric field can be neglected in view of their small charge-to-mass ratio, at least 1836 times less than that of an electron. Also, the thermal effects can be ignored for optical frequency waves since the typical electron thermal velocity $v_{te} = \sqrt{2kT_e/m_e} \approx 0.1c$ (assuming that for C-mod $T_e \approx 2$ keV) is small compared to the optical wave phase velocity, $v_{ph} \approx c$ (it will be verified later that v_{ph} for the CO_2 laser light in the plasma is indeed very close to the speed of light in vacuum, c).

Using these approximations, a calculation of the scattering from a single electron results in [15]

$$\mathbf{E}_s(\mathbf{x}, t) = -\frac{e}{c^2} \frac{\hat{\mathbf{s}} \times [\hat{\mathbf{s}} \times \dot{\mathbf{v}}]}{|\mathbf{x} - \mathbf{x}'|}\bigg|_{retarded} , \tag{2.3}$$

where the electron acceleration $\dot{\mathbf{v}} = -e\mathbf{E}_i/m_e$ is evaluated at the retarded time $t' = t - |\mathbf{x} - \mathbf{x}'|/c$, and $\hat{\mathbf{s}}$ is a unit vector in the scattered wave direction (see Fig. 2-1). However, in case of a plasma one has to deal with many electrons at the same time.

One possible way to calculate the scattered light from plasma would be to treat the radiation from all the electrons independently and simply add the intensities of light coming from every single electron. This scenario is referred to as *incoherent* scattering.

However, there are limits to which one can treat electrons as independent particles. In general, electrons in the plasma interact with each other. The characteristic distance for such interaction is the *Debye* length

$$\lambda_D = \left(\frac{KT}{8\pi n_e e^2}\right)^{1/2}. \tag{2.4}$$

Every charged particle in the plasma creates an electrical field and therefore affects nearby electrons. Those electrons in turn create a *sheath* around the original particle and effectively shield its field over a scale distance λ_D. This way, only electrons separated by a distance over a few λ_D are completely shielded from one another and can be treated independently.

So how would this collective behavior affect the scattering? The fields generated by the electrons will now be correlated and one should be adding up not the intensities, but rather amplitudes of these fields. The scattering becomes *coherent*, or *collective*. The conditions determining the kind of scattering are defined by the value of the plasma fluctuation wave number [15]

$$\mathbf{k} = \mathbf{k}_s - \mathbf{k}_i \ , \tag{2.5}$$

where $\mathbf{k}_i$ and $\mathbf{k}_s$ are the wave vectors of the incident and the scattered waves respectively. The incoherent scattering exists in the short-wavelength limit $k\lambda_D \gg 1$, while the coherent scattering requires $k\lambda_D \ll 1$. The need to use k, not k_i or k_s, is justified by the fact that we should consider the distance over which the phase difference of the incident and the scattered waves changes considerably, not their separate phases.

All of the scattering measured by the PCI diagnostic and discussed in this thesis is coherent. Indeed, for C-Mod typically $\lambda_D \sim$ 0.4-15 μm and $2\pi/k \sim$ 0.6-20 cm ($k\lambda_D < 0.015 \ll 1$).

2.1.2 Scattering from Density Fluctuations

In the coherent scattering limit we can neglect individual electrons and use a smoothed electron density function $n_e(\mathbf{x}, t)$. Using Eq. 2.3, the scattering field (far from the scattering center) then becomes

$$\mathbf{E}_s(\mathbf{x}, t) \approx r_e \int n_e(\mathbf{x}', t') \frac{\hat{\mathbf{s}} \times [\hat{\mathbf{s}} \times \mathbf{E}_i(\mathbf{x}', t')]}{|\mathbf{x} - \mathbf{x}'|} \, d^3\mathbf{x}' \ , \tag{2.6}$$

where $r_e = e^2/m_e c^2 = 2.8179 \times 10^{-13}$ cm is the classical electron radius.

For further analysis let us assume that the incident wave is plane and purely monochromatic

$$\mathbf{E}_i(\mathbf{x}, t) = \mathbf{E}_i e^{i(\mathbf{k}_i \cdot \mathbf{x} - \omega_i t)} \ . \tag{2.7}$$

For simplicity it is also assumed that the size of the scattering region is much smaller then the distance from it to the observation point. Equation 2.6 is then transformed into [16]

$$\mathbf{E}_s(\omega_s) = \frac{r_e e^{i\mathbf{k} \cdot \mathbf{x}}}{2\pi |\mathbf{x} - \mathbf{x}'|} \, \hat{\mathbf{s}} \times [\hat{\mathbf{s}} \times \mathbf{E}_i] \int n_e(\mathbf{x}', t) e^{-i(\mathbf{k} \cdot \mathbf{x}' - \omega t)} \, dt \, d^3\mathbf{x}' \ , \tag{2.8}$$

where $\omega = \omega_s - \omega_i$.

The expression inside the integral here is just the Fourier transform of the density waves in plasma. Thus, if only a single-frequency, single-$\mathbf{k}$ density wave is present then there should be only two possible scattered waves. One wave would have

$$\omega_s = \omega_i + \omega \quad \text{and} \quad \mathbf{k}_s = \mathbf{k}_i + \mathbf{k} \tag{2.9}$$

and the other

$$\omega_s = \omega_i - \omega \quad \text{and} \quad \mathbf{k}_s = \mathbf{k}_i - \mathbf{k}, \tag{2.10}$$

where we assumed infinite integration time and volume. Rescattering of the scattered radiation is negligible under all practical conditions.

2.1.3 Index-of-Refraction Approach

There is another mathematically equivalent and somewhat simpler approach to consider the scattering off density fluctuations. In this approach the plasma is treated as an optical medium with macroscopic changes in its index of refraction. Indeed, the motion of electrons in the field of an incident monochromatic wave induces a current density in the plasma

$$\mathbf{J} = -en_e\mathbf{v}_e = -en_e(-i\frac{e}{m_e\omega})\mathbf{E} \ , \tag{2.11}$$

where ω is the frequency of the wave; magnetic field effects are assumed negligible since $\omega \gg \omega_{ce}$. The effective plasma *conductivity* is

$$\sigma = \frac{\mathbf{J}}{\mathbf{E}} = i\frac{n_e e^2}{m_e\omega} = i\frac{\omega_{pe}^2}{4\pi\omega} \tag{2.12}$$

and the complex *dielectric* value is

$$\epsilon \equiv 1 + i\frac{4\pi\sigma}{\omega} = 1 - \frac{\omega_{pe}^2}{\omega^2}. \tag{2.13}$$

The *index of refraction* of the plasma (the ratio of the wave phase velocity to the speed of light) is [16]

$$N \equiv \frac{kc}{\omega} = \sqrt{\epsilon} \approx 1 - \frac{\omega_{pe}^2}{2\omega^2} \ , \tag{2.14}$$

where $\omega \gg \omega_{pe}$ is used.

As an example consider the single-frequency, single-$\mathbf{k}$ density wave in a plasma that propagates across the incident optical beam. It can be represented as a phase diffraction grating. The incident beam then diffracts into the three parts: the original beam and the two first-order sideband beams. Higher order sideband beams do not exist when the grating function is sinusoidal. The scattering angles are

$$\sin\theta = \pm\frac{\lambda}{\Lambda} \ , \tag{2.15}$$

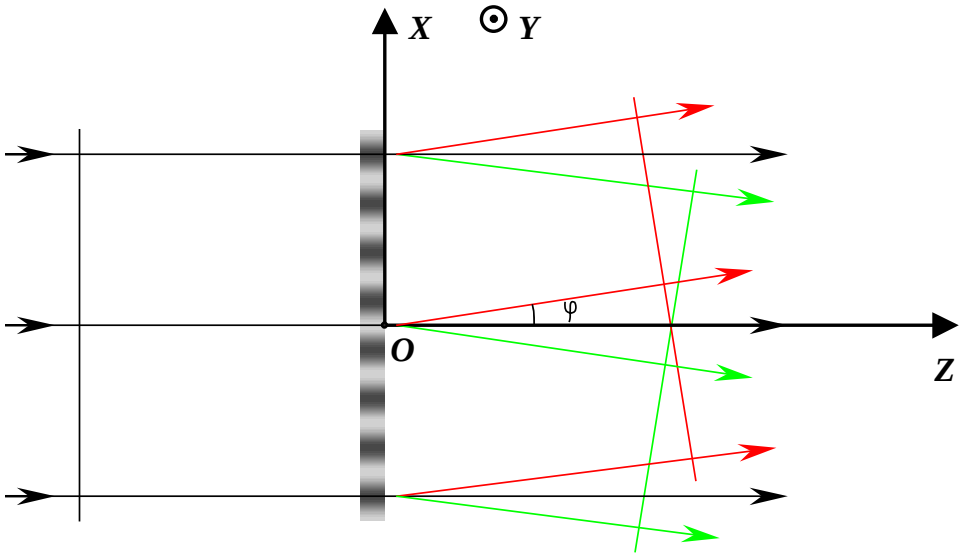

Figure 2-2: Scattering of the plane monochromatic wave from a thin-layer plasma.

where λ is the optical wavelength and Λ is the wavelength of the grating. Since the grating is moving in space the frequency of the sideband beam should be doppler up- or down-shifted by ω. The upshifted and downshifted beams correspond to the scattered waves from Eqs. 2.9 and 2.10, respectively.

This example demonstrates quickly that the two approaches are equivalent. Only the *index-of-refraction* approach will be used in the remainder of this thesis.

2.1.4 Plane Wave Propagation in Plasma

Consider a plane polarized monochromatic wave traveling through a thin layer of plasma as shown in Fig. 2-2. Let the electric field of this wave be

$$\mathbf{E}_0(x, y, z, t) = \mathbf{E}_0 e^{i(k_0 z - \omega_0 t)} \ . \tag{2.16}$$

Let the thickness of this thin plasma layer be l. The limit in which the plasma layer can be considered "thin" will be derived later. For now consider l to be infinitely small. Let the electron density of the plasma be as follows

$$n_e(x, y, z, t) = n_{e0} + \tilde{n}_e \cos(k_p x) \ . \tag{2.17}$$

After propagating through the optical medium (plasma) with the index of refraction given by Eq. 2.14, the plane incident wave acquires a phase delay

$$\Phi(x,y,t) = k_0 \int (N-1)\ dz = -\frac{k_0}{2\omega_0^2} \int \omega_{pe}^2 dz\ . \tag{2.18}$$

Since the original optical wave propagates with nearly the speed of light one can substitute $\omega_0/k_0 \approx c$. Using also the formulas for classical electron radius $r_e = e^2/m_e c^2 = 2.8179 \times 10^{-13}$ cm and the plasma frequency $\omega_{pe}^2 = 4\pi n_e e^2/m_e$ the previous equation can be rewritten as

$$\Phi(x,y,t) = -\lambda_0 r_e \int n_e(x,y,z,t)\ dz\ . \tag{2.19}$$

This is a very important result: **when the plane monochromatic wave propagates through a thin plasma layer it acquires a phase delay that is directly proportional to the line integral of the electron density**. This statement is one of the basic principles for using Phase Contrast Imaging (PCI) as plasma diagnostic.

For the density function given by Eq. 2.17 the phase delay becomes

$$\Phi(x,y,t) = \Delta \cos k_p x + \Phi_0\ , \tag{2.20}$$

where $\Phi_0 = -\lambda_0 r_e l n_{e0}$ is just a phase constant and $\Delta = -\lambda_0 r_e l \tilde{n}_e$. Φ_0 carries no physical significance in scattering from density fluctuations and is dropped for simplicity in the remainder of this chapter.

The amplitude of the electric field in the $z = 0$ plane is then given by

$$E_{z=0} = E_0 e^{i\Delta \cos k_p x}\ . \tag{2.21}$$

A wave with such an electric field can be decomposed into a set of the plane waves [17] with amplitudes and wave vectors given by

$$E(k_x, k_y) = \left\langle E_{z=0} e^{-i(k_x x + k_y y)} \right\rangle\ , \tag{2.22}$$

$$\mathbf{k} = k_x\hat{\mathbf{x}} + k_y\hat{\mathbf{y}} + \sqrt{k_0^2 - k_x^2 - k_y^2}\ \hat{\mathbf{z}}\ , \tag{2.23}$$

where the average $\langle ... \rangle$ is taken over all x and y.

If the phase changes introduced by the plasma are small ($|\Delta| \ll 1$) only three plane waves are present in the decomposition. These are the original wave and the two scattered waves

$$E(k_x = 0, k_y = 0) = E_0(1 - \frac{\Delta^2}{2}) \approx E_0 \tag{2.24}$$

and

$$E(k_x = \pm k_p, k_y = 0) = E_0\frac{i\Delta}{2}\ . \tag{2.25}$$

To summarize this section, a density wave in the plasma adds to the incident plane wave the two scattered plane-wave components with the amplitudes and the directions given by Eq. 2.25. Since all computations are linear, if there are two or more density waves present each of them will produce the scattered waves independent of the other. In the general case the density profile can be decomposed into Fourier harmonics and treated as a set of density waves.

The scattered waves travel at an angle $\sin\phi = \pm\lambda_0/\lambda_p$ to the incident wave. If the plasma is not *thin* the waves scattered by the front and the rear parts of the plasma will separate and will no longer be in phase. This imposes the limit[1] on the plasma thickness l when it still can be treated as a single layer

$$l < \frac{\lambda_p^2}{2\pi\lambda_0}\ . \tag{2.26}$$

In the PCI on the Alcator C-Mod $l \approx 60\ cm$ and the plasma is thin when $\lambda_p > 0.6\ cm$. All the measurements described in this thesis were taken in this regime.

[1]More discussion of this limit is in section 2.2.4

2.2 The Phase Contrast Technique

2.2.1 A Brief History

The need for viewing *phase objects* existed a long time ago. A phase object is one that alters the phase but not the amplitude of the incident wave. An object of this type is of non-uniform optical thickness, but does not absorb any of the incident light. Such objects are frequently encountered in biology, crystallography, and other fields. Unfortunately, with ordinary methods of observation little information can be obtained about phase objects since most observing instruments (including the human eye) can only distinguish changes in the intensity of the light. One can only get information about the amplitude changes but not the phase changes introduced by the object.

The earliest empirical attempts to enhance phase object imaging date back to the middle of the 19th century. They include the *central dark ground* method and the *schlieren*[2] method. However, it was not until 1935 when the most powerful method, the *phase contrast technique*, was introduced by the Dutch physicist Fritz Zernike[18, 19]. The method had the advantage of producing an intensity distribution which was directly proportional to the phase changes introduced by the object. The first application of the technique was in the phase-contrast microscope. The new instrument provided much better images of objects such as bacteria and animal cells and tissues, and was used extensively in biology and medicine. To recognize the importance of his invention, in 1953 Zernike was awarded the Nobel prize in physics.

The first application of the phase contrast technique in a plasma was done by Presby and Finkelstein at Yeshiva University, New York[20]. They employed a pulsed ruby-laser illumination to create photographic images of shock waves and vacuum spark discharges. It was demonstrated that the technique is superior to the schlieren method in the same configuration.

Henri Weisen, of the Ecole Polytechnique Fédérale de Lausanne, Switzerland[21,

[2]German for *streak*

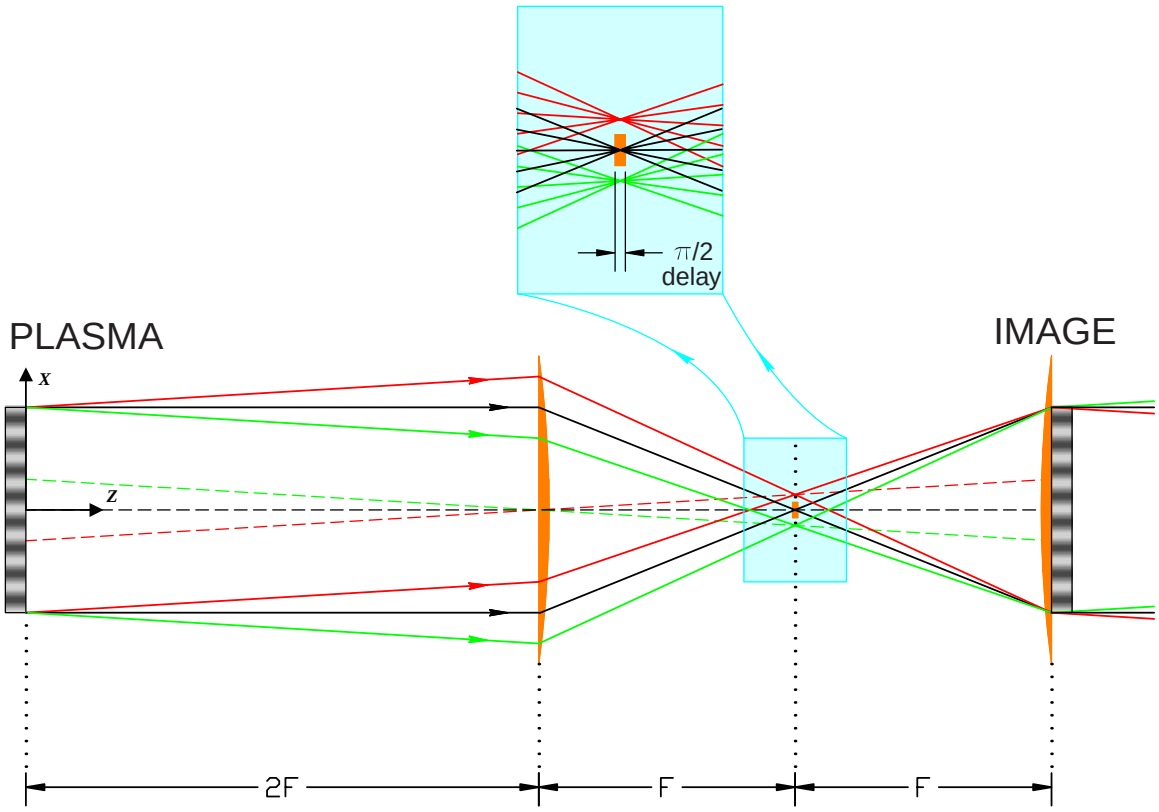

Figure 2-3: The simplest phase contrast imaging system.

22, 23, 24, 25] was the first to apply the phase contrast imaging to a plasma fusion device. Weisen used a CO_2 laser and a semiconductor detector array to study turbulence and driven Alfvén waves in the TCA tokamak. After the technique had been proven successful, it was utilized on other machines. These included the DIII-D tokamak at General Atomics[26, 27, 28], the Heliotron-E device at Kyoto University in Japan[29, 30], the TEXT-U tokamak at the University of Texas at Austin[31] and the CDX-U tokamak at Princeton University[32]. Finally, in 1998, a Phase Contrast Imaging (PCI) diagnostic has become operational on the Alcator C-Mod tokamak[33].

2.2.2 Basic Principles of the Phase Contrast Technique

In this section I will explain the physical principles of the phase contrast method using a simple imaging system depicted in Fig. 2-3 as an example. In this system a phase object, such as a plasma, is back-illuminated by a collimated monochromatic

light source. Two lenses of focal length F create an image of that object in the image plane. When positioned as shown, these two lenses provide a magnification coefficient of one and also insure that a plane wave is converted into a plane wave.

As in section 2.1.4, a plasma with a periodic density variation is taken to be

$$n_e(x, y, z, t) = n_{e0} + \tilde{n}_e \cos(k_p x) \tag{2.27}$$

for the object. The back-illuminating electromagnetic wave (Eq. 2.16) is then scattered into three parts given by Eqs. 2.24 and 2.25. The sum of the individual electric fields of these three waves in the object plane

$$E_{object} = E_0 + E_0 \frac{i\Delta}{2} \exp(ik_p x) + E_0 \frac{i\Delta}{2} \exp(-ik_p x) \tag{2.28}$$

represents the electric field pattern in this plane and is just a small term expansion of Eq. 2.21, and $\Delta = -\lambda_0 r_e l \tilde{n}_e$ is the amplitude of phase variations in the object, $|\Delta| \ll 1$. The first term here is due to the unscattered wave and the second two terms represent the scattered components.

Normally, this pattern is just copied exactly into the image plane (times some phase multiplier, which is dropped for simplicity) and results in the uniform intensity I distribution

$$E_{image} = E_0 + E_0 \frac{i\Delta}{2} \exp(ik_p x) + E_0 \frac{i\Delta}{2} \exp(-ik_p x) \tag{2.29}$$

$$I = \frac{c}{8\pi}|E_{image}|^2 = \frac{c}{8\pi}|E_0|^2|1 + i\Delta \cos k_p x|^2 = \frac{c}{8\pi}|E_0|^2 \left(1 + O(\Delta^2)\right) \approx \frac{c}{8\pi}|E_0|^2 \ . \tag{2.30}$$

In the phase contrast technique a *phase plate* is placed in the focal plane of the first imaging lens. An example of such plate is shown in Fig. 2-3. It is just a small window made out of an optically dense material. Its thickness is such that a passing electromagnetic wave picks up (or delayed by) an extra $\pi/2$ phase shift.

The phase contrast technique relies on a fact that the first imaging lens focuses the three object plane waves into three individual spots and thus efficiently separates

the waves in space. This allows the phase plate to be placed in such a manner that only the unscattered wave picks up the $\pi/2$ phase delay. When the waves recombine on the image this delay results in the additional i multiplier for the first term in

$$E_{image}^{PCI} = i \times E_0 + E_0 \frac{i\Delta}{2} \exp(ik_p x) + E_0 \frac{i\Delta}{2} \exp(-ik_p x) \ . \tag{2.31}$$

This i multiplier is the sole change in the electric field distribution due to the phase plate (compare Eqs. 2.29 and 2.31). However, it makes a profound difference for the image intensity. The electric field due to scattered components is now in phase with the incident wave field. Interference between them results in variations of the electric field amplitude and thus the intensity

$$I_{PCI} = \frac{c}{8\pi} |E_{image}^{PCI}|^2 = \frac{c}{8\pi} |E_0|^2 \times |1 + \Delta \cos k_p x|^2 \approx \frac{c}{8\pi} |E_0|^2 (1 + 2\Delta \cos k_p x) \ . \tag{2.32}$$

To reiterate, **the phase contrast technique transforms phase variations in the phase object into amplitude (and therefore intensity) variations in the image**. If the phase variations are small this **transformation is linear**. The relative intensity variations are then just twice the phase variations, as can be seen from Eqs. 2.20 and 2.32

$$\frac{\tilde{I}/I_0}{\tilde{\Phi}} = \frac{2\Delta \cos k_p x}{\Delta \cos k_p x} = 2 \ . \tag{2.33}$$

This linearity makes the phase contrast the best technique for imaging of phase objects. Additionally, the intensity variations produced by this technique are higher (often much higher) then with other available methods, as will be shown further in this section of the thesis.

2.2.3 Phase Contrast Imaging vs. Central Dark Ground and Schlieren Techniques

Central dark ground and *schlieren* are two other methods used for imaging phase objects[34]. In this section I will discuss their properties and compare them to the phase contrast imaging method. The goal is to prove the superiority of the PCI and

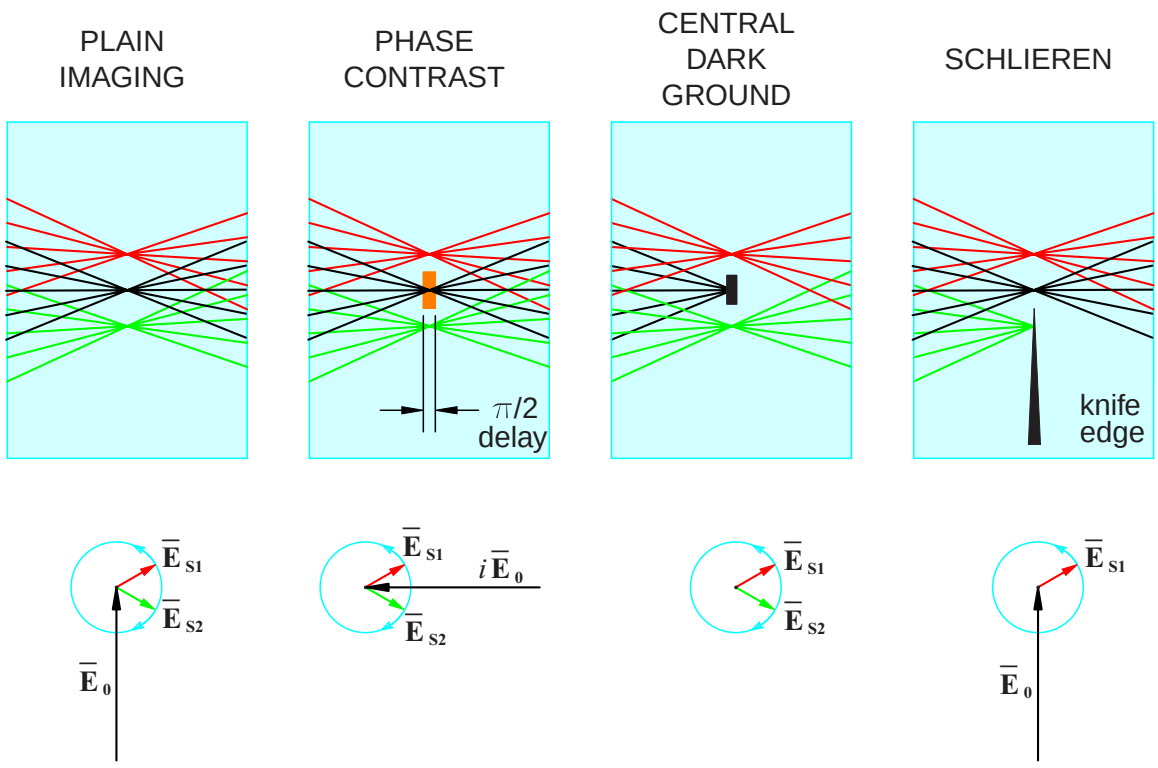

Figure 2-4: A comparative analysis of spatial filtering techniques.

further describe the technique. I will continue to use the example of a simple imaging system from Fig. 2-3.

The commonality of all three techniques is that they all rely on spatial filtering in the focal plane of the first imaging lens. While the PCI is based on delaying the unscattered wave by a quarter period by using a phase plate, the central dark ground and the schlieren methods utilize blocking some of the waves completely. Figure 2-4 illustrates the process. The four boxes on top show different configurations for the focal plane area. In this area the scattered and the unscattered waves are focused into points and become separated in space. Underneath the boxes are complex-plane vector diagrams for the electric field amplitudes on the image (not to be confused with vectors in real space). As one moves along the image plane, complex amplitudes $\mathbf{E}_{S1}$ and $\mathbf{E}_{S2}$ of the scattered waves rotate in the opposite directions. The reason for this rotation is a non-zero $k_x = \pm k_p$ component of the scattered wave wavenumbers.

In plain imaging of a phase object the sum of $\mathbf{E}_{S1}$ and $\mathbf{E}_{S2}$ stays perpendicular to $\mathbf{E}_0$. This results in only slight turning of the total amplitude vector while its

length stays constant, exactly as it should for a phase object. No intensity variations are present. In the phase contrast technique the phase of the unscattered wave is delayed by $\pi/2$. This can be represented by turning the vector $\mathbf{E}_0$ by 90° in Fig. 2-4. The scattered waves now change the length of the total vector and keep its direction constant. What used to be a phase change now becomes an amplitude (and therefore intensity) change.

In the central dark ground method a small non-transparent object (usually a thin wire) is used to block only the unscattered wave. The schlieren method (also known as *"knife edge"* method) relies on blocking all the scattered components to one side of the unscattered wave[3]. Naturally, a typical tool for this purpose is a knife edge or a similar object. The two techniques correspond to removing $\mathbf{E}_0$ and $\mathbf{E}_{S2}$ vectors, respectively, from the complex-plane vector diagram in Fig. 2-4. In both cases the total amplitude vector variates in length and direction, making the original phase oscillations visible.

Blocking of the center wave in the central dark ground (C.D.G.) technique modifies the original image electric field distribution (Eq. 2.29). The new distribution is given by

$$E_{image}^{C.D.G.} = 0 \times E_0 + E_0 \frac{i\Delta}{2} \exp(ik_p x) + E_0 \frac{i\Delta}{2} \exp(-ik_p x) \ . \tag{2.34}$$

The zero multiplier in the first term represents the unscattered wave being blocked. The image intensity for this technique is then given by

$$I_{C.D.G.} = \frac{c}{8\pi} |E_{image}^{C.D.G.}|^2 = \frac{c}{8\pi} |E_0|^2 \times |i\Delta \cos k_p x|^2 = \frac{c}{8\pi} |E_0|^2 \Delta^2 \cos^2 k_p x \ . \tag{2.35}$$

Comparison with the PCI intensity function (Eq. 2.32) immediately displays the main drawback of the central dark ground technique. The amplitude of intensity variations is now $\tilde{I} = \Delta^2 I_0$, which is much smaller than $\tilde{I} = 2\Delta I_0$ for the PCI. In a plasma $|\Delta| \ll 1$ ($|\Delta| < 10^{-3}$ rad for Alcator C-Mod) and the signals are already small even for the phase contrast. Additionally, the transfer function is no longer linear for

[3]Only one scattered wave is present on each side in this example. However, in the general case it should be replaced with a scattered wave spectrum.

this technique. The image intensity variation is proportional to the phase variation squared, making frequency analysis much more complex.

Although it does not follow directly from the above equations, the central ground method is also much more sensitive to optical misalignment. The unscattered wave should be blocked as completely as possible in order to allow the scattered components to dominate the image. Diffraction effects and mechanical vibrations tend to let some unscattered radiation pass through.

With the phase contrast imaging, intensity variations appear on top of a much higher uniform background level. This is the only aspect where the central dark ground technique has an advantage. In the latter technique, blocking the strong central wave removes the background and allows 100% intensity oscillations.

Similar analysis can be done for the schlieren technique. Blocking one of the scattered waves is represented by zeroing the last term in the electric field distribution function

$$E_{image}^{schlieren} = E_0 + E_0 \frac{i\Delta}{2} \exp(ik_p x) + 0 \times E_0 \frac{i\Delta}{2} \exp(-ik_p x) \tag{2.36}$$

and the resulting image intensity is now given by

$$I_{schlieren} = \frac{c}{8\pi} |E_0|^2 |1 + i\frac{\Delta}{2} \cos k_p x - \frac{\Delta}{2} \sin k_p x|^2 \approx \frac{c}{8\pi} |E_0|^2 (1 - \Delta \sin k_p x) \ . \tag{2.37}$$

By comparing with Eq. 2.32, one can see that the intensity oscillation amplitude for the schlieren technique $\tilde{I} = \Delta I_0$ is only half of what it is for the PCI. Also, the intensity pattern is delayed a quarter period from the phase pattern, meaning that in general the phase-to-intensity translation function is no longer linear. However, it is still linear in k-space for the purpose of simple frequency analysis. All said, this technique is not much worse than the phase contrast but it has no advantages either.

2.2.4 Phase Contrast Imaging vs. Phase Scintillation and Shadowgraphy Techniques

Phase scintillation[35] and *shadowgraphy*[36] are two other techniques for imaging

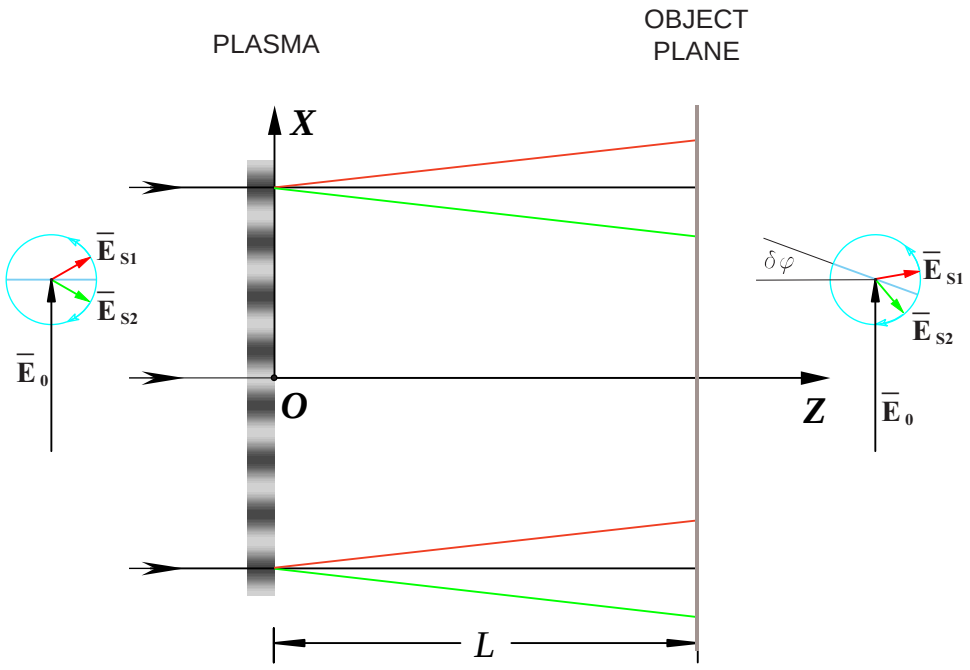

Figure 2-5: The Phase Scintillation technique.

plasma density fluctuations. Understanding these techniques is important because the phase contrast imaging may exhibit some of their properties under certain conditions.

The plasma given by the equations 2.27 and 2.28 is still being used as an example. In Fig. 2-3 the plasma layer is placed in the object plane of the imaging system. The object electric field distribution is then just copied into the image plane. Unless some spatial filtering is used, the image intensity is uniform.

Suppose now that the actual object (plasma layer) and the object plane of the imaging system are separated by a distance L as shown in Fig. 2-5. Since the scattered waves travel different distances and in different directions compared to the unscattered wave they acquire some additional phase shift. This can be represented by rotating the complex plane vectors $\mathbf{E}_{S1}$ and $\mathbf{E}_{S2}$ in the same direction by an angle $\delta\phi$. The sum of these two vectors now has a component along $\mathbf{E}_0$. This means that the length of the total electric field vector should oscillate as one moves along the object plane. When the object plane is copied into the image plane, oscillations appear in the image intensity (even without a phase plate).

To find a phase shift for the scattered wave one can use the z-component of its

wave number given by Eqs. 2.23 and 2.25

$$k_z = \sqrt{k_0^2 - k_p^2} \approx k_0 \left(1 - \frac{\lambda_0^2}{2\lambda_p^2}\right) \ , \tag{2.38}$$

$$\delta\phi = L(k_0 - k_z) = \frac{\pi\lambda_0 L}{\lambda_p^2} \ , \tag{2.39}$$

where λ_0 and λ_p are the wavelengths of the electromagentic wave and the plasma wave respectively. The original electric field distribution function from Eq. 2.28 becomes

$$E_{scintillation} = E_0 + E_0\frac{i\Delta}{2}\exp(ik_p x - i\delta\phi) + E_0\frac{i\Delta}{2}\exp(-ik_p x - i\delta\phi) \tag{2.40}$$

in the new object plane. The term $i\delta\phi$ represents the additional phase shift for the scattered waves. The corresponding image intensity is

$$I_{scintillation} = \frac{c}{8\pi}|E_0|^2|1 + i\Delta e^{-i\delta\phi}\cos k_p x|^2 \approx \frac{c}{8\pi}|E_0|^2(1 + 2\Delta\sin\frac{\pi\lambda_0 L}{\lambda_p^2}\cos k_p x) \ . \tag{2.41}$$

One can see that the phase scintillation technique can provide the same amplitude of intensity fluctuations as the PCI when $L = \lambda_p^2/2\lambda_0$. It is also simpler because no spatial filtering is needed. But everything comes at a price. Since the condition $L = \lambda_p^2/2\lambda_0$ can be satisfied only for a single value of λ_p the phase scintillation is not good at looking at a broad range of plasma oscillations. In general, the response function is non-linear. Also, because of diffraction effects, the technique cannot be used for large values of λ_p (of order of the aperture size). The PCI is free of these limitations.

It can be easily shown, that when the two techniques used together (i.e. when a plasma is moved from the object plane of the phase contrast imaging system) the sine function is replaced with a cosine in the Eq. 2.41

$$E_{PCI+scin.} = i \times E_0 + E_0\frac{i\Delta}{2}\exp(ik_p x - i\delta\phi) + E_0\frac{i\Delta}{2}\exp(-ik_p x - i\delta\phi) \ , \tag{2.42}$$

$$I_{PCI+scin.} = \frac{c}{8\pi}|E_0|^2|1+\Delta e^{-i\delta\phi}\cos k_p x|^2 \approx \frac{c}{8\pi}|E_0|^2(1+2\Delta\cos\frac{\pi\lambda_0 L}{\lambda_p^2}\cos k_p x) \ . \tag{2.43}$$

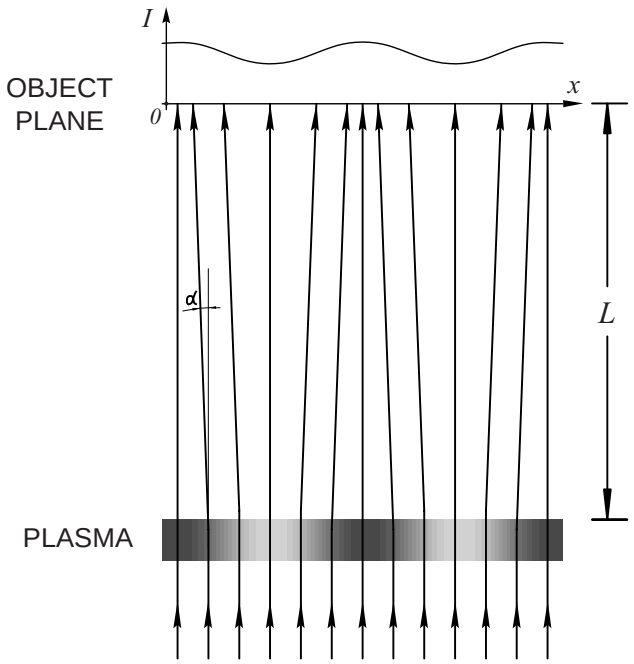

Figure 2-6: The Plasma Shadowgraphy technique.

The PCI performance degrades as the system becomes misaligned and defocused, especially for short wavelength density fluctuations. One can define a depth of focus parameter as the distance from the object plane when the signal drops to $\sqrt{0.5}$ of the maximum value. It is then given by

$$|L| \leq \frac{\lambda_p^2}{4\lambda_0} \ . \tag{2.44}$$

Not surprisingly, this is very similar to the limit on the plasma layer thickness in Eq. 2.26. The two limits are derived from the same physical principles. Additionally, from Eq. 2.43 for large values of L the amplitude of intensity oscillations should oscillate as L increases, as was confirmed experimentally by H. Weisen [23].

The shadowgraphy technique (see Fig. 2-6) also relies on separation of the actual phase object (such as plasma) and the object plane of the imaging system. Since the index of refraction of the plasma depends on its density (Eq. 2.14), denser regions of the plasma act as diverging lenses and create dark spots or "shadows" in the object plane. Likewise, less dense regions create bright spots.

The shadowgraphy technique can be reproduced even in everyday life. One of the examples would be a BBQ grill on a sunny day. The convective flows of cold and hot air have a different index of refraction and are easily seen above the grill on its shadow.

To find the intensity variations produced by the shadowgraphy method one can use a simple geometric optics approximation. The refraction angle α for rays emanating from the plasma is given by

$$\alpha = -\frac{\lambda_0}{2\pi}\frac{d\Phi}{dx} \ . \tag{2.45}$$

The image intensity is proportional to ratio of the distances enclosed between two particular beams in the plasma plane and the object plane of the imaging system. Taking this distance to be dx in the plasma plane one obtains

$$I_{shadowgraphy} = I_0\frac{dx}{dx - Ld\alpha} \approx I_0\left(1 + L\frac{d\alpha}{dx}\right) = I_0\left(1 - \frac{\lambda_0 L}{2\pi}\frac{d^2\Phi}{dx^2}\right) \ , \tag{2.46}$$

where $|\frac{d\alpha}{dx}| \ll L^{-1}$ is assumed. Once again, for the plasma given by the Eqs. 2.27 and 2.28 this reduces to

$$I_{shadowgraphy} = I_0\left(1 + \frac{2\pi\lambda_0 L}{\lambda_p^2}\Delta\cos k_p x\right) \ . \tag{2.47}$$

It can be seen immediately that this result is identical to the intensity provided by the phase scintillation technique in the limit $\lambda_0 L \ll \lambda_p^2$ (Eq. 2.41). The two techniques are just different approaches to describing the same physical events. As a results, the shadowgraphy technique shares the limitations and drawbacks of the phase scintillation method. Namely, the technique is non-linear and has a weak response to long wavelength plasma density fluctuations.

To summarize, the phase scintillation and shadowgraphy techniques are inferior to phase contrast imaging. However, one should pay attention to careful alignment and focusing of the PCI system since the phase scintillation or shadowgraphy effects may be introduced and cause some uncertainty in the measured signals.

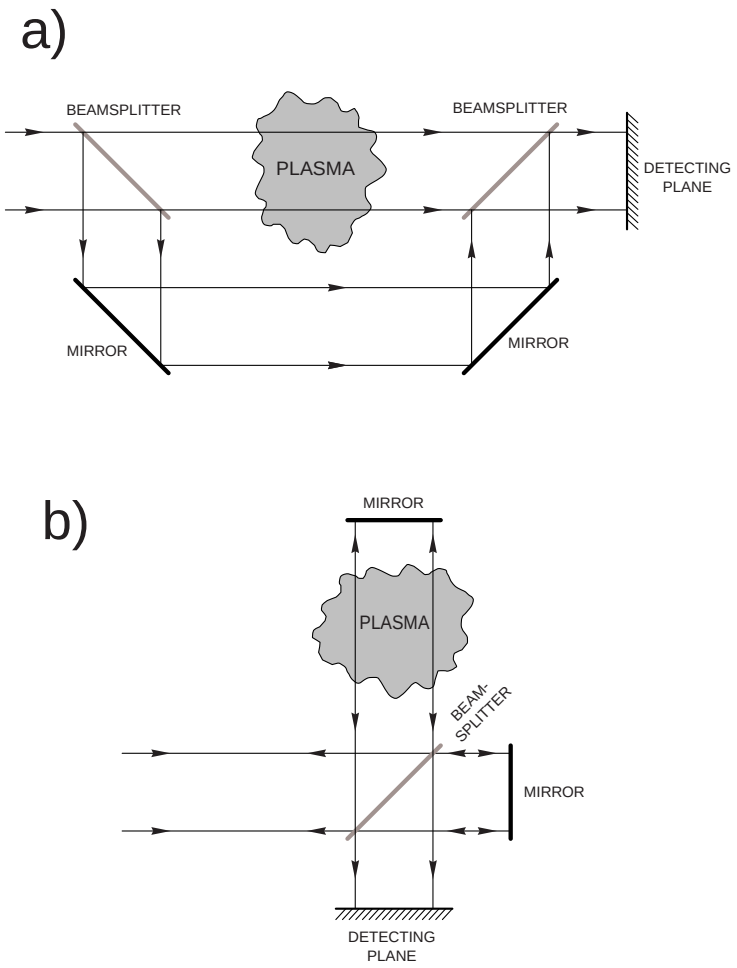

Figure 2-7: The two most common interferometer layouts: (a). The Mach-Zehnder interferometer; (b). The Michelson interferometer.

2.2.5 Phase Contrast Imaging vs. Interferometry

Interferometry is a traditional way to observe small variations of the index of refraction in a transparent object. In many ways, it is similar to the techniques previously described in this chapter and even may outperform them in certain applications. However, the interferometry also comes with some major drawbacks that limit its application. In this section, I will evaluate the interferometry usefulness for the plasma diagnostic purposes and justify the selection of the phase contrast technique and not interferometry for my research.

The interferometry technique relies on splitting a monochromatic laser beam into two parts as shown in Fig 2-7. One part (called a "probing beam") propagates

through the object of interest and picks up the information about changes in the index of refraction. The second part (called a "reference beam") is allowed to propagate freely in air or vacuum.

One has to differentiate between the *interferometer* and the *interferometric imaging system*. To add to the confusion, the latter is often called just an "interferometer" for simplicity. The difference is that the plain interferometer is based on a narrow laser beam and a single detector element and designed to provide just a single line-integrated measurement. Contrary to that, the interferometric imaging system uses a wide collimated laser beam to generate a complete two dimensional image of the index of refraction variations inside the object.

The two most common layouts for the interferometric imaging system are the Mach-Zehnder interferometer and the Michelson interferometer (shown in Fig. 2-7a and 2-7b respectively). Both designs are very similar and based on the same principles. One major difference is that the probing beam of the Michelson interferometer passes through the object twice.

To calculate the response of the Mach-Zehnder interferometer let us assume that the original laser beam and the transparent object (plasma) are still given by the equations 2.16 and 2.17. After the splitting the probing and the reference beams each has the amplitude of $E_0/\sqrt{2}$. The phase delay acquired by the probing beam when passing through the plasma was calculated to be (Eq. 2.20)

$$\Phi(x, y, t) = \Delta \cos(k_p x) + \Phi_0 \ . \tag{2.48}$$

Earlier we dropped the Φ_0 (the phase delay introduced by the whole plasma) when dealing with the phase contrast method since this delay was identical for all parts of the laser beam and did not affect the final result. However, in interferometry this term must be kept since it specifies the amount of phase delay acquired only by the probing beam and not the reference beam.

When the two beams are recombined on the detecting plane the electric field

amplitude is:

$$E_{image}^{interferometer} = \frac{E_0}{2}\exp(i\Delta\cos(k_p x) + i\Phi_0) + \frac{E_0}{2}\exp(i\Phi_{ref}) \ , \tag{2.49}$$

where Φ_{ref} is the phase difference between the probing and the reference beam with no plasma present. Additional $\sqrt{2}$-times drop in each beam amplitude is due to the second reflection/passing through a beam splitter. The intensity on the detecting plane is then given (after some arithmetic) by

$$I_{interferometer} = \frac{c}{8\pi}\frac{|E_0|^2}{2}\Big[1 + \cos\Big(\Delta\cos(k_p x) + (\Phi_0 - \Phi_{ref})\Big)\Big]. \tag{2.50}$$

Since $|\Delta| \ll 1$ in most cases this can be rewritten as

$$I_{interferometer} = \frac{c}{8\pi}\frac{|E_0|^2}{2}\Big[1 + \cos(\Phi_0 - \Phi_{ref}) - \Delta\cos(k_p x)\sin(\Phi_0 - \Phi_{ref})\Big]. \tag{2.51}$$

One exception is the case when $\Phi_0 - \Phi_{ref} = \pi$ (plus/minus any multiple of 2π). In this particular case all the terms up to $O(\Delta^2)$ need to be kept, yielding

$$I_{interferometer} = \frac{c}{8\pi}\frac{|E_0|^2}{4}\Delta^2\cos^2(k_p x). \tag{2.52}$$

As one can see from Eq. 2.51, the maximum system response to the plasma density fluctuations is achieved when $\Phi_0 - \Phi_{ref} = \pi/2$. Under this condition,

$$I_{interferometer} = \frac{c}{8\pi}\frac{|E_0|^2}{2}\Big[1 - \Delta\cos(k_p x)\Big]. \tag{2.53}$$

Comparing this to the response of the PCI system (Eq. 2.32) one can see that the interferometric imaging system has nearly identical performance. The overall image brightness is just factor of 2 lower (primarily due to some energy loss when the probing and the reference beams are recombined using a beamsplitter). The image contrast ($\delta I/I$) is also factor of 2 lower.

The disadvantage of the interferometer technique lies in its dependency on Φ_{ref}. Preferably, this quantity should stay constant to within much smaller than $|\Delta|$ value.

Unfortunately, vibrations in the system affect Φ_{ref}. For the fluctuations investigated in this thesis the value of Δ is typically 10^{-3} or smaller and the optical wavelength of the laser radiation is 10.6 μm. This requires the distances between the interferometer mirrors not to change by more than $\ll$ 10 nm, an impossible requirement on $5m$-scale machine with 300 MW pulsed magnets, such as Alcator C-Mod, or on any other possible plasma fusion device. This problem may be partially solved by noting that the vibrations and typical fluctuations of interest occur at different frequencies (<1 kHz for the vibrations, >10 kHz for fluctuations) and can easily be separated by simple signal analysis.

However, there is another requirement. As seen from Eq. 2.51 the responsivity of the interferometric imaging system is proportional to $\sin(\Phi_0 - \Phi_{ref})$. If $\Phi_0 - \Phi_{ref}$ changes by comparable to $\pi/2$ or greater amount the responsivity will be completely altered. To prevent this, the interferometer mirrors should not move by more than $1 \sim 2$ μm, which is also impossible to achieve. For comparison, the PCI tolerance to vibrations is about 50 μm (it should be smaller than the laser spot size, as will be discussed later in the section 2.2.7). To complicate the matter, Φ_0 changes from 0 to 1-1.5 during a typical C-Mod discharge, making the use of interferometer impossible even in the absence of vibrations.

On the contrary, the phase contrast imaging system is completely insensitive to changes in Φ_0. Since there is no separate reference beam in the PCI, it is also does not depend on Φ_{ref}. As it is sometimes called, the phase contrast is the "internal reference interferometer" technique. The image is created by interference of the scattered waves with the unscattered main beam, which is used as the internal reference beam in this case. Since the scattered waves and the reference beam propagate through the optical system and the plasma together, their relative phases are not affected by the mirror vibrations and the phase delay Φ_0 introduced by the plasma.

The advantage of the interferometer system is the ability to measure long wavelength fluctuations. It does not have the limitation of the PCI diagnostic which is sensitive only to fluctuations with wavelength shorter than the beam diameter (this is a theoretical limit that originates from the system layout and the laws of optics; it

will be derived later in section 2.2.7).

As one realizes by now, building an interferometric imaging system for the purpose of plasma diagnostic is a very demanding task, but not entirely impossible. Nazikian and Sharp implemented such a system on the LT-4 tokamak[37]. Besides carefully designing the system for minimized vibrations and temperature drifts, they had to resort to using active feedback stabilization. One of the mirrors in their system was controlled by a piezo actuator to counteract the effect of vibrations, temperature expansion and Φ_0 change. It was set up to keep $\Phi_0 - \Phi_{ref}$ as close to $\pi/2$ as possible at all times to guarantee constant (and also the maximum) system responsivity.

An interesting regime of interferometer operation is when $\Phi_0 - \Phi_{ref} = \pi$ (see equation 2.52). In this regime the interferometer image contrast becomes infinitely high, but the intensity variations are proportional only to the square of the plasma density fluctuations and therefore very small and would be hard to measure. The response function in this case is nearly identical to that of the central dark ground technique (Eq. 2.35) with some loss in intensity due to the use of beam splitters. Additionally, in this regime the interferometer is much more sensitive to the mirror vibrations - this is probably the main reason why this regime is rarely used.

The phase contrast imaging was selected over the interferometric system for fluctuations research on the Alcator C-Mod tokamak. The ability of the interferometer to detect longer fluctuation wavelengths was not important. The width of the PCI laser beam (up to 19 cm) already allowed measurements of all basic fluctuations of interest. However, the PCI reduced sensitivity to vibrations was of much greater importance because of the big size and large magnetic fields and currents of the C-Mod tokamak.

2.2.6 Phase Contrast Imaging vs. Small-Angle Scattering

Another widely used technique for researching plasma density fluctuations is *small-angle laser scattering*. Like phase contrast imaging, it is based on the principles of electromagnetic wave scattering described earlier in section 2.1, but there are some differences in the optical design. These differences define different areas of application of each technique. For a detailed discussion of small-angle CO_2 laser scattering sys-

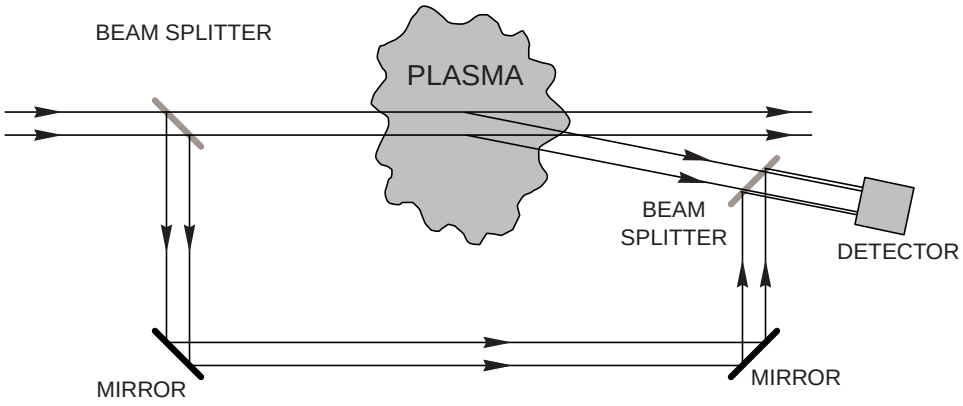

Figure 2-8: Optical setup of the simple heterodyne small-angle scattering system.

tems one should refer to an excellent review paper published by Slusher and Surko[38]. This section will just provide a brief introduction to this technique and its advantages and disadvantages over the PCI.

Fig. 2-8 illustrates the optical setup of the simple small-angle scattering system. A laser beam passes through the plasma from left to right and a part of it scatters from density fluctuations. A radiation detector is then positioned to the side of the main beam to detect the intensity of these scattered components. The position of the detector makes it sensitive only to the radiation scattered at a certain small angle, which, in turn, defines the wave number of the density fluctuations that caused this scattering (according to equations 2.9 and 2.10). A part of the original beam is split off and then mixed with the scattered beam on the detector by means of two beam splitters. This is called *heterodyne* scattering. The purpose of the "reference" beam is dual. First, since the frequency of the scattered beam differs from the frequency of the original beam (again, Eqs. 2.9 and 2.10), the interference generates modulations in the measured signal at the frequency of the plasma density fluctuations. Otherwise, only the wave number of the fluctuations can be measured and all the frequency information would be lost. Second, from Eq. 2.25 the scattered beam intensity is proportional to the fluctuation amplitude squared and typically would be very small. By interfering the two beams, the signal becomes proportional to the first power of Δ and therefore much easier to detect.

When comparing small-angle laser scattering and PCI (figures 2-3 and 2-8) one can

immediately see one important difference: in the scattering system the scattered beam should completely separate from the incident beam before being detected. Typically, this requires higher scattering angles than the PCI system, and means higher wave numbers (i.e. shorter wavelengths) of the detectable plasma density fluctuations. The maximum detectable fluctuation wavelength is

$$\lambda_p^{max} = \sqrt{\lambda_0 L}\ , \tag{2.54}$$

where λ_0 is the laser wavelength and L is the distance from the plasma to the detecting plane ($L \approx 5$ m for the Alcator C-Mod tokamak). In case of a CO_2 laser equation 2.54 limits the small-angle scattering system to wavelengths of a few millimeters. Of course, one can use a longer wavelength far-infrared laser or a microwave source[39] to increase λ_p^{max}, but then one loses in the detectable λ_p range as λ_p^{min} approaches λ_p^{max}. Also, one then has to deal with the refraction effect of the plasma and still cannot reach λ_p^{max} of the PCI system by at least a factor of two because of the finite size of the openings in the tokamak walls.

In practice, the small-angle scattering system is used to study short wavelength plasma fluctuations (typically $\lambda_p \leq 5$ mm) while the PCI is better suited for the fluctuations in 0.1-10 cm range. For the Alcator C-Mod tokamak, where most fluctuations of interest to date have a wavelength of $\sim$1 cm or larger, the phase contrast imaging system proved to be a better choice.

2.2.7 Diffraction Effects in the PCI System

As was discussed earlier in section 2.2.2 the phase contrast imaging system relies on focusing the scattered and unscattered waves into three different spots in the focal plane of the first imaging lens. Unfortunately, one has to account for the diffraction effects that limit the minimal size of the focal spots. Under certain conditions, these spots begin to overlap and the phase contrast technique cannot be longer used effectively. This section provides careful evaluation of these effects. Recommendations will be given on how to maximize the system performance under the conditions when

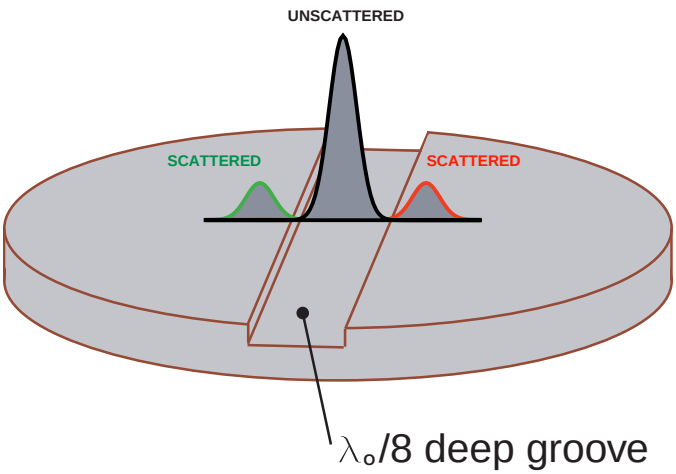

Figure 2-9: A finite size of the focal spots is due to the diffraction effects.

diffraction effects become significant.

Figure 2-9 illustrates the typical shape of the focal spots on the phase plate. Note that the phase plate is of the reflective type (more on the phase plate design will be provided in the next section [2.2.8]). The shape of the focal spot is determined by the intensity profile of the laser beam. Gaussian-shaped beams are known to provide the smallest size focal spots – a gaussian beam of diameter D when focused generates a gaussian shaped focal spot of the diameter:

$$d = \frac{4}{\pi}\frac{F\lambda_o}{D} \ , \tag{2.55}$$

where F is the focal length of the first imaging lens and λ_o is the optical wavelength of the laser (10.6 μm). D and d are the diameters inside $1/e^2$ points on the intensity profiles.

Now we need to compare the focal spot size d with the width w of the $\lambda_o/8$-deep groove on the phase plate and with the separation s between the centers of the scattered and unscattered spots. From Eq. 2.25 the angle between directions of propagation of the two waves is λ_o/λ_p and therefore:

$$s = \frac{\lambda_o}{\lambda_p}F = \frac{D}{\lambda_p}\frac{\lambda_o F}{D} \ . \tag{2.56}$$

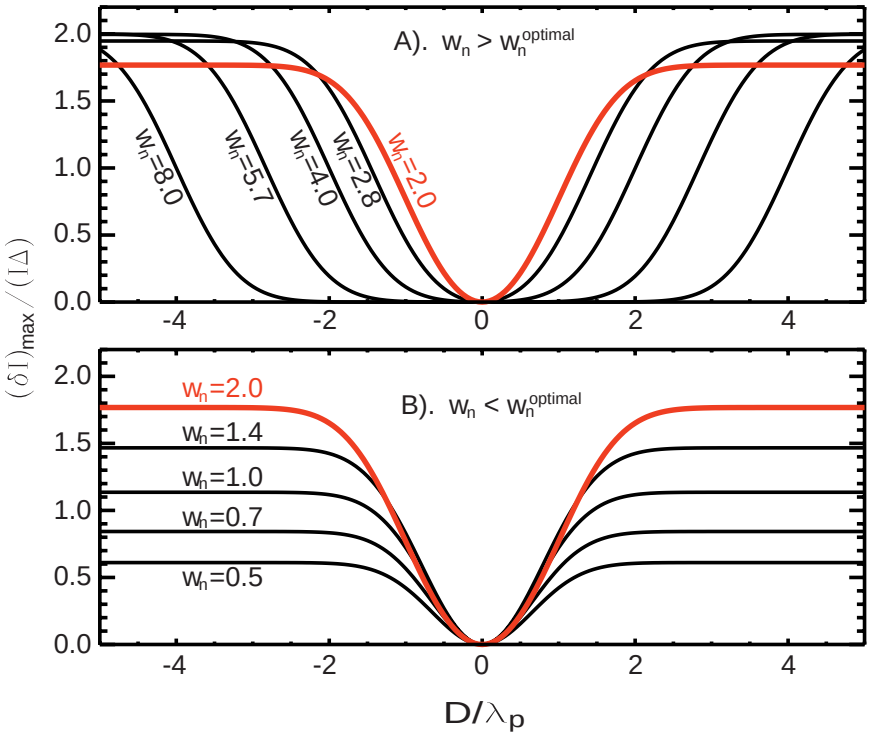

Figure 2-10: A responsivity of the PCI system vs. the number of plasma fluctuation wavelength per beam diameter for various values of the phase plate groove width.

To get a good response from the PCI system it is better to have nearly 100% of the center focal spot within the phase plate groove. At the same time, the side spots should be as completely as possible beyond the groove width. Overall, this translates into:

$$d \ll w \ll 2s \tag{2.57}$$

or, after dividing by $(\lambda_o F/D)$:

$$4/\pi \ll w_n \ll 2D/\lambda_p \ , \tag{2.58}$$

where $w_n = w/(\lambda_o F/D)$ is the normalized groove width. So the PCI system is capable of producing good response when $D/\lambda_p \gg 1$. But to understand what is happening when D/λ_p is of the order of 1 or less a numerical analysis had to be carried out. The resulting responsivity of the system vs. D/λ_p is plotted in Fig.2-10 for a number of values of w_n. As one can see, when the groove gets very wide (Fig.2-10a) the

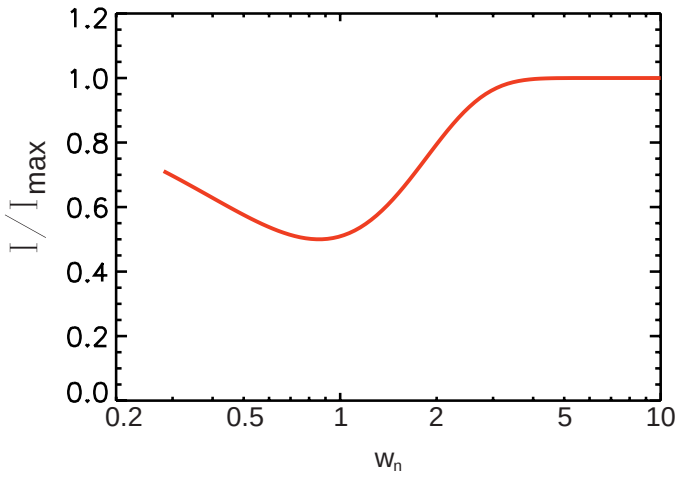

Figure 2-11: A level of the non-varying intensity in the center of the PCI system image plane as a function of the normalized phase plate groove width.

system becomes insensitive to large wavelength of the plasma density fluctuations. The reason for such behavior is that when w_n is large the side focal spots begin to appear partially (or even completely) within the groove, canceling the phase effect. This basically cuts off all the plasma fluctuation wavelengths longer than $\sim 2D/w_n$.

On the other side, when the groove is very narrow (Fig.2-10b) it delays (by $\pi/2$ in phase) only a part of the central unscattered focal spot. Since only the delayed part is in phase with the scattered waves and can interfere with them, the system responsivity drops for all values of λ_p. Moreover, for λ_p of order of D or longer there is now a significant contribution from the interference between the non-delayed part of the central spot and the delayed parts of the side spots. This interference tends to cancel the system response (and cancels it completely when $\lambda_p \to \infty$). The result is that the wavelengths $\lambda_p > D$ are cut off even when w_n is small.

At low values of w_n there is another undesirable effect when the groove is narrower than the focal spot, which is then only partially delayed by $\pi/2$ in phase. The interference between the delayed and non-delayed parts of the spot causes the beam to diverge differently than it should in the geometrical optics approximation. This causes some unwanted (generally non-linear) distortions, such as a drop in the non-varying image intensity level (Fig.2-11). The image becomes larger, darker and non-gaussian. There is no more simple point-to-point translation between the object and the image

planes of the PCI system. This is definitely not a favorable mode of operation.

Since very large and very low values of the phase plate groove width are not suitable, there should be some optimal width $w^{optimal}$ somewhere in between. The exact value of $w^{optimal}$ depends on one's preferences, but the following value should be sufficient for the most of applications (as seen in Figs. 2-10 and 2-11):

$$w^{optimal} = 2.0\frac{\lambda_o F}{D} \qquad (\text{i.e. } w_n^{optimal} = 2.0)\ . \tag{2.59}$$

If higher responsivity and more linearity is needed it may be better to use a slightly higher value of $w_n \approx 2.5 - 3$. Somewhat lower values of $w_n \approx 1.5$ may be used when long wavelength fluctuation detection capability is of primary importance.

The width of the groove defines the high cut off in wavelength for detectable plasma fluctuations. For $w_n = 2.0$ the $-3\ dB$ cutoff is:

$$\lambda_p^{max} = 1.075 \times D \approx D. \tag{2.60}$$

In the Alcator C-Mod PCI system $D = 15$ cm, $\lambda_o = 10.6$ μm and $F = 203\ cm$ $(80'')$ which results in

$$w^{optimal} = 2.0 \times \frac{\lambda_o F}{D} = 287\ \mu\text{m}\ ; \qquad \lambda_p^{max} = 16\ \text{cm}. \tag{2.61}$$

2.2.8 Phase Plate Design

The phase plate is the most important element in the PCI system. It is the part that gives the phase contrast technique its unique properties and advantages over other diagnostics. Different phase plate designs and ways to manufacture are described in this section.

There are two ways to make a phase plate. The first way was described earlier in section 2.2.2. The phase plate in this case transmits all the radiation through, but the unscattered light passes through some extra layer of optically dense material, and its phase is delayed. Unfortunately, this would require some complicated polishing

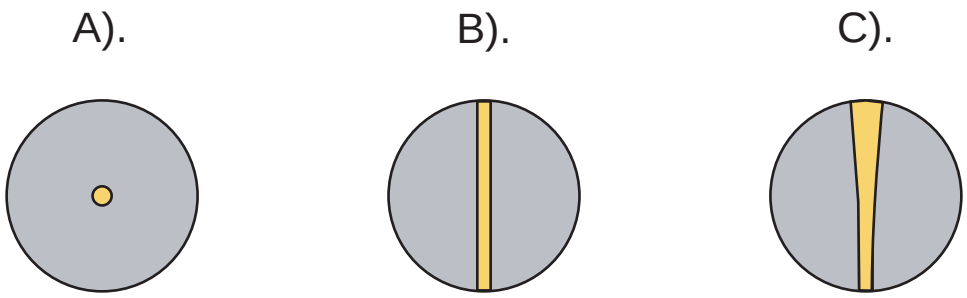

Figure 2-12: Different shapes of the phase plate grooves.

and there are no easily available manufacturing techniques to produce such a plate.

An alternative method is to make a "reflective" phase plate. This plate is basically a mirror with its center portion deepened by $\lambda_o/8$ (Fig. 2-9). The unscattered wave is focused on this indentation and is delayed by a quarter wavelength relative to the scattered waves when reflected. The advantage of this design is the ease of manufacturing. One can take a mirror, cover its center area with some form of a mask and deposit a $\lambda_o/8$-thick reflective metal layer on the rest of the mirror. The metal deposition techniques are readily available and the layer thickness can be controlled with a great degree of accuracy.

Different kinds of the "reflective" phase plates exist based on the shape of the center indentation. Ideally, it should be a circle about the size of the central focal spot (Fig. 2-12a). A system with the plate with such indentation is capable of producing complete 2-dimensional (2D) images.

However, in a strongly magnetized plasma (such as the plasma in Alcator C-Mod) the fluctuation pattern is strongly 1-dimensional when viewed across the magnetic field lines. Therefore the 1-D imaging system should be sufficient for such application. The main advantage of the 1D PCI is that a linear detector array may be used instead of a full 2D matrix, which reduces the cost of the detector along with the number of the required amplifier and digitizer channels and the stored data volume. For this 1D PCI system a different phase plate should be used, where the indentation is made in a form of a groove or a stripe (see Fig. 2-12b). When one needs to work with the beams of different diameters, a phase plate with a V-shaped groove (Fig. 2-12c) may be utilized. By focusing the beam on upper or lower parts of the plate one can quickly

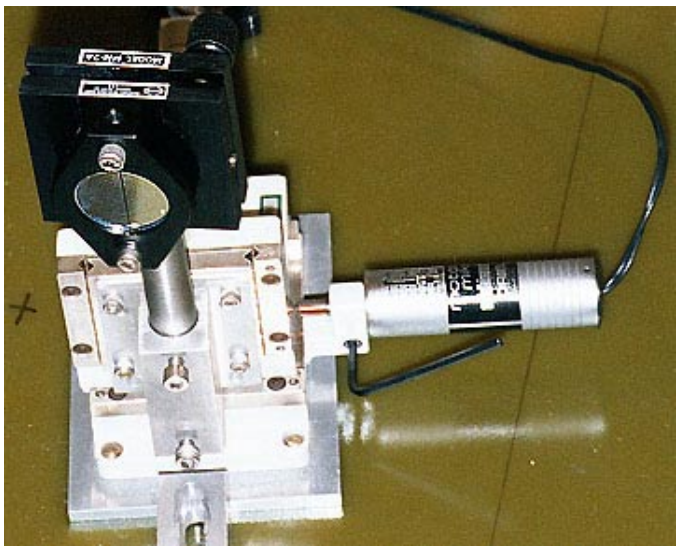

Figure 2-13: Photograph of the phase plate used in the Alcator C-Mod PCI system.

change the groove width as required in accordance with eq. 2.59. In the C-Mod PCI system plates with both straight and V-shaped grooves are used. The groove width is 286 μm for the straight groove plate (optimized for $D = 15$ cm beam and large λ_p^{max}) and $400 - 2000$ μm for the V-shaped one (for ease of alignment when looking for short wavelength fluctuations).

One of the actual phase plates used in the C-Mod system is shown in Fig. 2-13. For the purpose of the system alignment it is attached to a 2D tiltable mount, and the mount itself is fixed on a 3D translation stage. One of the stage movements is controlled by an electric motor, the other two are controlled manually. The motor is needed to remotely control the position of the unscattered wave focal spot, which should always be centered on the phase plate groove. The position of the spot tends to drift somewhat during the C-Mod run day and needs to be readjusted between the shots.

The cross section of the actual phase plate is shown in figure 2-14. It is made out of a Zinc-Selenite (ZnSe) window that has $\lambda_o/8$ metal coating on the front side (except for the groove) and antireflective coating on the back side. The metal coating is either protected gold or protected aluminum. Gold is a better choice since it has higher reflectivity at 10.6 μm: 99.5% vs. 98% for aluminum. Higher reflectivity means

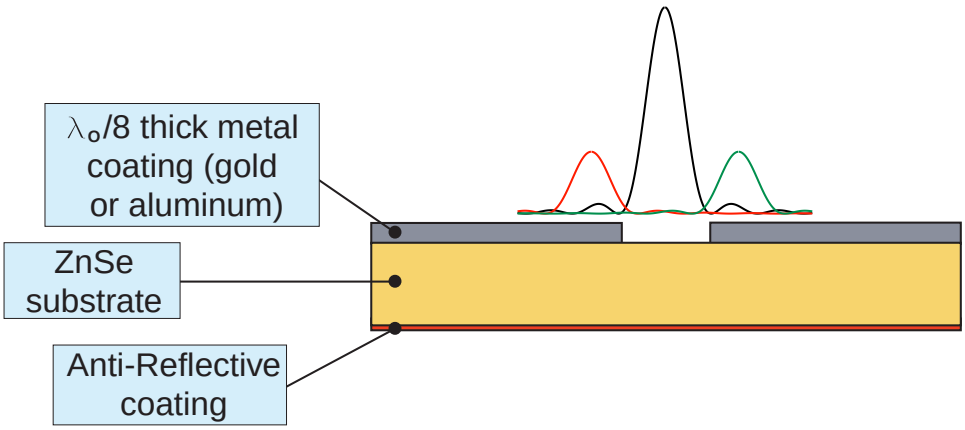

Figure 2-14: Cross section of the phase plate.

less absorption and less probability of surface damage, since on the phase plate the laser beam is focused and its power per unit area is extreme.

Up to now we considered that the reflection coefficient is 1 everywhere on the phase plate. However, the actual plate substrate material (ZnSe) is transparent for the CO_2 laser light. It has the index of refraction of N=2.4028 and the reflection coefficient of only R=0.1699 (at 10.6 μm normal incidence). The groove not only delays the phase of the reflected wave by $\pi/2$, but also reduces its amplitude by a factor of $1/\sqrt{R}$. The reason for such design is dual. Primarily, a transparent substrate is needed to monitor the position of the central focal spot relative to the groove. By placing a power meter behind the phase plate one can measure the amount of the laser light hitting the grove. The alignment is right when this amount is maximal. The anti-reflective coating is needed to eliminate secondary reflections that would introduce uncertainty into the phase of the reflected light.

The second reason for using reflection from ZnSe is that the contrast of the image is then increased. The first term in eq. 2.31 now should be multiplied by an additional factor of $\sqrt{R}$, resulting in the image intensity of

$$I_{PCI+ZnSe} \approx R\frac{c}{8\pi}|E_0|^2(1+\frac{2\Delta}{\sqrt{R}}\cos k_p x) \ . \tag{2.62}$$

When compared with the original intensity (eq. 2.32) one can see that the image contrast is now indeed a factor of $1/\sqrt{R}$ higher, albeit the overall image intensity

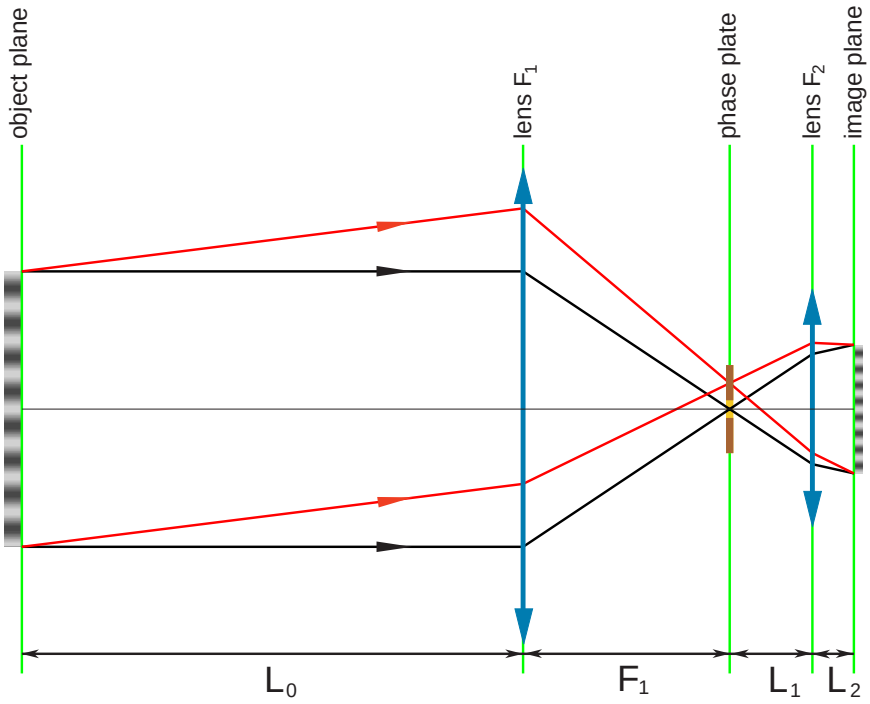

Figure 2-15: Optical layout of the PCI system with an arbitrary magnification coefficient.

drops. It will be shown later in the section 2.2.10 that the main source of the noise in the system the laser itself. Therefore, increasing the image contrast (even at the expense of the image intensity) immediately improves the signal-to-noise ratio.

2.2.9 Arbitrary Imaging System

The previously mentioned example of a PCI system (Fig. 2-3) has a magnification coefficient of $M = 1$ (for simplicity) , i.e. the image has exactly the same dimensions as the object. This is not always practical, since most detector elements are $\sim$1 mm in size or less and are not well suited for detection of plasma fluctuations with $\lambda_p > 1$ cm in such a system. Therefore one needs to construct a system that would reduce M (and the image size) to some manageable value. Another advantage of reducing the image dimensions is that it increases the image brightness and makes the signal detection easier. This section covers the optical layout of the PCI system with an arbitrary magnification coefficient.

Figure 2-15 illustrates such a system. The difference from the early example is that

the focal lengths of the lenses and the distances between the system components (at least L_0 and L_1) are now allowed to be arbitrary. Also, the scattered and unscattered waves have now generally spherical wavefronts when they combine in the image. This significantly changes the wave phase and amplitudes in eq. 2.31. However, the relative phases of the waves stay the same, and therefore the intensity equation (eq. 2.32) is modified only slightly. Specifically, the overall image intensity goes up by a factor of $1/M^2$ and the image dimensions are reduced by $1/M$ (once again, M is the magnification coefficient, i.e. the ratio of the image size over the object size).

For the PCI system to work, the scattered and unscattered waves should converge into the same space, and this fixes L_2 to some function of (F_1, F_2, L_0, L_1). This function can be easily found from the laws of geometrical optics. After some simple mathematics one would get:

$$L_2 = \left[\frac{1}{F_2} + \frac{L_0 - F_1}{F_1^2 - L_1(L_0 - F_1)}\right]^{-1} . \tag{2.63}$$

L_0 and F_1 are fixed by the system design ($L_0 = 493$ cm and $F_1 = 203$ cm) and cannot be changed. One is left to vary L_1 and F_2 in order to obtain the desired magnification. A plot of L_2 vs. L_1 for 3 different values of F_2 is shown in Fig. 2-16(a). The system magnification may be found from geometrical optics as well:

$$M = \frac{L_1}{F_1}\left[1 - \left(\frac{1}{F_2} - \frac{1}{L_1}\right)L_2\right] . \tag{2.64}$$

Magnification M as a function of $(L_1 + L_2)$ and F_2 is shown in Fig. 2-16(b). $(L_1 + L_2)$ is chosen for the horizontal axis since this parameter is usually hard to change (it involves repositioning the detector array).

Another important property of the system is the depth of focus, or how much one can move the detector plane before the image starts to degrade. When the detector and the image plane are separated by the distance s the scattered waves do not overlay the unscattered wave correctly. What happens is basically *phase scintillation* (see section 2.2.4) and the image contrast changes. To prevent this effect

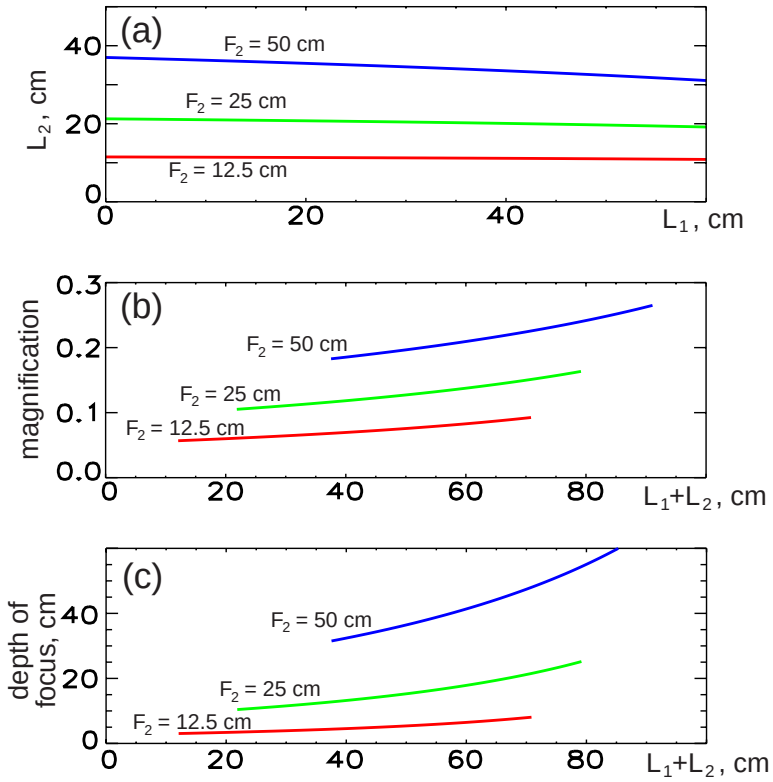

Figure 2-16: Parameters of the PCI system for different configurations.

the separation between the scattered and unscattered waves should be significantly less then $M\lambda_p/2\pi$ ($1/2\pi$ of the imaged size of the fluctuation wavelength λ_p). This may be shown to be equivalent to:

$$s < \frac{\lambda_p^2 M L_2}{\lambda_o(F_1 + L_1 - L_0 L_1/F_1)}. \tag{2.65}$$

Plots of this value vs. $(L_1 + L_2)$ and F_2 for $\lambda_p = 1\ cm$ (most fluctuation wavelengths are around this size or larger) are shown in Fig. 2-16(c). As one can see the depth of focus is usually quite large and the system should be easy to align. Table 2.1 summarizes the typical parameters of the actual C-Mod PCI setup.

An interesting result may be obtained when one removes the F_2 lens (assume $F_2 = \infty$). A valid PCI system still may be built with just one lens. However, in this case the values of

$$L_1 + L_2 = \frac{F_1^2}{L_0 - F_1} \quad \text{and} \quad M = \frac{F_1}{L_0 - F_1} \tag{2.66}$$

F_1	203 cm
F_2	25 cm
L_0	493 cm
L_1	25 cm
L_2	20.6 cm
M	0.123
s	<14.3 cm

Table 2.1: Actual parameters of the C-Mod PCI optical setup.

become too large to be practically usable on C-Mod (142 cm and 0.7 respectively).

The PCI system in this example is built with lenses and a transparent phase plate. However, the same analysis still applies when parabolic mirrors and a reflective phase plate are used (as in the real C-Mod system).

2.2.10 Responsivity and Signal-to-Noise Ratio of the PCI System

The performance of the phase contrast imaging system depends strongly on the kind of the detecting element used. In systems employing a CO_2 laser (which emits light at 10.6 μm) semiconductor detectors proved to work well, providing a good combination of responsivity and signal-to-noise ratio.

There are two major classes of semiconductor light detectors: *photoconductive* and *photovoltaic*. Both kinds rely on the formation of free charge carriers when a photon of light is absorbed. The difference is that photoconductive detectors are made out of the same (usually n-type) material and operate under some external constant current (the *bias* current). When illuminated, the resistance of such detectors drops and this changes the voltage across the element. The photovoltaic detectors, on the other hand, are made out of a p-n junction. They can operate in *voltage* mode, when the birth of hole-electron pairs generates voltage across the junction, or in *current* mode, when a reversed *bias* voltage is applied and the pair formation causes an increase in the current.

Both kinds of detectors were considered for use in the Alcator C-Mod PCI system. Photoconductive detectors typically have the advantage of lower price, higher respon-

Detector type	photoconductive, HgCdTe, linear array
Manufacturer	Belov Technology Inc.
Model Number	B12N-32A-20
Number of elements	32
Element width	750 μm
Element height	1000 μm
Element separation	100 μm
Frequency response	DC - 10 MHz
Bias current (per element)	30 mA
Field of view	60°
Responsivity (per element)	1500-1600 V/W
Peak responsivity λ	≈ 10 μm
D^* (per element)	4×10^{10} cm$\sqrt{\text{Hz}}$/W

Table 2.2: Specifications for the Alcator C-Mod PCI detector array.

sivity and, when manufactured as an array, have much better uniformity between the elements. Photovoltaic detectors, on the other hand, have much better frequency response (up to 1 GHz vs. $\sim$10 MHz for photoconductors). Since operation at very high frequencies was not needed, the 32-element photoconductive detector array (manufactured by Belov Technology Inc., model number B12N-32A-20) was finally selected for its combination of price and performance. Table 2.2 lists specifications for this detector. Only 12 central channels of the array are currently used, the rest is needed for future upgrades. Each used channel is hooked up to a preamplifier which supplies the needed bias current and provides additional gain of ~ 200. The exact value of the gain is fine tuned so that each combination of the detector element and the preamplifier has the same combined gain of 3.0×10^5 V/W.

There are four sources of noise in the PCI system: the CO_2 laser, the detector elements, the preamplifiers and the digitizers. Figure 2-17 illustrates the spectral density of the squared RMS voltage for these sources. Curve (e) represents just a digitizer noise, i.e the noise in the system when the laser and preamplifiers are powered off. It is a combination of the *ideal bit-noise*, noise in the internal digitizer circuitry and "pick up" in the cables. Ideal bit-noise (line (f)) is associated with the finite resolution of the digitizer (2^{12} bins over $-5... + 5$ V range). The smallest

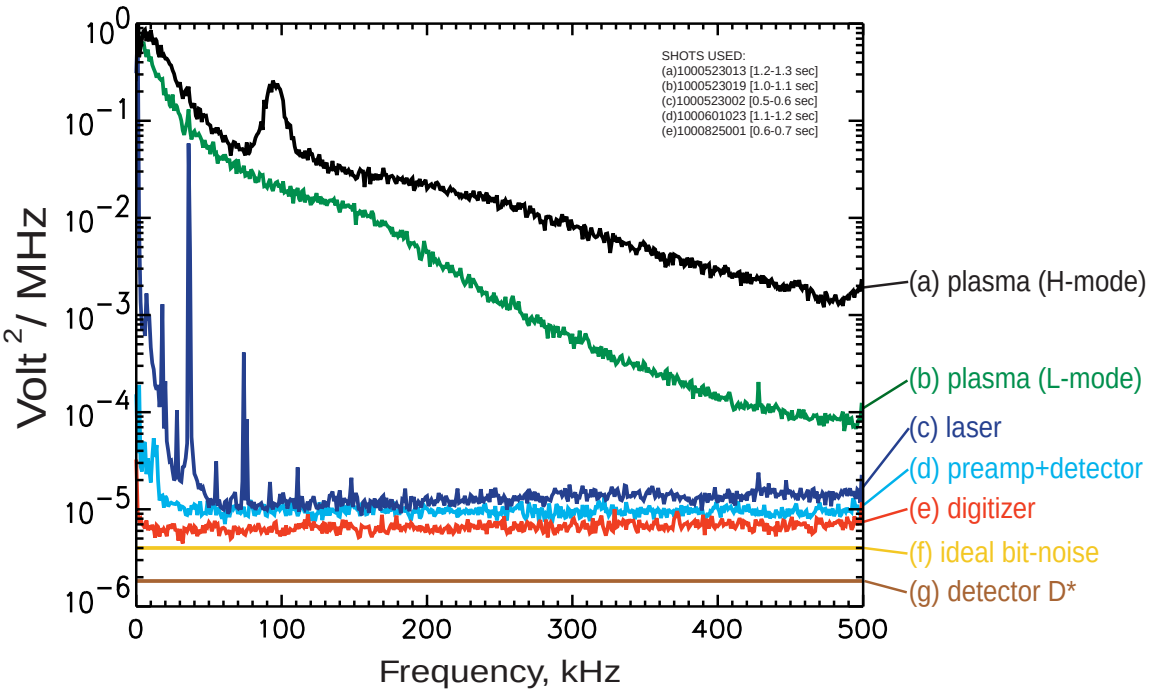

Figure 2-17: Spectral density of the squared RMS voltage for different sources of noise and signals in the Alcator C-Mod PCI system.

increment of the digitizer is just 2.44 mV, the result of which is that the digitizer on average is 1.22 mV off the real value. This noise is uniformly distributed from DC to the digitizer Nyquist frequency (500 kHz).

Figure 2-17, curve (d) represents the noise in the system when the preamplifiers are powered on. It is combination of noise from the digitizers, the preamplifiers and the detectors. The detector noise in turn is a combination of *Johnson* noise, *shot* noise, *photon* noise, *generation-recombination* noise, $1/f$ noise and *temperature* noise [40]. To reduce this noise the detector is cooled down to the liquid nitrogen temperature (77 K). It is common to describe a combined amount of noise in a detector by specifying the normalized detectivity

$$D^* = \frac{\sqrt{A_d \Delta f}}{P_{noise}}, \tag{2.67}$$

where A_d is the active area of the detector element, Δf is the frequency bandwidth and P_{noise} is the equivalent power of light needed to produce the same response as the noise. D^* of the PCI detector array has been specified to be no less than

4×10^{10} cm$\sqrt{\text{Hz}}$/W per element. Line (g) shows the spectral density of the noise derived just from the D^* alone. As one can see, the detector noise is negligible compared to the other sources in the system.

Finally, in Fig. 2-17, curve (c) represents the noise in the system when the CO_2 laser is also turned on. The laser introduces noticeable amount of additional noise, especially at $f < 100$ kHz. It also has some continuous oscillation at 38 kHz (and its harmonics) of an unknown origin. This oscillation is strong enough to show up in the final signal, and it needs to be filtered out or just disregarded in the final analysis.

The signal-to-noise ratio (SNR) of the PCI system can be evaluated by comparing the spectral density of the actual plasma signals and the noise. Fig. 2-17, curves (a) and (b) represent one the strongest and one the weakest signals typical for the Alcator C-Mod plasmas. The SNR ranges from ~ 100 (at $f < 150$ kHz) to 3-10 (at $f \approx 500$ kHz). The tendency of the plasma signals to fall off with frequency can be attributed to the line-integrated nature of the PCI measurements. Higher frequency density fluctuations usually have smaller wavelengths and tend to average out when integrated.

2.3 The PCI System Implementation on Alcator C-Mod

Currently, the phase contrast imaging diagnostics has been implemented on a number of plasma fusion devices (see section 2.2.1 for the full list). However, the unique properties of the Alcator C-Mod tokamak (such as its dimensions, accessible ports, available space nearby, etc.) require that the PCI diagnostic be largely redesigned to fit specifically this machine. This section reviews the hardware part of the experiment.

A sideview of Alcator C-Mod and the location of the key PCI components are shown in Fig. 2-18. The CO_2 laser and beam expansion optics are located on the ground next to the machine. The beam travels from this table to a mirror (located underneath the tokamak) and then reflects upward into the vertical access port. After

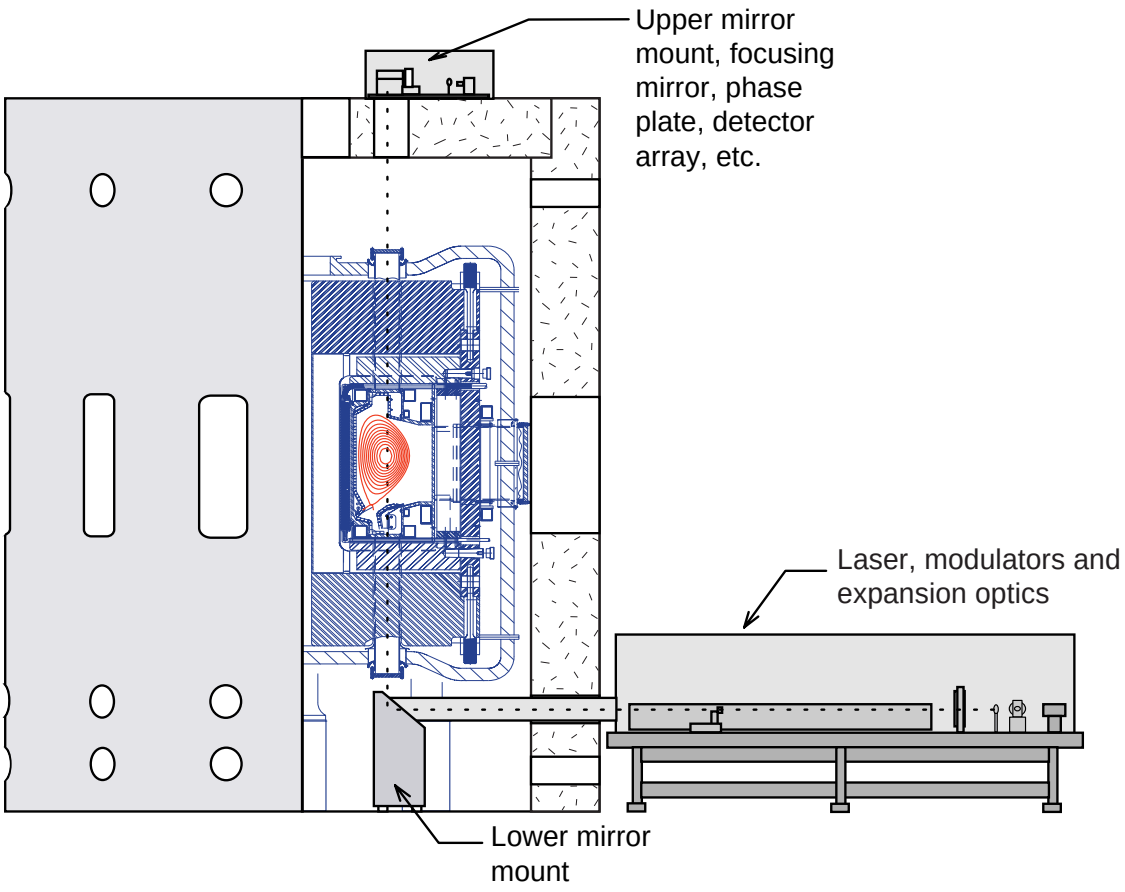

Figure 2-18: Location of major PCI components around the Alcator C-Mod tokamak.

passing through the plasma, the beam reaches an enclosure on top of the C-Mod *igloo* (the 2-foot thick concrete structure surrounding the machine). Inside this enclosure are the imaging optics and the detector array with preamplifiers.

It should be mentioned, that no optical parts of the diagnostic (except for two vacuum break windows) are attached to the machine itself, thus greatly reducing unwanted vibrations in the system. Also, for the safety reasons, the beam is completely enclosed everywhere along its path.

2.3.1 Beam Generation and Expansion

The PCI system requires a collimated monochromatic optical beam to operate. The beam width determines the size of plasma fluctuations that can be detected (Eq. 2.60). On C-Mod, the beam width was chosen to be 19 cm (limited only by the width of the vertical access ports), primarily to allow measurements of the long wavelength fluctuations associated with the ion cyclotron range of frequencies (ICRF) waves.

A beam of such properties is obtained by using a laser and special expansion optics. All the required components are located on the $3.04\,\mathrm{m} \times 0.91\,\mathrm{m}$ optical table on the lower level of the Alcator C-Mod cell, as shown in Fig. 2-19. During the normal operation, the table is completely enclosed (Fig. 2-19(a)). This is required by the safety regulations (to prevent stray scattering of the laser light) and needed to minimize dust collection on the optical surfaces.

The component layout drawing is shown in Fig. 2-20. The largest piece on the table is the 100 watt continuous CO_2 laser manufactured by MPB Technologies, model IN-100. The laser is pumped by $\sim$ 1 kW glow DC discharge. A closed loop water chiller underneath the table provides the required cooling for the laser.

The unexpanded laser beam can have a power density in excess of 1 $\mathrm{kW/cm^2}$ and, if misaligned, it causes immediate damage to skin, plastics and painted surfaces. Therefore, a chopper with 1:12 duty cycle is used to significantly reduce the average power of the beam during alignment. The chopper is removed from the beam path when the system is aligned and ready to operate.

A few flat surface mirrors used to steer the beam are made of a copper base

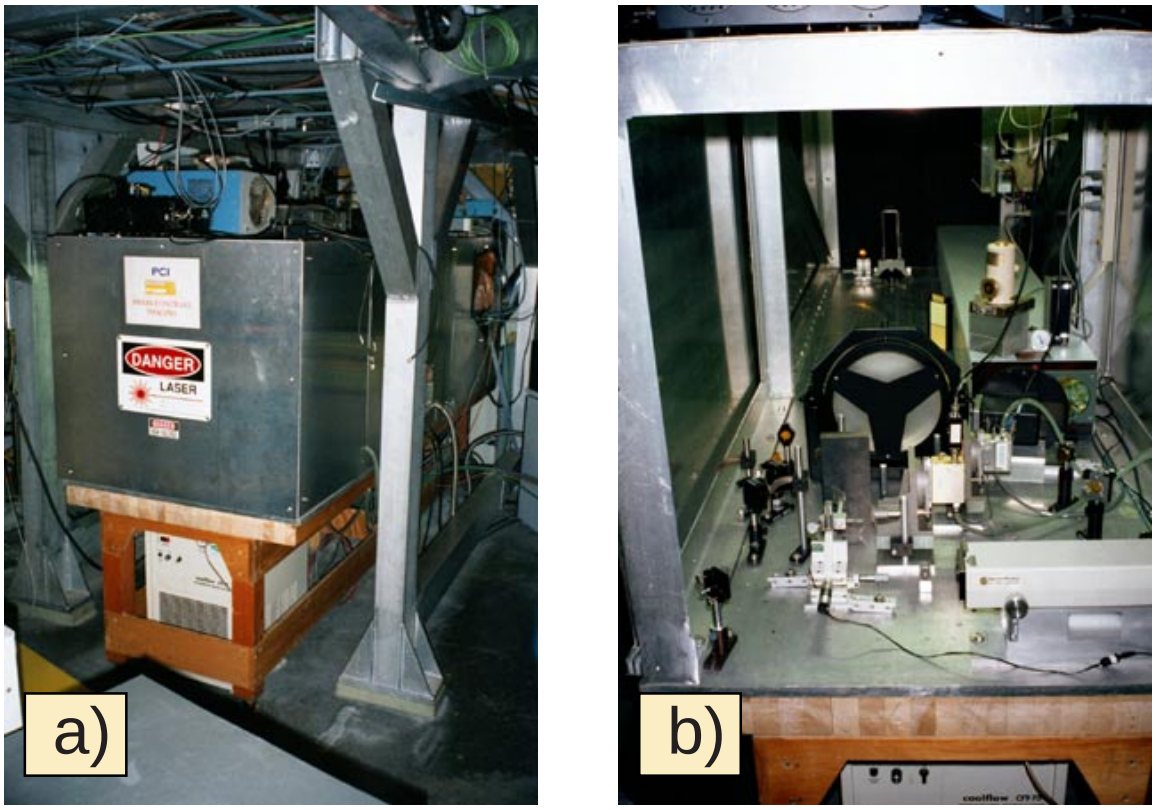

Figure 2-19: The optical table housing the CO_2 laser and the beam expansion optics.

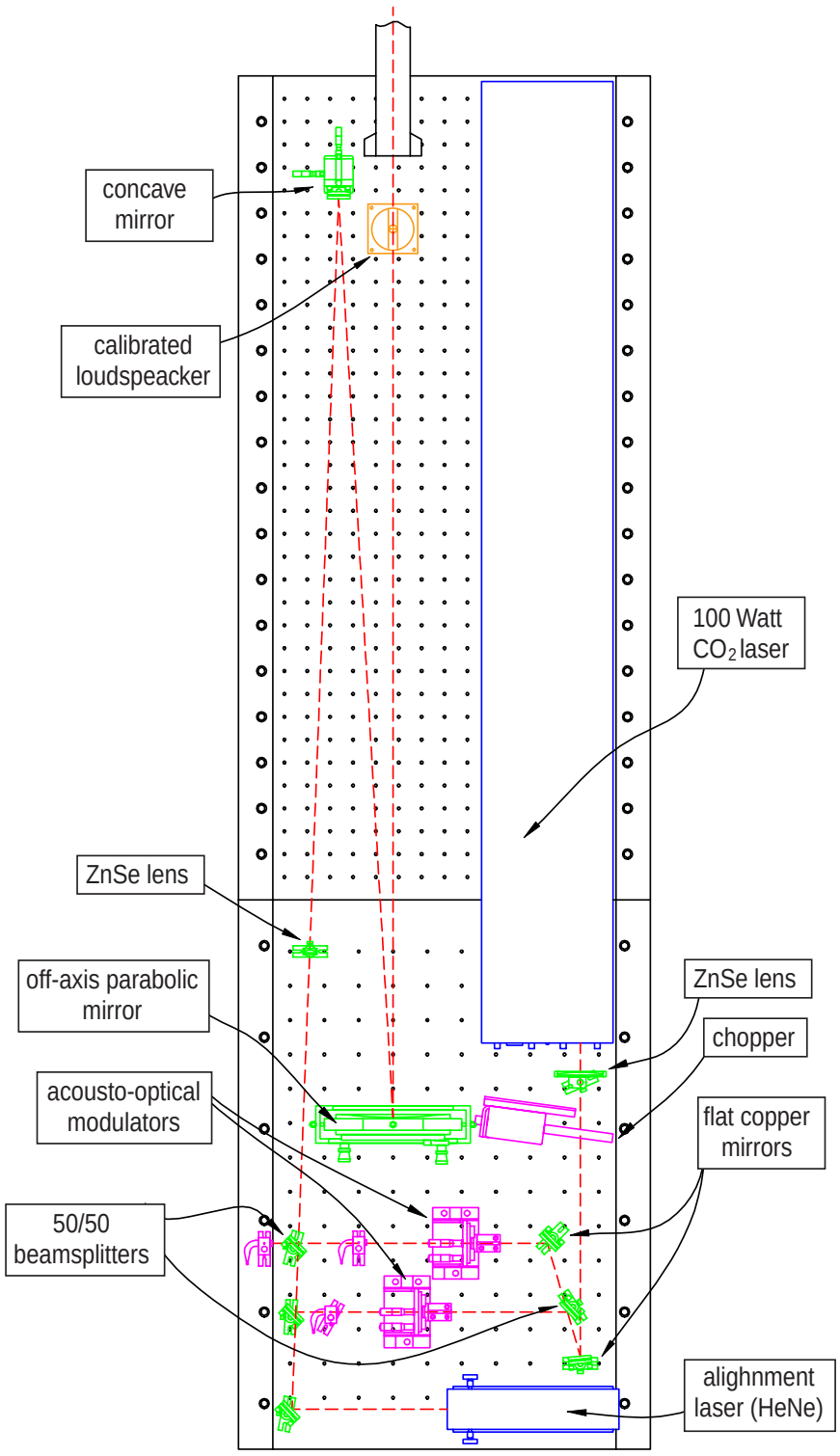

Figure 2-20: Layout of the optical components on the PCI lower table.

and then gold coated. The gold has a superior reflection coefficient for the infrared light (99.5% at 10.6 μm) and the copper provides excellent heat conduction. Such precautions are necessary to prevent uneven heating of the mirrors, which may cause the surface deformation (and therefore beam distortion) or even damage to the coating layer.

The beam is split into two parts and then recombined by means of the two 50/50 beam splitters. This is needed to introduce the high frequency beam modulation as needed for optical heterodyning, see chapter 4 for detailed discussion on this subject.

Since radiation of the CO_2 laser is invisible to the human eye, a set of special thermosensitive plates is used to perform the initial beam alignment. Further, a visible Helium-Neon laser light is mixed into the CO_2 beam with the help of a specially designed beam combiner, which reflects all 10.6 μm radiation and yet is semitransparent to the He-Ne laser light. The location of the CO_2 beam then becomes visible and alignment is greatly simplified (the thermosensitive plates cannot be used on the expanded beam at all since its power density is too low).

The expansion of the beam is achieved by a pair of focusing mirrors: a small concave spherical mirror and a large 22.8 cm off-axis parabolic mirror. The two mirrors form a telescope that expands the beam diameter by a factor of 27. The off-axis parabolic mirror is the only way to produce a collimated beam of the required width that also would be free from significant aberrations or astigmatisms. It is custom manufactured by cutting a larger 56 cm on-axis parabolic mirror. A couple of Zinc-Selenide (ZnSe) lenses are used to prevent the CO_2 beam from expanding too early and to control the initial beam diameter when it enters the two-mirror telescope. ZnSe is the transparent material of choice for use with the 10.6 μm infrared radiation due to combination of its price and durability. It is also mostly transparent to visible light, allowing the use of the HeNe alignment laser.

Finally, a calibrated loudspeaker is located underneath the expanded beam right before it exits the table. The sound wave produced by the speaker is used to perform the system calibration and testing (as will be discussed later in section 2.4).

Figure 2-21: The PCI mirror stand underneath the C-Mod tokamak.

2.3.2 Mirror Stand

A large flat mirror is used to deflect the laser beam vertically into the Alcator C-Mod vacuum vessel. It is located right below the machine and inside the igloo. The harsh conditions in that area demand a special design for the stand that holds this mirror (Fig. 2-21).

The two worst factors that had to be dealt with when building the mirror stand were vibrations and temperature drifts. The Alcator C-Mod tokamak operates under typical magnetic fields of ~ 5 T. Just the generation of this field requires input of more than 200 MW into the magnets, and the resulting magnetic field pressure more than 100 times exceeds the atmospheric pressure. In addition to that, the plasma current is in the 0.4-1.2 MA range. The combination of this current and magnetic field creates tremendous forces inside the tokamak. Naturally, there are some deformations inside the machine, and this results in powerful vibrations. Although the mirror stand is not attached to the machine directly, it is positioned next to C-Mod support columns

and may be affected by the vibrations.

The C-Mod magnets require extensive cooling, and it is achieved by using liquid nitrogen (LN_2). During and after the machine pulse, large amounts of cold nitrogen are puffed from the tokamak cryostat in the vicinity of the mirror stand. This naturally cools the mirror and the stand, and cools it rather unevenly. The generated temperature gradients may result in non-uniform expansion of the components and change the mirror alignment.

The large sand-filled box represents the foundation for the mirror stand. Inside the box there are four carbon columns. The mirror mount is attached to the tops of these columns. There is a layer of rubber foam to somewhat isolate the box from the ground. The combination of the heavy box and the sand filling helps to further damp the vibrations.

To reduce distortions and misalignments due to temperature drifts significant attention was paid to selection of the right components when building the stand. The material of the columns (graphite-like carbon) has a naturally low thermal expansion. The mirror material is Zerodur glass, which is specifically mixed to have zero expansion coefficient. The mirror itself is quite large (30.5 cm) since it should exceed the laser beam diameter at least by a factor of $\sqrt{2}$ (due to the 45° reflection angle). If the mirror were made out of regular glass it would deform easily. Unfortunately, even with these precautions there is still some amount of drift left, and some alignment is still needed between shots.

2.3.3 Imaging Optics

The $1.07\,\mathrm{m} \times 1.68\,\mathrm{m}$ enclosure of top of the Alcator C-Mod igloo holds the PCI system imaging optics and the detector array. Figure 2-22 illustrates the enclosure content. The top cover (which is needed to prevent dust collection and for the safety reasons) is removed to make the photograph.

The layout of the optical components is shown in Fig. 2-23. First, a slightly raised large flat mirror deflects the CO_2 laser beam sideways (and somewhat downward) towards the large off-axis parabolic focusing mirror. Both mirrors are bolted directly

Figure 2-22: PCI imaging optics and detector array on top of the Alcator C-Mod igloo

to the concrete igloo top. The parabolic mirror is exactly the same kind as the one used to expand the laser beam on the lower PCI table (both are actually cut from the same original mirror). The focusing mirror reflects the beam exactly horizontally.

For the beam to be focused into a diffraction limited spot, surfaces of the all optical components in the system must be perfect to about $\lambda_o/20$ limit. Fortunately, most of the optics available commercially is manufactured to at least $\lambda/4$ limit for *visible* (usually HeNe laser) light, which translates to $\lambda_o/60$ when $\lambda_o = 10.6$ μm.

The rest of the optical components are mounted on a small optical table. There are two flat mirrors that steer the beam towards the phase plate as it is being focused. The sole purpose of these mirrors is just to make the PCI system more compact. The phase plate is mounted on a 3D translation stage (Fig. 2-13) and reflects the beam toward the ZnSe imaging lens. The power meter probe is located behind the phase plate to provide feedback on the plate position. There is also a scanning flat mirror between the imaging lens and the detector array. The angle of this mirror may be varied during the C-Mod shot, allowing imaging of different parts of the plasma on the detector.

The distances between the phase plate, the imaging lens and the detector array

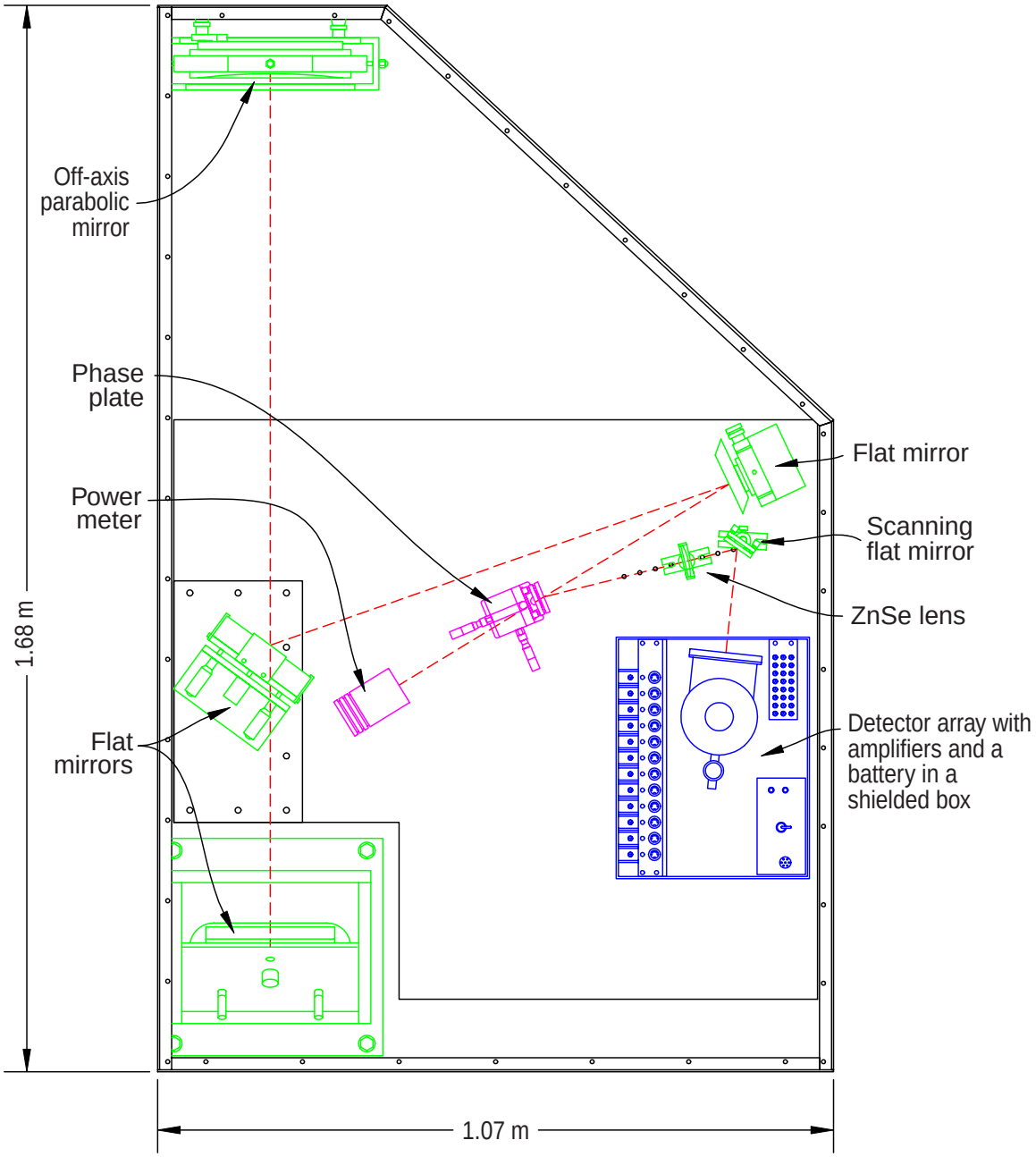

Figure 2-23: Layout of the optical components in the PCI enclosure on top of the C-Mod igloo.

Figure 2-24: Shielded box for the detector array, the preamplifiers and the battery power supply.

are made easily variable. There is a row of predrilled tapped holes to hold the lens to the table. All this allows different magnification coefficients to be achieved (in accordance with Eqs. 2.63 and 2.64).

2.3.4 Detector and Amplifier Box

The detector array and the set of preamplifiers are enclosed inside a shielded metal box (Fig. 2-24, shown with the top cover removed). The purpose of the box is to reduce pick up in the detector and in the detector-to-preamp cables. These components are especially susceptible since whatever is picked up there is then magnified by ~ 200 in the preamplifiers. The walls are made of 3/16" aluminum and should provide sufficient shielding. The box is grounded only via the ground terminal of the output cables. The other ends of the cables are attached to the digitizer ground. There is a

small rectangular window in the side of the box through which the laser light enters.

There is a built-in rechargeable Ni-Cad battery power supply. It has an optocoupler input to allow remote on/off switching. Using an optocoupler ensures that no pick being fed through the remote control cable. An external AC/DC power supply (ground insulated from the AC line by a transformer) proved to work almost as well.

The detector array is located inside a LN_2 cooled dewar. The dewar can hold LN_2 for only about 12 hours and needs to be refilled at the beginning of each run day. Periodic pumping down of the dewar is needed to ensure that the hold time does not decrease.

2.3.5 Remote Operation

The presence of high voltages and magnetic fields, low oxygen content (due to LN_2 cooling), neutron radiation and other hazards do not allow any personnel present in the Alcator C-Mod cell during shots. As a matter of fact, with a few exceptions, no access is allowed during the whole run day (8:30am to 5pm typically) at all. This requires that the system should be operated remotely from the control room.

An Allen-Bradley PLC-5 programmable logic controller is installed to facilitate the remote operations (Fig. 2-25), and is hooked up to a PC in the control room. The controllers consists of a number of replaceable modules. Besides the required CPU and the fiberoptic uplink modules, there are also digital IN, digital OUT, 12-bit analog IN and 12-bit analog out modules.

The realized functions on the PLC controller are the following:

- LASER: The high voltage power supplies for the laser tubes can be turned on/off and the discharge current can be adjusted. The shutter can be opened/closed. The water cooler can be switched on/off.

- GATEVALVES: The gatevalves are large 10" valves at the ends of the C-Mod vertical access tubes. These can be opened/closed and the pressure outside each gatevalves can be monitored.

Figure 2-25: The programmable logic controller used to remotely control the PCI system.

- PHASE PLATE: The phase plate can be moved side to side for the purpose of aligning the focal spot on the grove. An analog output from the power meter serves as a feedback for the plate position.

- DETECTOR: The preamplifiers and the bias current can be switched on/off to conserve the battery energy and to reduce the heat generation inside the dewar.

Using a special reprogrammable controller allows easy and fast changes to the system when needed.

2.3.6 Specifications

The table 2.3 summarizes the major specifications of the Alcator C-Mod PCI system. The responsivity and the sensitivity values given in the table are just some typical values. The real values are determined by the laser power and the amount of the laser noise for a given shot. These quantities tend to fluctuate within quite a large range depending on quality of the laser mode. Unfortunately, finding a good laser mode is not always an easy task for the laser used.

Laser type	CO_2 CW, DC-discharge pumped
Laser power	100 W
Laser wavelength	10.6 μm
Beam width	3-19 cm
Number of channels	12 (upgradeable to 32)
Accessible view, R	0.59 m$< R <$0.79 m
Accessible view, r	-10 cm$< r <$10 cm
Responsivity	$\sim 0.3 \times 10^{-13}$ V cm^2
Sensitivity (SNR=1)	$\sim 10^{11}$ cm^{-2} MHz$^{-1/2}$
Frequency range	2-500 kHz
Detectable λ_p range	0.5-19 cm
Detectable k_p range	0.33-12.5 cm^{-1}

Table 2.3: Specifications for the Alcator C-Mod PCI system.

Ranges of λ_p and k_p mentioned in the table refer to plasma fluctuations wavelength and wave number and are determined by the -3 dB cut-off.

2.4 Calibration and Testing Techniques

The most convenient way to test and calibrate the Phase Contrast Imaging system is by using sound waves in air [25]. The phase velocity of 340 m/s puts these waves well within the PCI measurement range. For example, the wavelength of a 15 kHz sound wave is 2.26 cm. This corresponds to about 4 detector channels per single sound wavelength or a total of about 3 wavelengths across the typical 7 cm laser beam width. The precise measurement of the wave number is easily achieved in this configuration. At the same time, 15 kHz is also within the 5–500 kHz operating frequency range of the PCI diagnostic.

The setup for testing and calibration includes a Radio Shack model 40-1377 loudspeaker with an 8 Ohm impedance and 4–40 kHz bandwidth. It is bolted to the surface of the PCI optical table (see Fig. 2-20). The expanded laser beam passes about 20 cm above the loudspeaker before entering the Alcator C-Mod vacuum vessel. The loudspeaker launches a spherical sound wave that propagates across the laser beam as shown in Fig. 2-26. High pressure and low pressure regions of the wave have

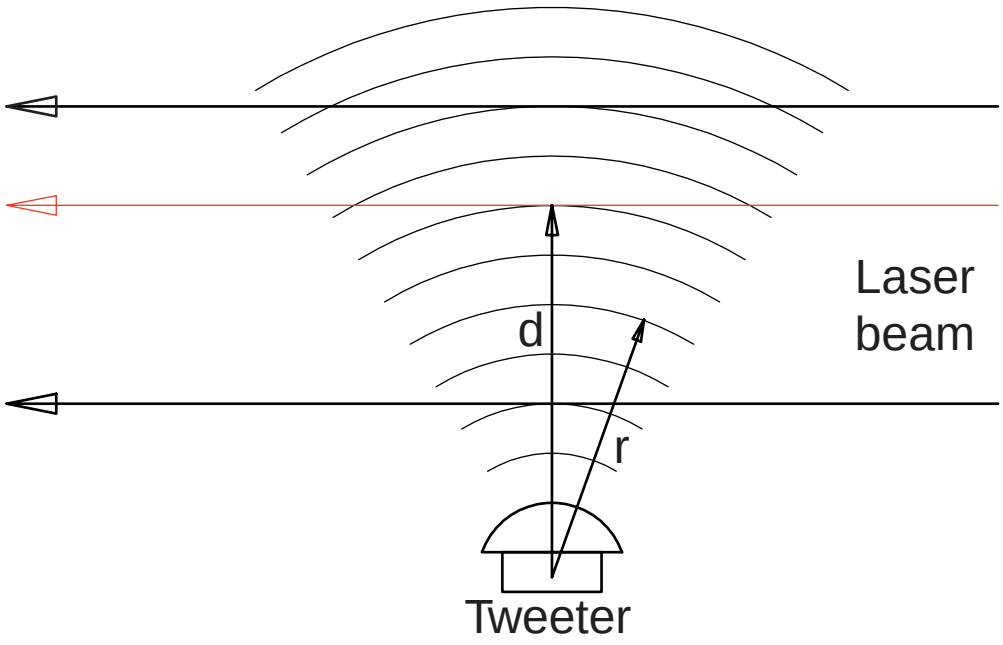

Figure 2-26: A spherical sound wave being launched by the tweeter.

different indices of refraction and alter the propagating laser beam wavefront in the same way the plasma density fluctuations would do. By knowing exactly how much alteration is done one can perform an absolute calibration of the PCI system.

An alternative source for the PCI calibration and testing is a standing sound wave in a ZnSe crystal. The wave is induced by a piezo-actuator glued to the edge of the crystal and driven at the crystal standing wave resonance frequency. One can get a $\lambda = 2$ cm standing wave pattern at about 200 kHz. However, the introduced phase variations in this setup are hard to estimate and absolute calibrations are not reliable.

2.4.1 Sound Wave Analysis

To be able to use sound waves in air for the absolute PCI calibration one has to know exactly how much phase delay is introduced into the laser beam. In this section, I will use the spherical wave approximation to achieve this.

The index of refraction of the air is governed by the Biot and Arago formula [41]

$$N - 1 = (N_0 - 1)\frac{\rho}{\rho_0} \ , \tag{2.68}$$

where $(N_0 - 1) = 2.72613 \times 10^{-4}$ and $\rho_0 = 1.2256$ kg/m^3 are reference values of the index of refraction and the density of standard air specified at $t = 15°C$, $p_0 = 1.01325 \times 10^5$ Pa and 10.6 μm wavelength [41, 42].

The sound speed is $c_s = 331.45$ m/s at 0°C. It is proportional to $\sqrt{T}$ and for a typical Alcator C-Mod cell temperature of 23°C becomes $c_s = 345$ m/s [41].

The pressure p and intensity I_S of a single frequency plane sound wave are connected by [41]

$$p = p_0 + \tilde{p} \ , \tag{2.69}$$

$$\tilde{p} = \tilde{p}_0 \cos(kx - \omega t + \phi) \ , \tag{2.70}$$

and

$$I_S = \frac{\tilde{p}_0^2}{2\rho_0 c_s} \ , \tag{2.71}$$

where $\tilde{p}_0$ is the amplitude of the pressure oscillations. The sound intensity I_S is often given in decibels with 10^{-12} W/m^2 being referred to as the 0 dB level.

For a spherical wave $I_S \propto 1/r^2$ and at $r \gg \lambda_s$

$$\tilde{p} = \frac{\tilde{p}_0 r_0}{r} \cos(2\pi \frac{r}{\lambda_s} - \omega t + \phi) \ . \tag{2.72}$$

The phase delay introduced by a sound wave into a laser beam is

$$\tilde{\Phi} = \frac{2\pi}{\lambda_{CO_2}} \int \left(\frac{1}{N} - \frac{1}{N_0} \right) dl \approx -\frac{2\pi}{\lambda_{CO_2}} \int \tilde{N} \ dl \ , \tag{2.73}$$

where we used $N = N_0 + \tilde{N}$ and $N_0 \approx 1$, and the integral is taken along the propagation path of the particular part of the beam.

From Eq. 2.68

$$\tilde{N} = (N_0 - 1)\frac{\tilde{\rho}}{\rho_0} = (N_0 - 1)\frac{\tilde{p}}{\gamma p_0} \ , \tag{2.74}$$

where $\gamma = 1.403$ is the ratio of the specific heats, c_p/c_v, for the normal conditions of air [41].

Now, by using Eq. 2.72 and 2.74 for the geometry shown on Fig. 2-26 one can

rewrite Eq. 2.73 in the following way

$$\begin{aligned}\tilde{\Phi} &= -\frac{2\pi(N_0-1)}{\lambda_{CO_2}\gamma p_0}\int \tilde{p}\; dl = \\ &= -\frac{2\pi(N_0-1)\tilde{p}_0 r_0}{\lambda_{CO_2}\gamma p_0}\int_{-\infty}^{+\infty}\frac{\cos(2\pi\lambda_s^{-1}\sqrt{x^2+d^2}-\omega t+\phi)}{\sqrt{x^2+d^2}}dx\ . \end{aligned} \qquad (2.75)$$

This integral can be calculated exactly [43] with the following result

$$\tilde{\Phi} = \frac{2\pi^2(N_0-1)\tilde{p}_0 r_0}{\lambda_{CO_2}\gamma p_0}\Big[J_0(2\pi d/\lambda_S)\sin(-\omega t+\phi)+Y_0(2\pi d/\lambda_S)\cos(-\omega t+\phi)\Big]\ , \quad (2.76)$$

where J_0 and Y_0 are the Bessel functions of the first and the second kind, respectively[4]. For $d \gg \lambda_S$ one can use the appropriate asymptotic limits of the Bessel functions. The equation 2.76 then reduces to

$$\tilde{\Phi} = -\frac{\pi(N_0-1)\tilde{p}_0 r_0\sqrt{\lambda_S}}{\lambda_{CO_2}\gamma p_0\sqrt{d}}\cos\left(\frac{2\pi}{\lambda_S}d-\omega t+\phi+\frac{\pi}{4}\right)\ . \qquad (2.77)$$

2.4.2 Actual Test Results

Most of the PCI sound wave tests are performed at 15 kHz using only a 1 ms long pulse. Such a short pulse is needed to avoid detecting reflected sound waves from the surrounding objects on the PCI bottom table. Spurious reflected signals arrive back into the detector view about 4 ms after the beginning of the pulse.

A typical voltage form applied to the speaker during the calibration pulse is shown in Fig. 2-27. It is generated by a small custom made electronic circuit. The initial part of that pulse (approximately the first 20%) has some lower frequency imperfections and normally is not used for the calibrations. The amplitude of the 15 kHz harmonic in the pulse is 25.2 V. This translates into 9.9 W of input power into the 8 Ohm speaker.

A test/calibration using a 1 ms sound pulse is routinely performed one second before each Alcator C-Mod shot. The results of the test are stored along with the

[4]Sometimes, the Bessel function of the second kind is also labeled as N_0.

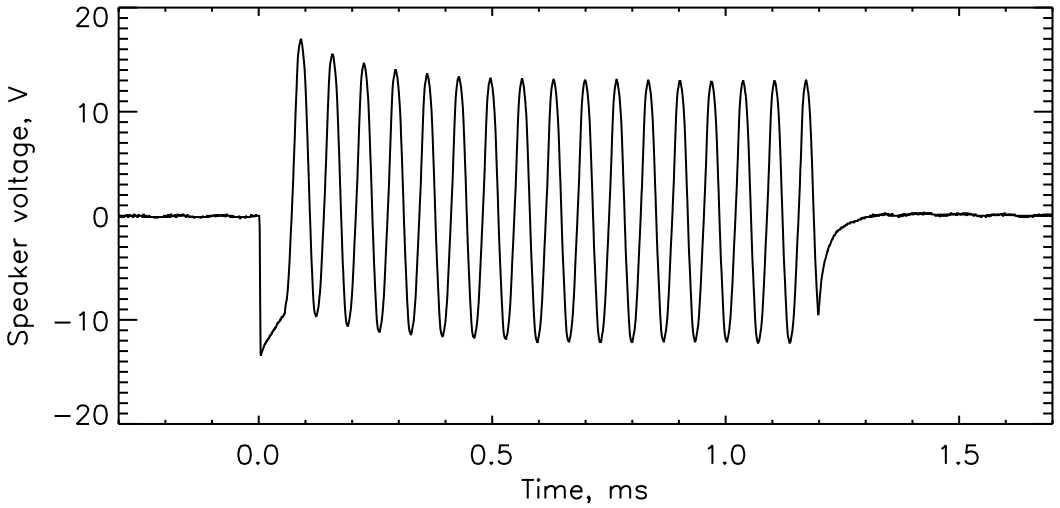

Figure 2-27: Speaker voltage during a calibration pulse.

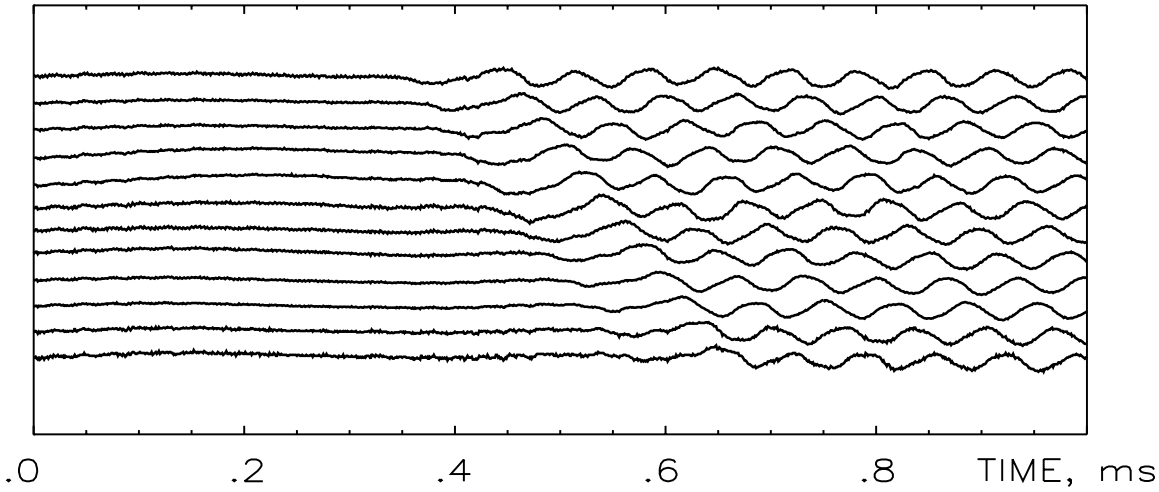

Figure 2-28: Raw signals from the 12 channels of the detector.

actual PCI data. The calibration results allow for compensation of the changes in laser beam intensity as well as for the difference in responsivity and amplifier gain of different PCI channels.

Figure 2-28 shows the response of the 12 PCI channels to a test pulse. At $t = 0.0$ s the sound pulse is launched. Each channel detects the pulse arrival at a different time. By looking at the different delay times and measuring the PCI channel separation directly one can verify that the pulse propagates across the channels with the appropriate sound speed of $c_s = 345$ m/s. Once that has been done, one is justified to reverse the procedure and use the arrival times to derive the PCI chord positions.

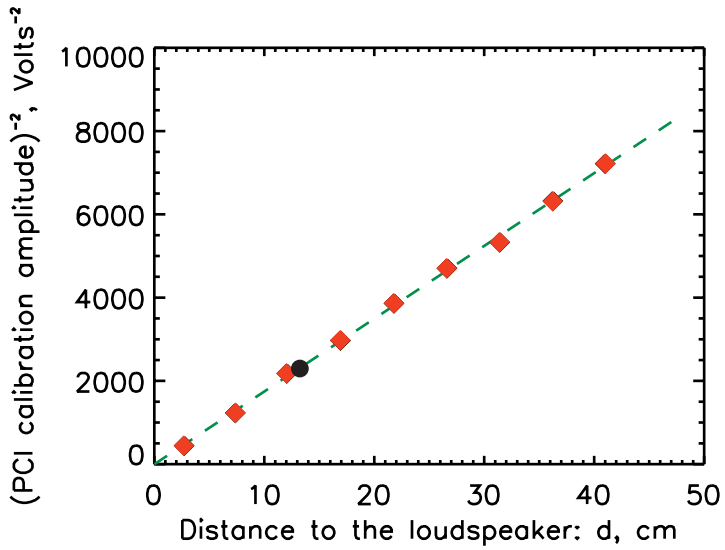

Figure 2-29: PCI calibration signal strength vs. distance to the loudspeaker.

The channel separation is obtained immediately by taking the difference of arrival times. In fact, the separation can be measured even more precisely this way than by direct measurement. Knowing the channel separation is crucial for deriving the wave number of fluctuations.

However, an absolute measurement of the PCI channel positions cannot be immediately derived from the arrival times. At least one direct measurement is needed to establish the position of a chord with arrival time $t = 0$ s. Once done, this measurement can be used as a reference (assuming that no more changes are introduced to the beam expansion optics) for all other measurements. Changes in the receiving optics will not affect this reference.

For better accuracy all 12 signals are used simultaneously. Equal spacing between all the channels is assumed and the best fit function of a 15 kHz traveling wave is found. The estimated accuracy is about 0.5 cm for the absolute position measurement, and 0.02 cm for the channel separation.

The following experiment was performed to verify the validity of the spherical acoustic wave approximation. The tweeter was suspended above the laser beam at various distances from the PCI integration chords. In each position 30 sound pulses were recorded and their signals averaged. According to Eq. 2.77 the amplitude of the

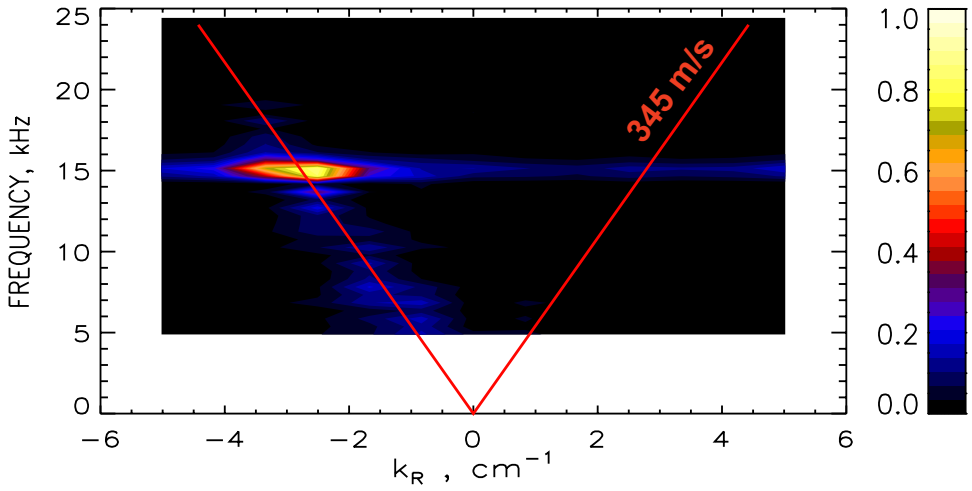

Figure 2-30: Sound wave in (f, k) space.

measured sound pulse amplitude should be inversely proportional to the square root of the distance between the tweeter and the integration cord.

In Fig. 2-29 the measured results are shown as diamonds with the dashed line being the best linear fit. As one can see the points do line up very well. The circle corresponds to the calibration signal amplitude for the loudspeaker at its usual position below the laser beam. The spherical wave model is in excellent agreement with the experimental data and can be used for the absolute calibration of the PCI system.

2.4.3 Two-Dimensional Fourier Analysis of the Sound Tests

12 PCI signals form a 2-dimensional array in (R, t) space, where R is the tokamak major radius coordinate of the PCI integration chord. By doing a two-dimensional Fourier transform the intensity of the PCI signal in (ω, k) space can be obtained. Each point in (ω, k) space would correspond to a particular harmonic of the PCI signal. This harmonic has spatial variations from channel to channel corresponding to a k value and oscillates with frequency $\omega/2\pi$ in time. Positive and negative k values correspond to waves propagating in opposite directions, with $k > 0$ specifying propagation in the increasing R direction.

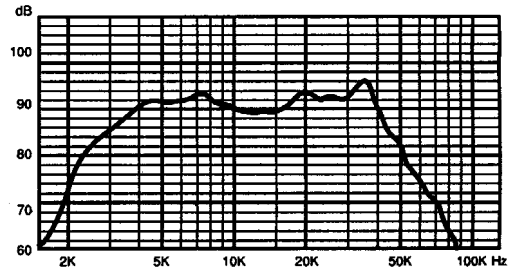

Figure 2-31: Speaker frequency response curve.

Figure 2-30 illustrates the results of the 2-D Fourier transform of a PCI signal containing the observed sound wave propagation (a 1 ms long slice of data beginning from $t = 0.4$ ms in Fig. 2-28). One can see a strong peak at $k = -3$ cm^{-1}, $f = 15$ kHz, corresponding to the sound wave. The propagation is only in one direction (negative), as it should be. The diagonal lines correspond to a phase velocity of ± 345 m/s. One of these lines passes through the peak, demonstrating that the measured phase velocity is correct. One can also see some weaker signals along the negative 345 m/s line. It can probably be attributed to the spectral impurity of the simple custom made signal generator used for the test. However, it still proves that the PCI system is working properly since these lower-frequency spurious signals still propagate in the right direction with the correct phase velocity.

2.4.4 Absolute Calibrations

An absolute calibration of the PCI system requires knowing the exact sound pressure produced by the loudspeaker. The best way to do that would be to use a calibrated microphone, which was not available. However, the manufacturer provided a frequency response curve for the loudspeaker (see Fig. 2-31). On this plot the vertical axis shows the sound intensity level in dB at 1 meter distance and at 1 watt input power. There are certainly some variations from speaker to speaker and the curve depicts only the typical response. This may not be the most accurate way to determine the sound pressure but it was the only one available. From sec. 2.4.2, the input power on the speaker is 9.9 W. The speaker "1 W, 1 m" response at 15 kHz

is about 89.5 dB. From these data and from Eq. 2.71 one can obtain the sound wave parameters

$$r_0 = 1\ m,\ I_S(r_0) = 8.82 \times 10^{-3}\ \mathrm{W/m^2},\ \tilde{p}_0 = 2.73\ \mathrm{Pa}\ . \tag{2.78}$$

After substituting these values into Eq. 2.77 one can find the calibration value of the phase fluctuation

$$\tilde{\Phi}_0 = 2.34 \times 10^{-3}\ \mathrm{rad\ cm^{1/2}}\ \times \frac{1}{\sqrt{d}}\ , \tag{2.79}$$

where d is the distance from the loudspeaker to the PCI integration chord. For a typical value of $d = 20$ cm one obtains the value of the phase fluctuation amplitude $\tilde{\Phi}_0 = 5 \times 10^{-4}$ rad.

Using Eq. 2.19 one can write down the plasma density fluctuation amplitude that would produce the same phase fluctuation as the calibration sound wave:

$$\left(\int \tilde{n}_0\ dz\right)_{\text{SAME AS SOUND}} = 7.83 \times 10^{12}\ \mathrm{cm^{-3/2}}\ \times \frac{1}{\sqrt{d}}\ . \tag{2.80}$$

Again, for a typical $d = 20\ cm$ this results in the sound wave producing the same PCI signal as a $1.75 \times 10^{16}\ m^{-2}$ line integrated plasma electron density fluctuation.

Chapter 3

Quasi-Coherent Fluctuations in the Enhanced D_α H-Modes

3.1 Introduction

In this Chapter, we study the Quasi-Coherent (QC) fluctuations that exists in the edge of tokamak plasma under certain conditions. These fluctuations are found to be responsible for a particularly good confinement regime (Enhanced D_α H-mode) of the Alcator C-Mod plasmas and currently are of great interest to the fusion community. Results of the experimental study of the QC mode by the PCI are compared with the resistive ballooning X-point mode predicted by the BOUT (Boundary Plasma Turbulence) numerical code[44].

3.1.1 Regimes of Operation of the Alcator C-Mod Tokamak

The achievement of sufficiently long particle and energy confinement times in magnetically confined plasmas is required for reaching breakeven and ignition conditions in a fusion reactor. On the other hand, confinement of the spent fuel (alpha particles) and impurities should not be high to prevent fuel dilution and radiative losses, respectively.

Two kinds of transport determine the confinement times in tokamaks. The first

results from the Coulomb collisions and referred to as *neoclassical* transport. Its exact mathematical calculation is somewhat complicated, partly because of the complicated orbits of charged particles in a torus, but can be done accurately[7]. The second type of transport, known as *anomalous* transport, is due to diffusion in fluctuating electric and magnetic fields which are generally observed in toroidal plasmas. Certain types of instabilities and turbulence can drive anomalous diffusion. Evaluation of the associated transport requires knowledge of the saturation levels of the instabilities, which can be obtained from complicated nonlinear analysis. Alternatively, numerical modeling may be used to predict the amount of transport.

Based on plasma transport and confinement conditions, a tokamak is said to operate in a particular regime, or *mode*. "L-mode" or the low-confinement mode is the oldest known and easiest to obtain in a tokamak. In this regime, the transport is dominated by anomalous diffusion and density and temperature just gradually fall off from the plasma core towards the edge. The L-mode is the typical operating regime possible in older tokamaks with circular cross-sections. For the Alcator C-Mod tokamak, the energy confinement time in L-mode is typically 20-30 ms.

A better confinement regime (correspondingly called H-mode for "high-confinement mode") was first discovered in 1984 in ASDEX tokamak [9]. This regime is characterized by suppression of turbulence in the vicinity of the separatrix (the last closed flux surface) and formation of a transport barrier. The safety factor q (defined as the number of toroidal revolutions a magnetic line completes while making one full poloidal turn) reaches infinity at the separatrix and, at the same time, a strong sheared radial electric field tends to suppress the instabilities. As a result, steep density and temperature pedestals form in the plasma edge, sometimes only 1-3 mm wide, and the confinement time increases factor of two or more as compared with the L-mode. Extremely high pressure gradients in the edge, however, may drive other kinds of instabilities, particularly ELMs (Edge Localized Modes)[45]. The ELM-free H-mode plasmas are free of these edge instabilities, but impurity accumulation due to the very long particle confinement results in increased radiation losses and eventually leads to a radiative plasma collapse[10], making this regime unapplicable for steady

state operation. ELMy H-modes, in particular with Type-I ELMs typical of high power neutral heated discharges, are periodically cleansed from impurities, and hence may be run continuously. However, during the occurrence of ELMs, a large fraction of the stored energy is ejected across the plasma edge over a very short duration of time, leading to undesirably large divertor heat loads.

In the high density, compact, diverted Alcator C-Mod tokamak yet another kind of H-mode is observed, the so-called enhanced D_α (EDA) H-mode [11]. Along with emitting much more radiation in the first D_α line of the deuterium Balmer spectral series, the plasma in this regime is characterized by significantly reduced impurity confinement compared to the ELM-free H-mode, while the energy confinement time is only marginally lower. The EDA H-mode is an excellent candidate for long pulse or steady state operation owing to the absence of excessive central radiation and large ELMs, and acceptable heat loads. Discharges in Alcator C-Mod were run continuously for at least 10 energy confinement times, limited only by the available RF heating pulse length (0.6 s).

Figure 3-1 shows transitions between a few different modes for one of the C-Mod shots. At $t = 0.94$ s the plasma switches from the initial L-mode to ELM-free H-mode due to externally controlled ramping of the toroidal magnetic field and the plasma current. The transition causes an immediate drop in the D_α emission level due to reduced excitation of neutrals in the cold plasma region outside the separatrix. These neutrals are typically excited by a flow of energetic particles from the plasma core and therefore the drop in D_α level indicates reduction of the transport across the separatrix. The transport reduction leads to better confinement and, as a result, the plasma density starts to climb. The PCI diagnostic detects increased signal in 100-400 kHz frequency range, caused by the increased plasma turbulence due to the higher core temperatures and density. At $t = 1.02$ s the second transition follows, this time to the EDA H-mode (as shown by increased level of D_α). Particle confinement somewhat worsens, and the density stops to increase. At the same time, the impurity level begins to drop, causing gradual decrease in the total radiated power level. Finally, at $t = 1.12$ s the plasma transitions again into the L-mode.

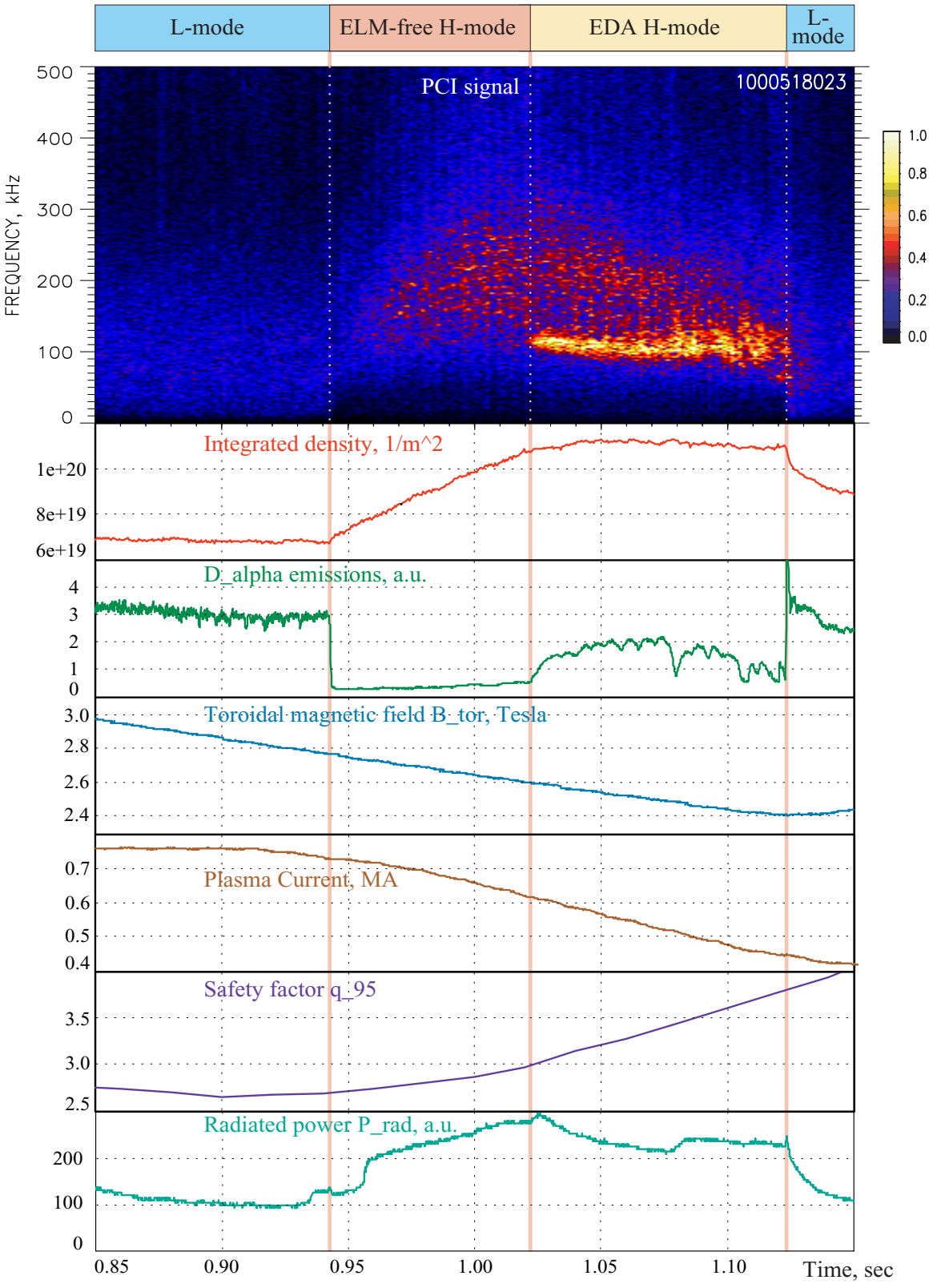

Figure 3-1: "L-" to "ELM-free H-" to "EDA H-" and back to "L-mode" transition in the Alcator C-Mod ohmic shot 1000518023.

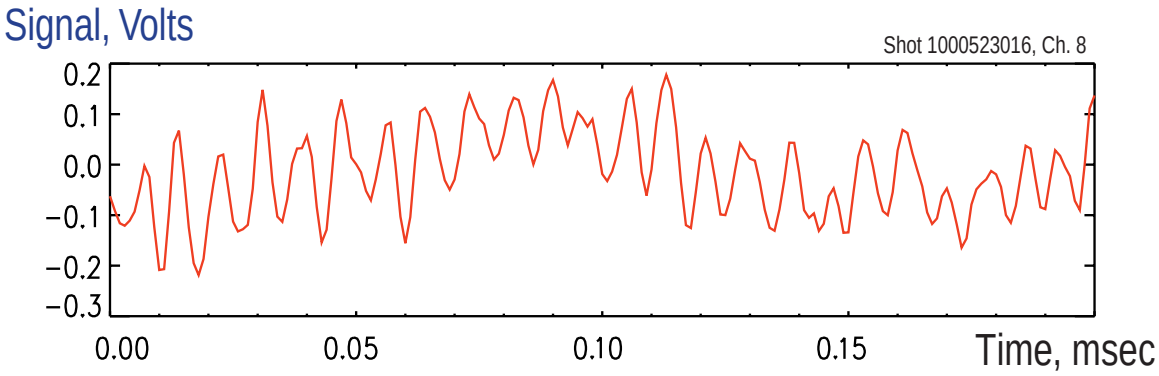

Figure 3-2: The voltage recorded from the PCI detector in EDA H-mode. The QC mode oscillation (∼130 kHz) clearly dominates the signal.

3.1.2 Quasi-Coherent (QC) Fluctuation Mode

An important property of the EDA H-mode is that it is always accompanied by a continuous, high frequency (50-250 kHz) Quasi-Coherent (QC) fluctuation mode localized in the steep density pedestal in the plasma edge region. This QC mode is easily seen in the PCI spectrum in Fig. 3-1 as a strong narrowband ($\Delta f \approx 20$ kHz) signal at ~ 110 kHz in the EDA H-mode. It may also be seen as a nearly sinusoidal fluctuation directly in the raw signal recorded from a single PCI detector channel (Fig. 3-2), or as a Gaussian shaped peak in a line plot PCI spectrum (Fig. 2-17(a) on page 64).

Besides the PCI, the quasicoherent mode has also been seen on other diagnostics on Alcator C-Mod, such as reflectometry[46], scanning Langmuir probes[2] and scanning magnetic probe[1]. All these diagnostics complement each other allowing many properties of the QC mode to be determined. While the PCI measures amplitude and wavenumber spectrum of the mode, the reflectometer and the scanning Langmuir probes provide information about the mode radial structure and location, and measurements of the fluctuating magnetic field are performed by the scanning magnetic probe. It should be noted that both probe measurements are performed only occasionally, limited to ohmicly heated plasmas only (RF heated plasmas are too hot and damage the instrument) and are not completely non-invasive. On the other hand, the QC mode is not always present in the reflectometry data (depending

on the density profile at the QC mode location), and this diagnostic results are somewhat hard to interpret[46]. This leaves the PCI as a primary tool for the QC mode study, capable of providing calibrated non-perturbing measurements in all kinds of plasma discharges.

Studies of ELM-free to EDA boundary found that the quasicoherent mode favors lower plasma current (higher q), moderate plasma shaping (triangularity $\kappa \sim 0.35 - 0.55$) and higher plasma densities[11]. It is an increase in the safety factor q and in plasma density that causes transition to EDA H-mode in Fig. 3-1. Overall, the QC mode was found to be localized within 1-3 mm wide area (full width at half maximum) in the plasma edge near the density pedestal foot. It propagates in the electron diamagnetic drift direction and has a poloidal wavenumber of typically 3–7 cm^{-1} and an amplitude of $\tilde{n}_e/n_e \approx$0.05-0.3 at the peak. The magnetic fluctuation component was estimated to reach $\tilde{B} \approx 5 \times 10^{-4}$ T by extrapolating the magnetic probe measurements about 1 cm away from the plasma separatrix[1].

The QC mode was estimated to drive a significant amount of particle flux Γ (up to $1.2 \times 10^{22}\ \mathrm{m}^{-2}\,\mathrm{s}^{-1}$) across the plasma pedestal, explaining lower particle confinement and increased level of D_α emissions in the EDA H-mode. The flux was calculated from $\langle \tilde{n}_e \cdot \tilde{E}_\theta \rangle$ as measured by the scanning Langmuir probe[2].

A very similar fluctuation mode was detected earlier by microwave scattering in the neutral beam heated PDX (Princeton Divertor Experiment) tokamak[47]. That mode and the QC mode found in Alcator C-Mod share many characteristics, such as narrow frequency spectrum, similar $\tilde{n}/n$ and $\tilde{B}/B$ amplitudes, and localization in the plasma edge region. However, in the PDX plasmas the fluctuations were always bursty in time, whereas in C-Mod the QC mode is typically continuous (although a bursty mode has been observed in some cases). Unfortunately, the absence of detailed measurements of the mode in PDX does not allow further comparison of the two modes.

Recent theoretical modeling suggests that the QC mode may be manifestation of the resistive X-point mode (a resistive ballooning mode which is strongly influenced by the magnetic geometry near the X-point)[48, 49]. A more detailed discussion of

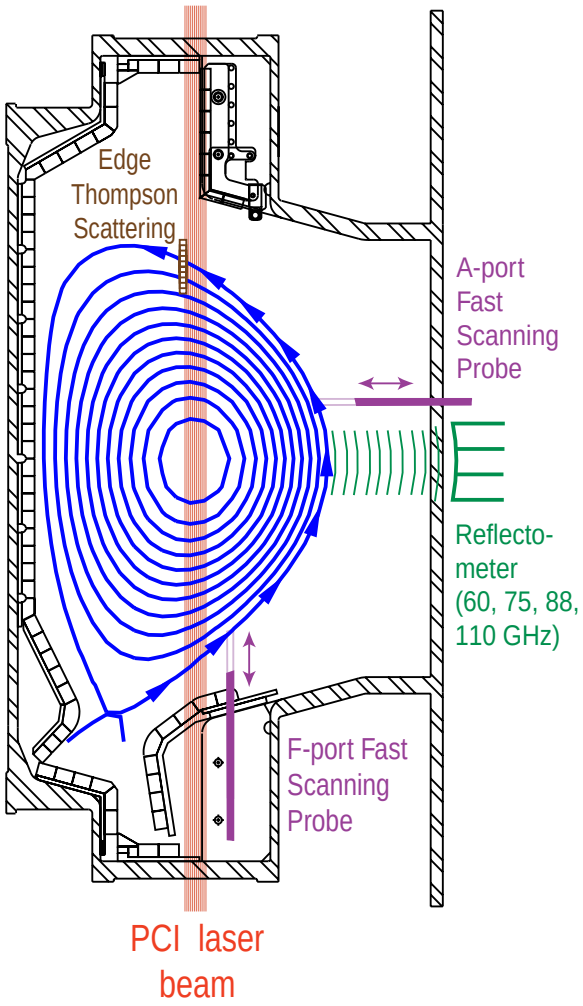

Figure 3-3: Positioning of the diagnostics used for QC mode study in the C-Mod vacuum vessel. Location and direction of propagation of the QC mode is indicated by the arrows in the plasma edge.

this mode theoretical model and results of numerical simulation are presented later in this chapter.

3.1.3 QC Mode Observation by the Phase Contrast Imaging Diagnostic

The Phase Contrast Imaging diagnostic is well positioned to study the quasi-coherent mode. The diagnostic CO_2 laser beam passes vertically through the plasma core and picks up the QC mode twice when it intersects the plasma edge (Fig. 3-3) near the

top and the bottom of the tokamak vacuum vessel. Although the mode propagates only in one direction (in the electron diamagnetic drift direction, i.e. counterclockwise in Fig. 3-3), it is observed propagating in two opposite directions in the PCI vertical laser beam, since the mode at the bottom part of the plasma is detected as moving from left to right (i.e. in the direction of increase of major radius R), and the mode at the top is seen as moving from right to left.

The wavelength of the quasi-coherent fluctuations is observed to be shorter in the laser beam due to the less-than-90° angle α between the plasma surface and a vertical. The measured wavenumber k_R relates to the mode poloidal wavenumber k_θ as

$$k_R = \begin{cases} k_\theta / \sin\alpha & \text{, at the bottom of a plasma} \\ -k_\theta / \sin\alpha & \text{, on the top of a plasma} \end{cases} . \tag{3.1}$$

Note that k_R is not the major radius component of the mode wave vector. The angle α is about 45° at the bottom and 55° on the top of a typical C-Mod plasma.

When comparing results of the diagnostics shown in Fig. 3-3 one should take into account that the QC mode parameters are likely to vary in different locations in a plasma. If the mode density fluctuations are field-aligned (a reasonable assumption considering a relatively small mode frequency of ∼100 kHz) then the mode radial width w and the poloidal wavelength should expand and compress with the magnetic field lines as the latter circles around the plasma. By definition[50, p.109], the magnetic flux ψ equation can be written as

$$\nabla\psi \times \hat{\mathbf{e}}_\phi = RB_\theta \hat{\mathbf{e}}_\theta \ , \tag{3.2}$$

where B is the magnetic field in plasma and R is the major radius. The mode radial width w then would change as a distance between adjacent two flux surfaces, and for a given instantaneous magnetic geometry the following relation would be valid

$$B_\theta R w = \text{const} \ . \tag{3.3}$$

If one now considers a flux tube in the plasma edge with the radial extent w and the poloidal extent $\lambda = 2\pi/k_\theta$, the amount of magnetic flux through a vertical cross section of this tube would be $w\lambda B_\phi$ and this quantity should stay constant as the tube circles around the plasma. Since $B_\phi = B_0 R_0/R \propto 1/R$, the following relation enqueues:

$$k_\theta R/w = \text{const} \ . \tag{3.4}$$

After substituting for w this can also be written as

$$B_\theta R^2 k_\theta = \text{const} \ . \tag{3.5}$$

In a typical C-Mod magnetic field configuration, the distance between the edge flux surfaces (and therefore the QC mode radial width) is about factor of 2.5 larger at the PCI beam locations than at the plasma outboard midplane (where the mode is detected by the reflectometer and the A-port scanning probe, see Fig. 3-3). Using Eq. 3.4, this predicts the QC mode wavenumber also to be larger by about factor of 2 at the PCI observation locations. Precise ratios should be obtained using Eqs. 3.3 and 3.5 individually for each shot using numerically reconstructed (by EFIT[51]) magnetic equilibrium.

Figure 3-4 compares the QC mode signal as recorded by the PCI and the reflectometry diagnostics[46]. A plasma with three separate H-modes (separated by brief periods of L-mode) is shown; the first H-mode is ELM-free (no D_α emissions and no QC mode), and the last two are EDA. In the second EDA H-mode the D_α level is stronger, suggesting a larger QC mode amplitude, and the PCI diagnostic indeed observes a stronger signal. No higher harmonics of the QC mode are observed by the PCI, indicating that the fluctuation is purely sinusoidal and that the diagnostic operates in a linear regime (the QC mode introduces a phase delay of the order of $< 10^{-2}$ rad to the laser beam; and significant non-linearity starts at $\Delta\Phi \sim 0.5$ rad). For the reflectometer, on the other hand, the probing radiation wavelength is about 3 mm (vs. 10.6 μm for the PCI) and the QC mode introduces phase delays of the order of π (since $\Delta\Phi \propto \lambda_{radiation}$ from Eq. 2.19). As a result, the reflectometer probing

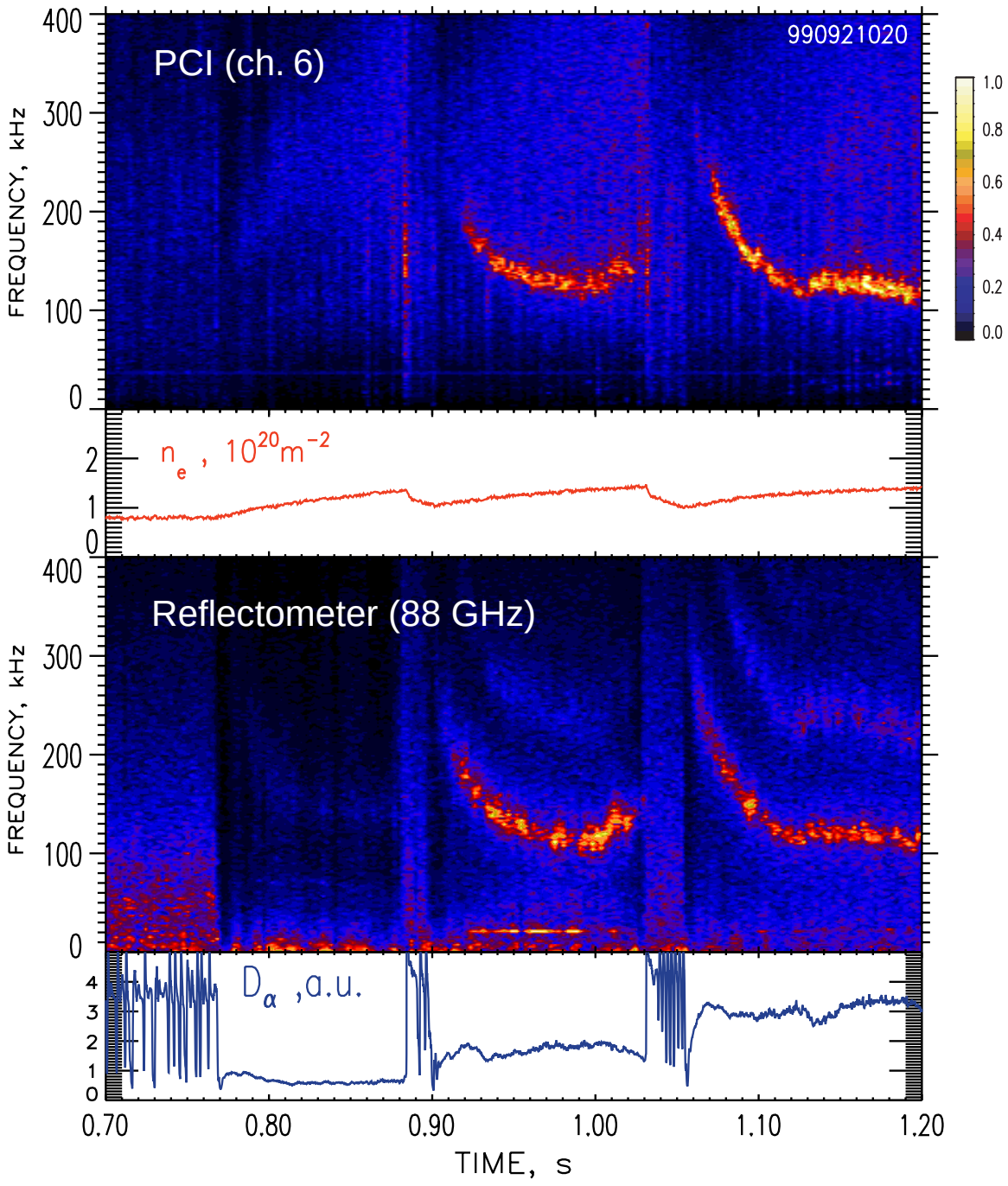

Figure 3-4: The same QC mode signal as detected by the PCI and the reflectometer diagnostics. Also shown are the line integrated plasma density and level of D_α emissions.

wave amplitude A is strongly affected by refraction and scattering on the QC mode, and that diagnostics response ($\propto A\cos\Delta\Phi$) becomes non-linear. This explains presence of the QC mode second harmonic in the reflectometer spectrum in the last EDA H-mode in Fig. 3-4, and may be partially responsible for no increase in the observed mode amplitude (along with a change in the reflectometer cut-off layer location due to a gradual density rise) compared to the PCI data. Although the reflectometer non-linearity and dependence on a density profile may be somewhat compensated by computer modeling[52, 46], the PCI diagnostic has the advantage of linearity and calibrated response when measuring the QC mode amplitude. On the other hand, the reflectometer dependence on the density profile allows it to determine a radial structure of the mode; something that the PCI alone is not capable of doing.

Figure 3-5 illustrates correlation between the measurements done with the PCI and the F-port scanning probe. The pneumatically driven probe was briefly inserted into the vacuum vessel, and at its most extended position the probe tip was only about 1 cm outside the plasma separatrix. Four separate Langmuir sensors are mounted on the probe head. When the probe was most extended these sensors recorded a coherent signal at the QC mode frequency of 110 kHz. By measuring a phase delay of the signal on the two sensors most separated poloidally, a wavenumber of the QC mode was estimated as $k_\theta \approx 4$ cm^{-1}. This value agrees well with the wavenumber inferred from the PCI data. One may notice a slight ($\sim$ 10 kHz) jump in the quasicoherent mode frequency in the PCI spectrum during the probe insertion. This may be an indication that the probe measurement is perturbing the plasma and that it alters the QC mode characteristics while trying to measure them. The PCI CO_2 laser radiation, on the other hand, does not interact with a plasma that much and the PCI diagnostic may be considered non-invasive.

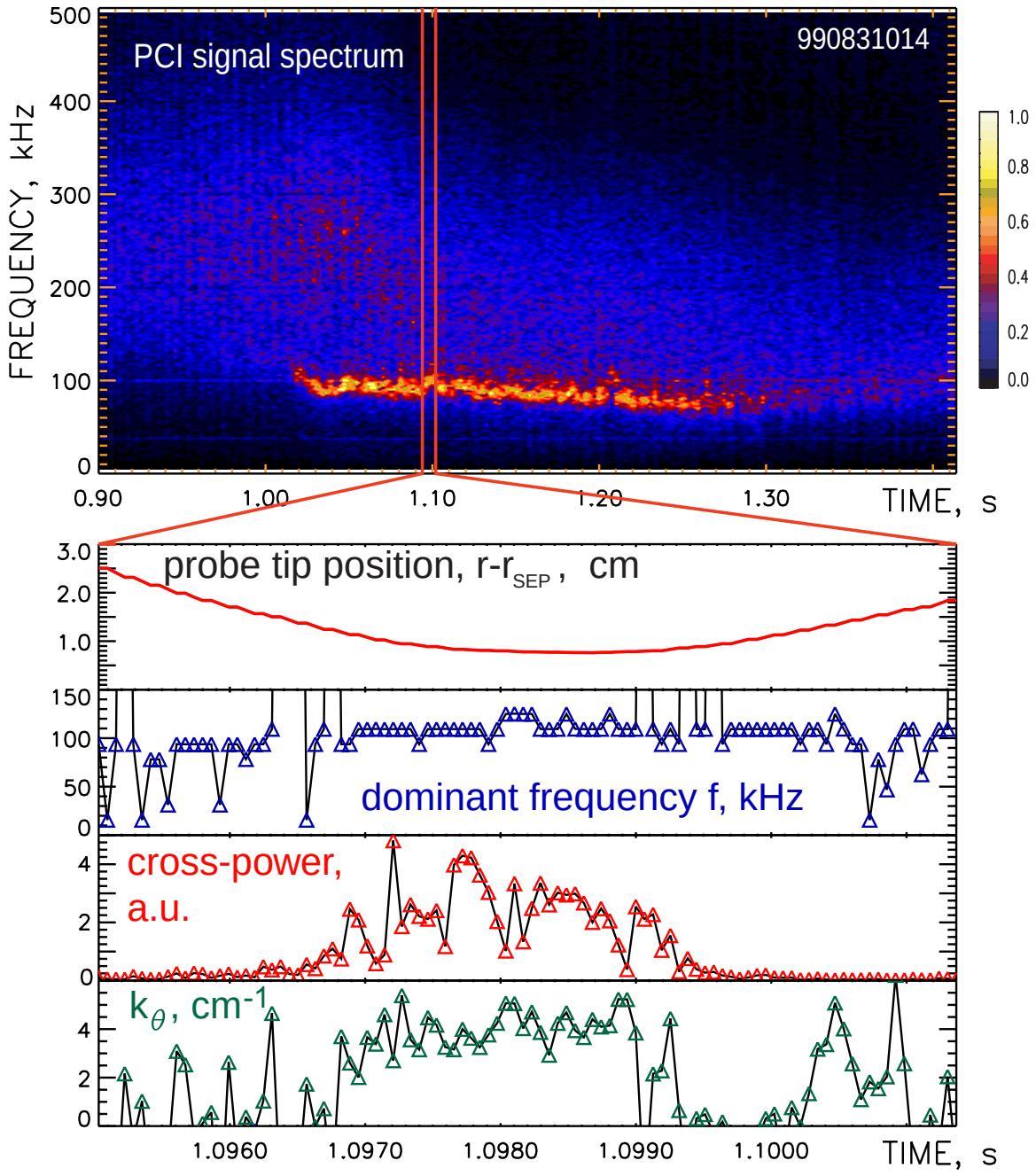

Figure 3-5: The quasi-coherent mode as being detected by the PCI and the F-port scanning probe.

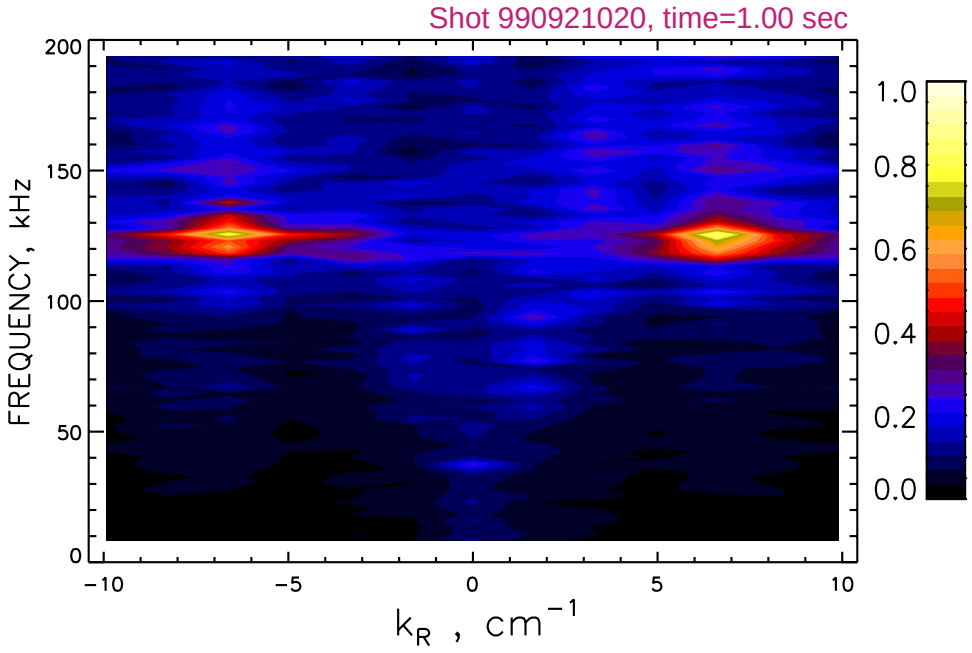

Figure 3-6: An instantaneous frequency/wavenumber spectrum of plasma fluctuations taken by the PCI diagnostic. Two peaks at 125 kHz correspond to the quasicoherent mode.

3.2 Experimental Study of the QC Fluctuations

3.2.1 QC Mode Wavenumber

Ability to continuously measure the quasicoherent mode wavenumber spectrum is one of the main advantages of the PCI diagnostic. An example of such measurement, an instantaneous frequency/wavenumber spectrum, is shown in Fig. 3-6. Two peaks in this plot are produced by the quasicoherent mode at the two locations where the diagnostic laser beam passes through the plasma edge. Most of the time the positive k_R peak would correspond to the bottom plasma location and the negative one to the top location (except those rare shots when the tokamak is operated in "the reversed field" configuration). Approximately equal magnitude of the peaks indicates roughly the same amplitude of the QC mode at the both places.

A limited number of the PCI channels limits the horizontal resolution in Fig. 3-6 to twelve data points. The wavenumber of the QC mode, however, may be estimated more precisely to taking a Gaussian-shaped fit to the wavenumber spectrum data.

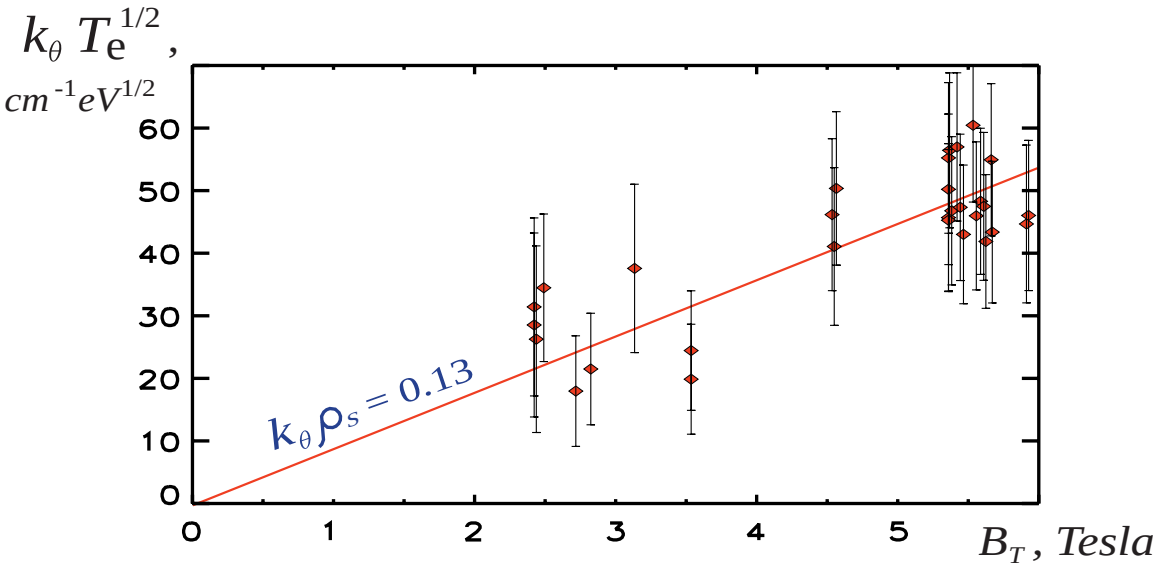

Figure 3-7: Scaling of the QC mode wavenumber with plasma electron temperature and magnetic field.

Equation 3.1 may further be used to convert the obtained k_R result into the mode poloidal wavenumber k_θ.

For different plasmas the QC mode wavenumber is found to increase with the toroidal magnetic field and weakly decrease with the plasma electron temperature. Overall, within experimental error it seems to obey the scaling

$$k_\theta \rho_S \approx 0.13 \tag{3.6}$$

for the bottom PCI location (Fig. 3-7). Here $\rho_S = c\sqrt{KT_e m_i}/eB_t$ is the ion Larmour radius estimated with electron temperature, B_t is the toroidal magnetic field and T_e is taken at the middle of the temperature pedestal as measured by the edge Thompson scattering diagnostic. Electron temperature is used since the ion temperature data are not available for the C-Mod tokamak (however, it is reasonable to assume $T_i \approx T_e$ in the edge due to high collisionality).

The QC mode wavenumber (as measured by the PCI) is also in agreement with the results inferred from the A-port scanning magnetic probe (Fig. 3-8)[1]. Since this measurement was taken near the plasma horizontal midplane, the $k_\theta = 1.5$ cm^{-1} wavenumber is significantly lower than the one typically measured by the PCI due to

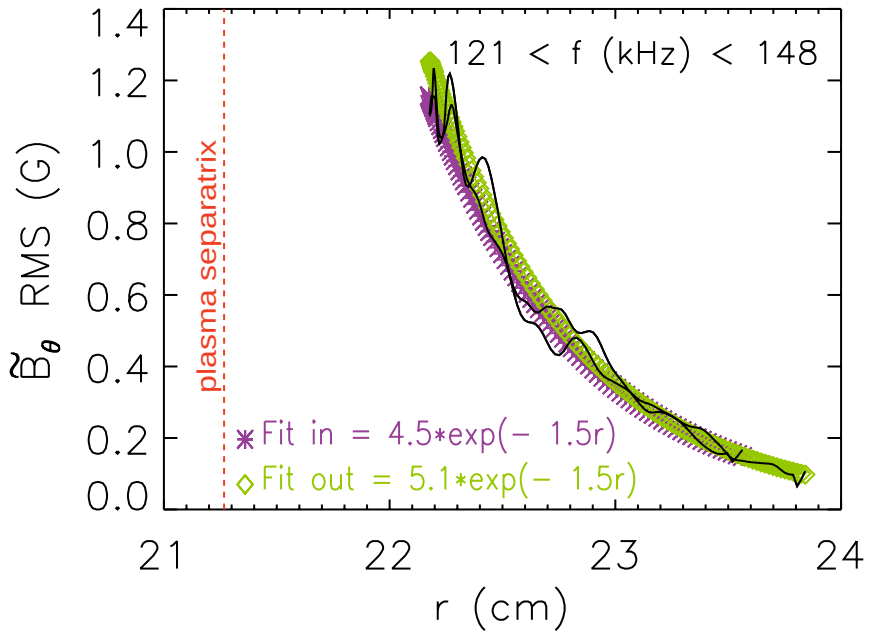

Figure 3-8: Fluctuating magnetic field due to the QC mode as measured by the scanning magnetic probe. The inferred mode wavenumber (equal to the fall-off rate) is 1.5 cm^{-1}. (from Ref. [1]).

expansion of the magnetic field lines. Equations 3.3-3.5 should be used to map this measurement to the PCI location and obtain the agreement.

3.2.2 QC Mode Frequency

The quasicoherent mode frequency ranges from 50 to 300 kHz, which nicely fits the PCI diagnostic frequency range of 2-500 kHz. A characteristic feature of this mode is that it typically starts at fairly high frequency of 200-300 kHz following an L- to H-mode transition and then the frequency "sweeps" down and settles at a steady state level of 50-150 kHz (as in Fig. 3-4, page 96). The characteristic time for this frequency sweep is about 20-30 ms.

We suggest the following explanation for the observed behavior. The measured QC mode frequency is determined by the two factors: the mode intrinsic frequency in the plasma frame and a Doppler shift due to overall plasma poloidal rotation. The intrinsic frequency should only depend on the plasma local parameters, such as edge pedestals and local magnetic field configuration. None of these were found to

change significantly during the frequency sweep. The mode wavenumber also stays relatively constant in the process, as seen in Fig. 3-9. In this example there is more than a factor of two drop in the frequency and only slight ($\sim$10%) fluctuation in the mode wavenumber. All this suggest that the mode intrinsic frequency is not likely to vary significantly during the transition, and therefore the poloidal rotation (and the corresponding Doppler shift) is left to be to be the only factor contributing to the observed frequency sweep.

The following two arguments may be used to further support this theory. First, the timescale of the sweep is consistent with the toroidal plasma acceleration timescale[53]. Toroidal and poloidal rotations are likely to be linked together, although the physics of these phenomena is currently not well understood. Second, the frequency sweep is not observed when the onset of the QC mode is preceded by a fairly long ($>$ 50 ms) ELM-free H-mode period, like in Figs. 3-1 (page 90) and 3-5 (page 98) the QC mode starts right up at the steady state frequency. In these examples the plasma rotation should be already settled when the ELM-free to EDA H-mode transitions occur. This implies the frequency sweep is caused not by the QC fluctuations themselves, but rather that these fluctuations are just a "tool" that makes the change in plasma rotation visible to us.

Since the observed QC mode frequency sweeps down following the L- to H-mode transition, bulk of the plasma should rotate in the ion diamagnetic drift direction (i.e. opposite to the QC mode propagation) in H-mode (if we assume there was no significant rotation in L-mode). The radial electric field needed to sustain such rotation through $E_r \times B$ drift is estimated to be at least a few tens of kV/m.

Mechanism determining the intrinsic QC mode frequency is still under investigation. One possible solution is offered by the resistive X-point mode theory[48] described later in this chapter. In this theory the QC mode is accompanied by a narrow, yet relatively deep E_r well localized in the pedestal region. The mode phase velocity is found to be close to $E_r \times B$ drift velocity in the well.

Figure 3-10 illustrates another property of the quasicoherent fluctuations – their

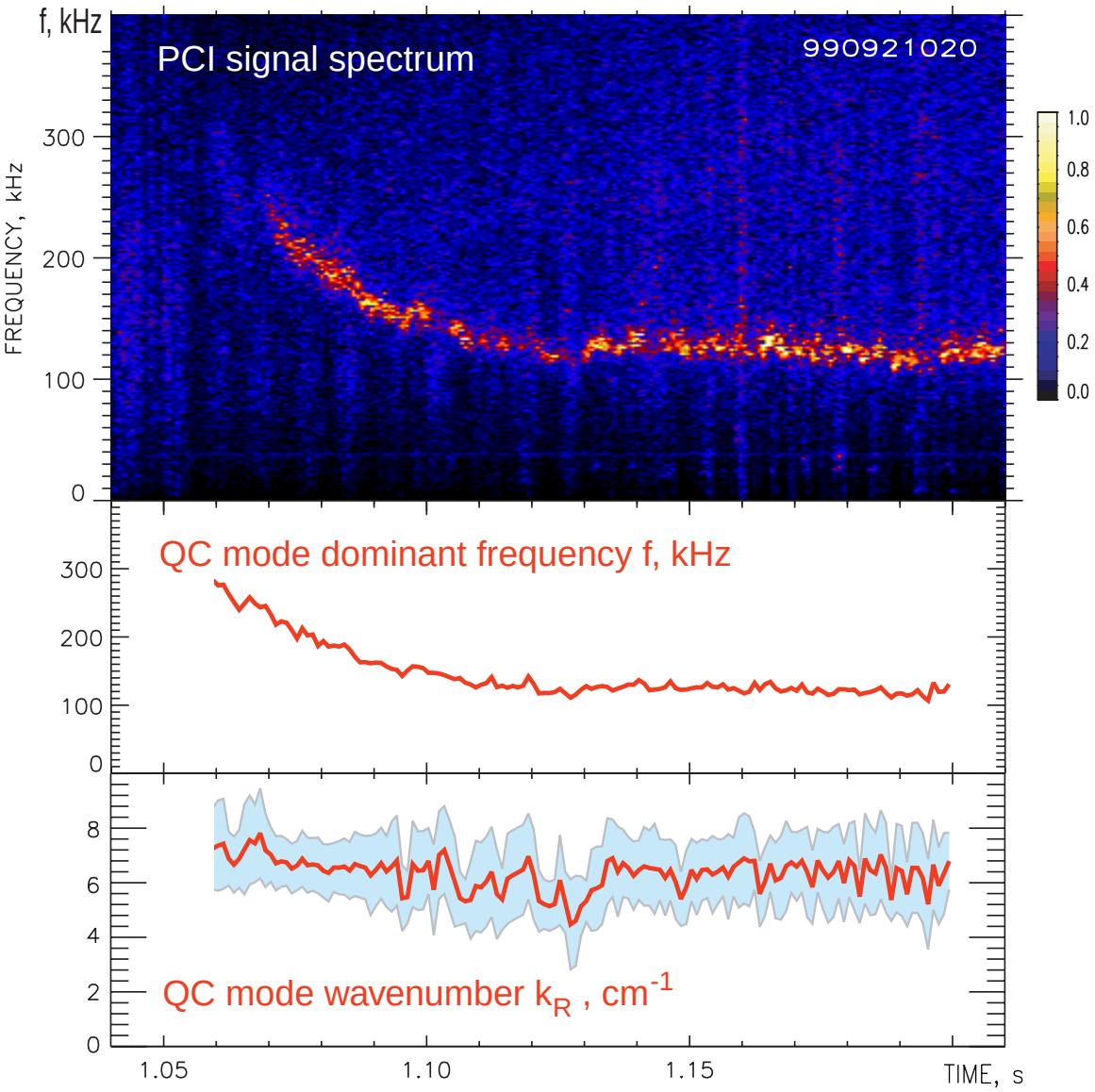

Figure 3-9: QC mode frequency sweep following an L- to H-mode transition. Frequency and wavenumber values are obtained by fitting a Gaussian function on the PCI data spectra. Shaded area on the k_R plot shows the width of the fit.

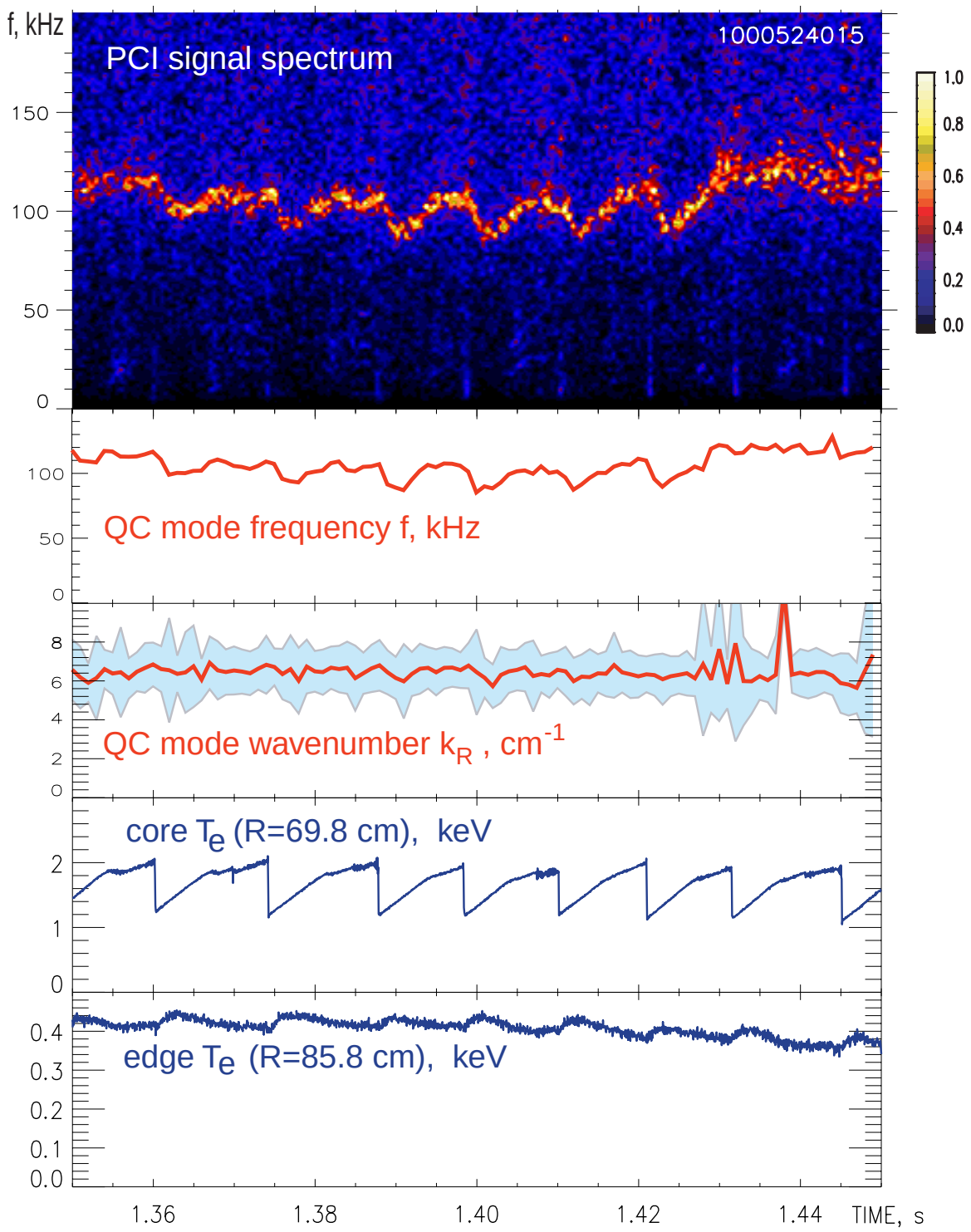

Figure 3-10: The quasicoherent mode frequency is modulated by the sawteeth in electron temperature.

frequency is modulated by the sawteeth oscillations in electron temperature[1]. Each sawtooth crash is followed by a decrease in the mode frequency. Since the mode is localized in the plasma edge, the frequency changes are most likely caused by the changes in edge plasma temperature – higher frequencies corresponding to lower edge temperatures.

The relative frequency changes are quite large – more than twice the relative changes in edge plasma temperature, while the wavenumber of the mode has a much weaker dependence. This may be explained by the fact that the observed frequency is significantly reduced by a Doppler shift. In the plasma frame the mode frequency may be factor of 2-3 higher than in the lab frame and the relative frequency changes would not be that large. The poloidal plasma rotation is unlikely to be affected much by the sawteeth oscillations since it has a significantly longer characteristic time.

3.2.3 QC Mode Amplitude

The line integrated amplitude of the QC fluctuations is easily measured by the PCI owing to this diagnostic linearity and absolute calibration. Although no simple dependency on major plasma parameters was found, the amplitude tends to increase with overall plasma density.

In the 1000914 series of shots most operational plasma parameters were kept constant and only the density was varied gradually[2]. At higher target densities the QC mode was found to be more intense (Fig. 3-11). As the mode amplitude increased, so did the level of D_α radiation at the plasma midplane. This again suggests that the quasicoherent fluctuations are responsible for driving a significant amount of particle transport out of the plasma.

An important observation is that the X-ray radiation pedestal gets wider with increasing QC mode amplitude. X-ray emissions are mostly generated by hot high-

[1]Sawteeth oscillations in electron temperature T_e are caused by an instability with toroidal and poloidal mode numbers of one. It occurs when the tokamak safety factor $q = rB_t/RB_\theta$ drops significantly below unity in the plasma core. During a sawtooth crash the magnetic field lines inside the plasma are "reconnected", a process that is accompanied by expulsion of hot core particles closer to the plasma edge. The temperature is then ramping up again due to external plasma heating.

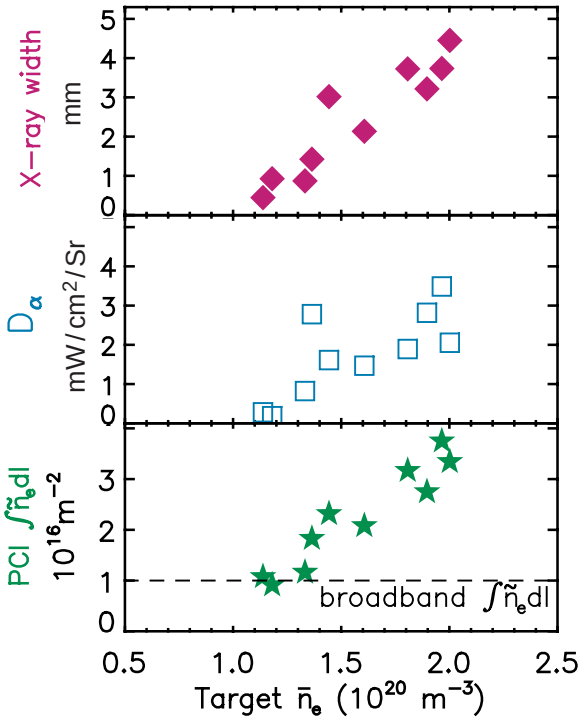

Figure 3-11: Correlation of the QC mode amplitude, D_α emission level and the X-ray pedestal width (from Ref. [2]).

Z (high atomic charge) impurities and are responsible for radiative collapse of the ELM-free H-mode plasmas. The X-ray pedestal width is a good indication of degree of the impurity confinement[54] (with narrower pedestals corresponding to longer confinement times). This directly shows how the QC fluctuations do reduce the impurity concentration of the EDA H-mode plasmas.

3.3 Numerical Modeling of the QC Fluctuation Mode

This section covers the results of collaborative work of the author of this thesis and his supervisor, Prof. Miklos Porkolab of MIT, with Dr. Xueqiao Xu and Dr. Bill Nevins of Lawrence Livermore National Laboratory[55]. As a result of this joint effort, a fluctuation mode with characteristics closely matching those of the C-Mod Quasi-Coherent mode was successfully modeled in a realistic tokamak geometry.

3.3.1 BOUT Code and Initial Conditions

The recently developed BOUT (**BOU**ndary Plasma **T**urbulence)[44, 56] numerical code is used to model events in the separatrix region of the Alcator C-Mod plasmas. The code is designed to simulate realistic divertor geometry and is based on a set of the Braginskii equations which predict the evolution of plasma vorticity, density n_i, electron and ion temperatures (T_e, T_i) and parallel momentum. A detailed list of the equations is given in Ref. [44].

The BOUT code is using the field-line-following coordinate system which has the advantage of efficiently representing high-n (high toroidal mode number) ballooning modes. Another coordinate is taken along the poloidal magnetic flux surfaces, with poloidal flux ψ normalized to unity on the separatrix. Typically the $0.95 < \psi_n < 1.05$ region is modeled in the code.

We start our simulations by using an EDA H-mode plasma profiles at a time slice $t = 1.00\ s$ corresponding to the C-Mod shot 1001020014 (Fig. 3-12). The magnetic geometry is obtained from the magnetic equilibrium code EFIT (for **E**quilibrium **FIT**ting)[51]. The EFIT is run to include the bootstrap current[2] contribution derived according to the Ref. [57]. The equilibrium plasma profiles used in BOUT and EFIT are obtained by using hyperbolic tangent fits to the experimentally determined (by the edge Thompson scattering diagnostic[58]) plasma density n_i and electron temperature T_e (Fig. 3-13). The mid-plane temperature and density on the separatrix are $T_e = 53$ eV, and $n_i = 0.67 \times 10^{20}$ m^{-3}, respectively, and on the top of the pedestal, $T_e = 330$ eV and $n_i = 1.91 \times 10^{20}$ m^{-3}. For these parameters ν^* is greater than 5 in the boundary region ($\psi_n > 0.95$) and the Braginskii two-fluid model is valid.

No experimental measurements of either the ion temperature or the radial electric field are available for this shot. Given the high collisionality it is reasonable to assume $T_i = T_e$, while the radial electric field is obtained from the nonlinear simulations themselves.

[2] *Bootstrap current* – the current generated in the pressure gradient region by trapped particles following the banana orbits

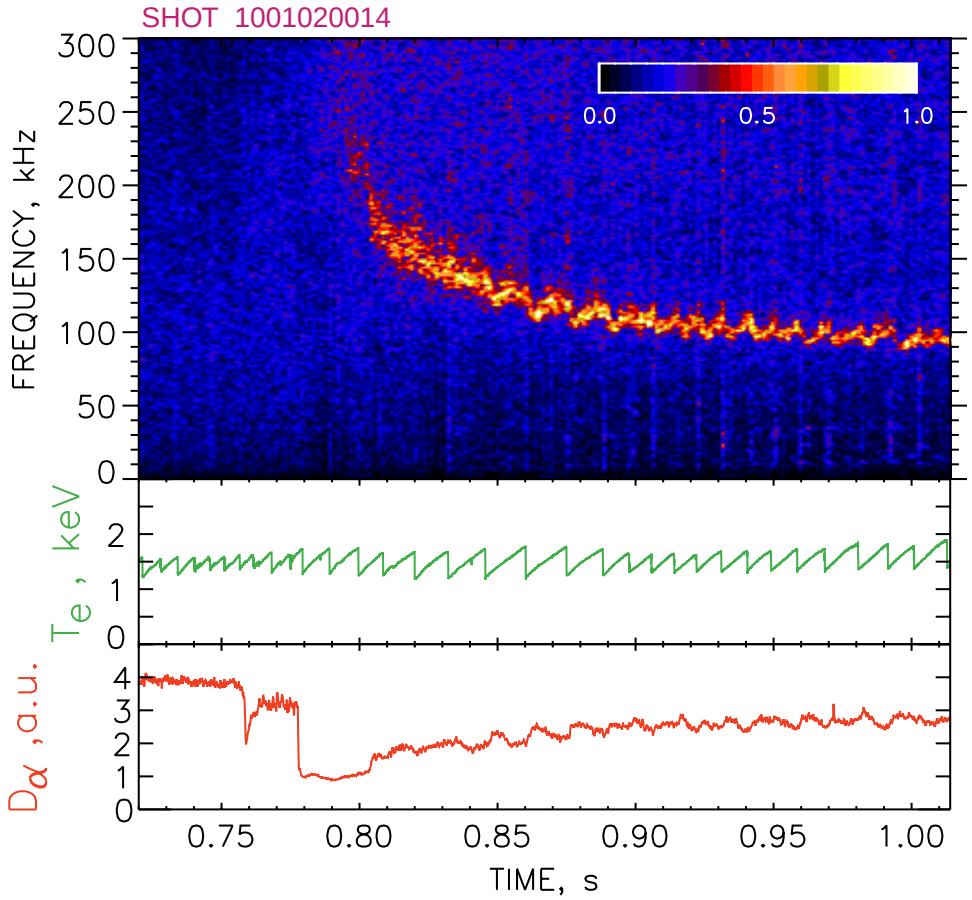

Figure 3-12: The $t = 1.00\ s$ of this C-Mod shot 1001020014 is used in the BOUT modeling.

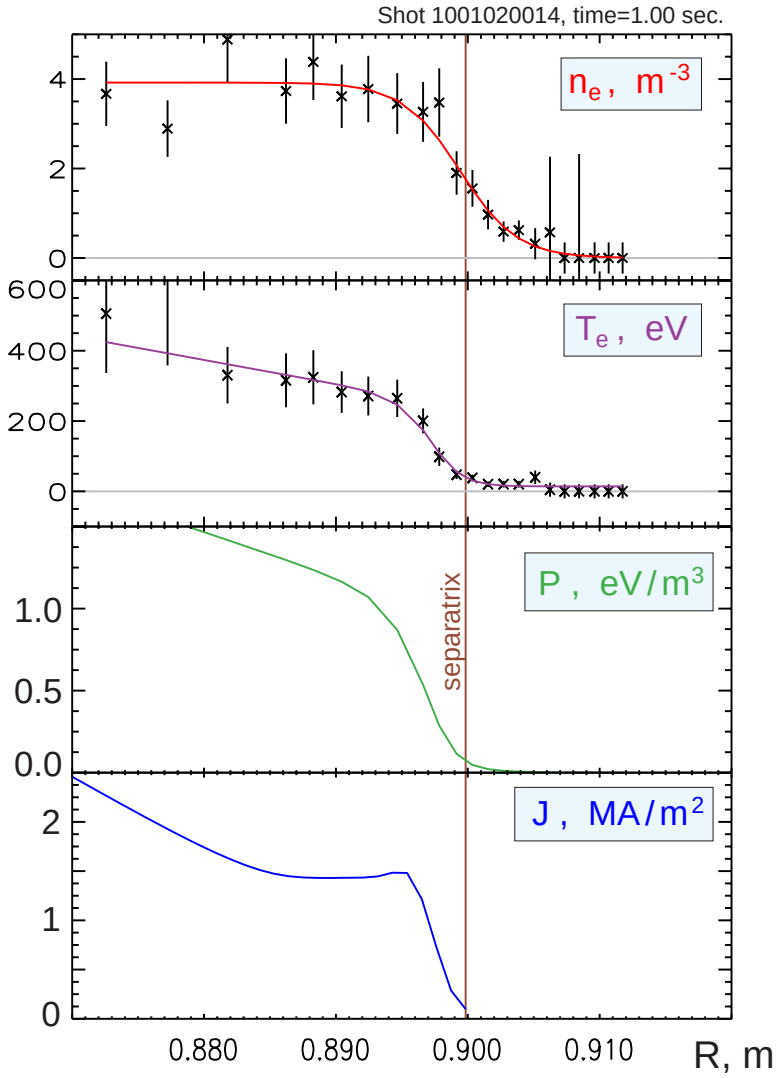

Figure 3-13: Shot 1001020014 (t=1.00 s) plasma edge profiles used in the BOUT modeling. n_e and T_e profiles are measured by the Thompson scattering and then *tanh*-fitted. The current density J profile is generated by EFIT and includes the bootsrap contribution.

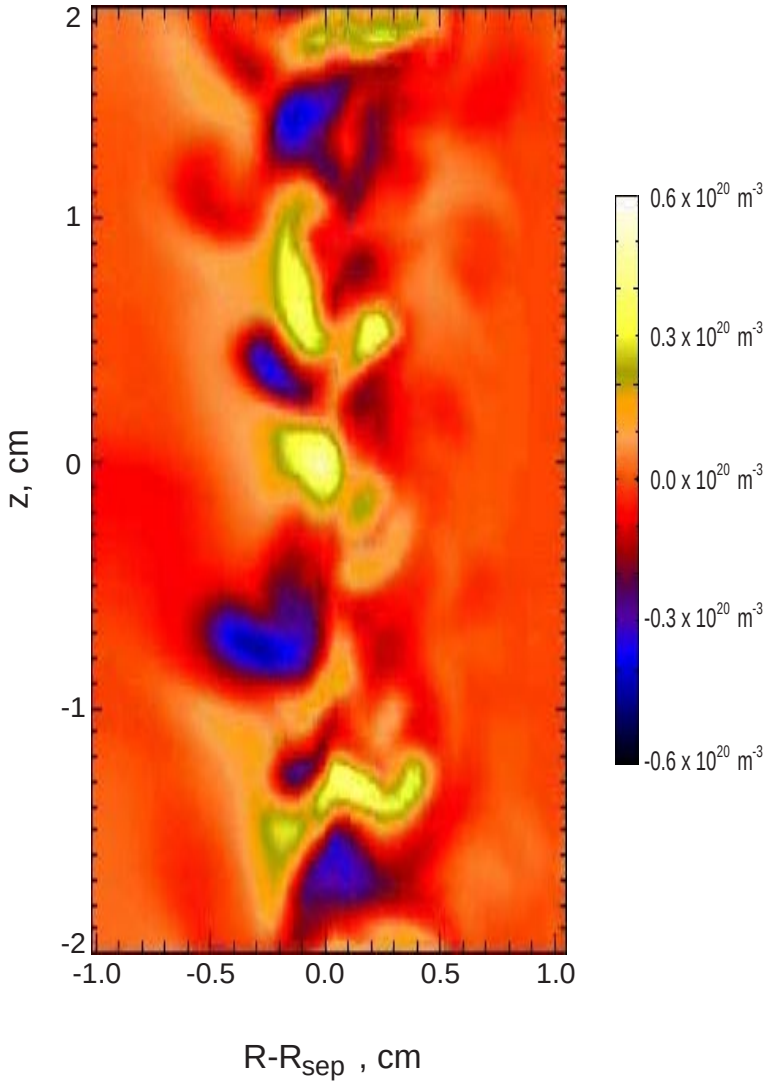

Figure 3-14: Plasma density fluctuations generated by the resistive X-point mode in the BOUT simulation.

3.3.2 Resistive X-point mode

The BOUT code is run from the initial conditions of the shot 1001020014 at $t = 1.00$ s. Within a simulation time of 80 μs the plasma turbulence settles down to steady-state which features a remarkably coherent resistive X-point mode[48, 49] at the plasma edge (Fig. 3-14).

Magnetic curvature is the dominant instability drive for the resistive X-point mode. This mode is electromagnetic at the outboard midplane and transitions to an electrostatic resistive mode near the X-point. This transition is due to electron

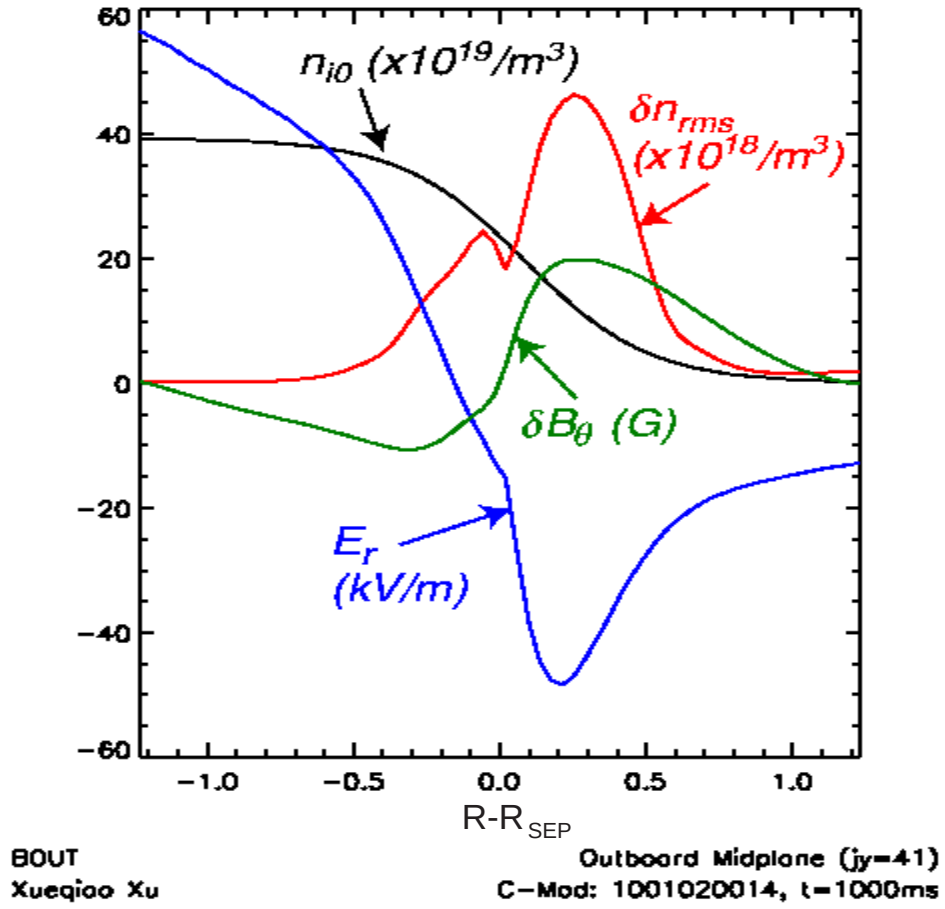

Figure 3-15: Amplitudes of density and magnetic field fluctuations and density and electric field profiles at the plasma midplane in the resistive X-point mode.

dissipation (collisional and collisionless skin effects) proportional to $k_\perp^2$ which becomes large near the X-point where magnetic shear yields large radial wavenumber, k_ψ and $B_p \to 0$ yields large k_θ.

Figure 3-15 illustrates the density and magnetic field fluctuation amplitudes inside the resistive X-mode. Also shown are the initial density profile and the evolved profile of the radial electric field. The density fluctuation amplitude (mapped to the PCI location) is in agreement with the line integrated PCI measurement of 2.1×10^{16} m^{-2}. The amplitude and fall-off rate of the magnetic field oscillations also agree well with the magnetic scanning probe data (Fig. 3-8 on page 101).

The frequency/wavenumber spectrum of the simulated resistive X-point mode is shown in Fig. 3-16. The plot shows an excellent agreement with the measured

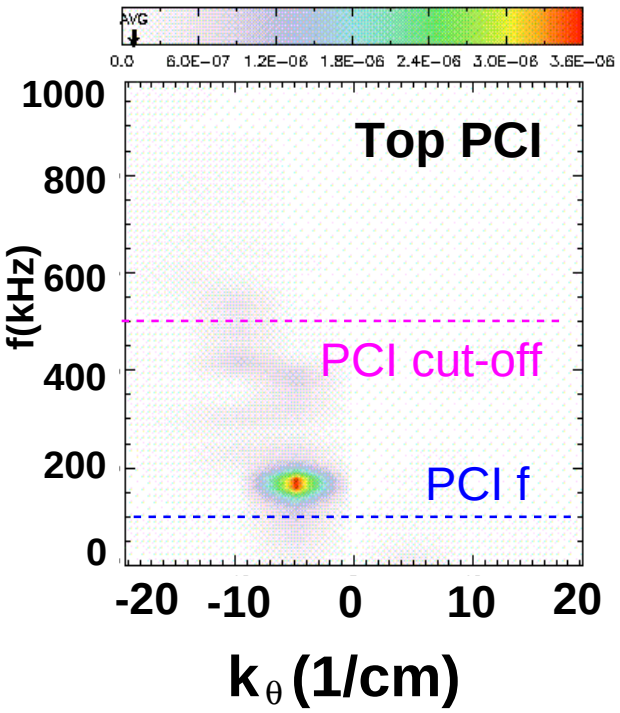

Figure 3-16: Frequency/wavenumber spectrum of the resistive X-point mode mapped to the top PCI location.

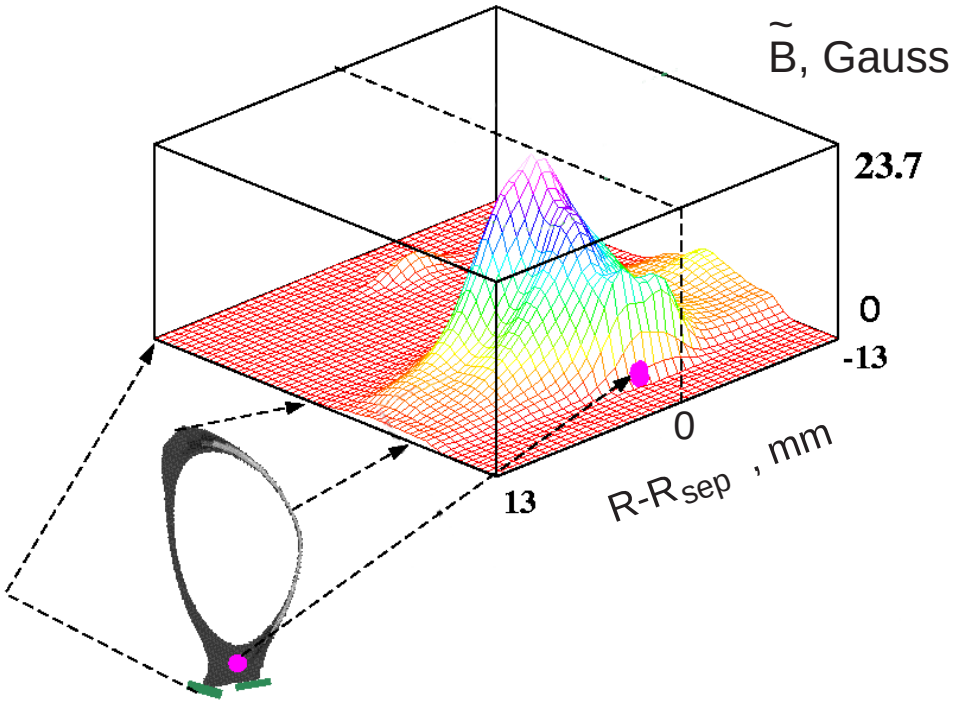

Figure 3-17: Fluctuating magnetic field amplitude in the resistive X-point mode.

quasicoherent mode wavenumber of $k_\theta = 4.5$ cm^{-1} for this shot. The mode frequency (175 kHz) also agrees reasonably with the experiment, but it is strongly influenced by the $E \times B$ drift induced by the radial electric field in a plasma. Since no measurements of the field are available, its profile is determined from the simulations themselves and the predicted frequency significantly depends on the assumptions used.

Figures 3-17, 3-18, 3-19 show distribution of the magnetic field and density fluctuations in the resistive X-point mode and the radial particle flux that it drives across the plasma separatrix. The latter is in agreement with the $\Gamma = 1.2 \times 10^{22}$ m^{-2}s^{-1} value measured by the scanning Langmuir probe near the plasma midplane[2].

3.4 Conclusions and Future Work

The beneficial confinement properties of the EDA H-mode regime have been linked to the quasi-coherent (QC) fluctuation mode that exists in the vicinity of the plasma separatrix. The mode has been compared to the resistive X-point mode predicted by the BOUT numerical code and the main features agree reasonably well. However, the fre-

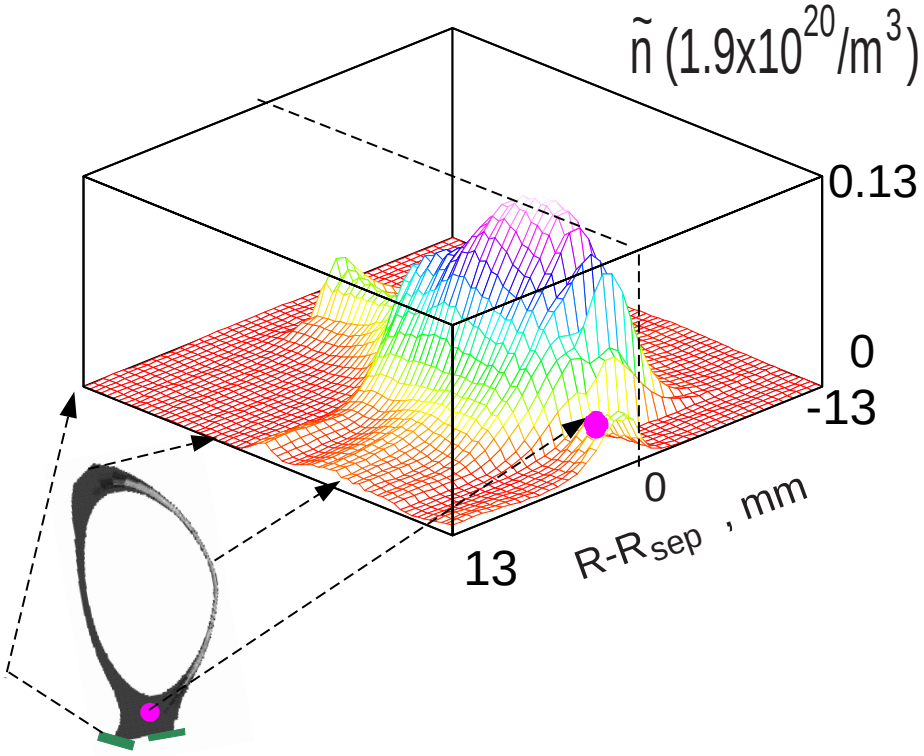

Figure 3-18: Density fluctuation amplitude in the resistive X-point mode.

quency is dominated by the $E_r \times B$ Doppler shift which is not measured in experiment in C-Mod. Earlier measurements indicated $-E_r$ values as high as 200 kV/m[59]. In some simulations by BOUT $E_r \approx -150$ kV/m has been seen. Given the uncertainties in the code modeling, the agreement with experiments considered to be reasonable.

Plans for future research include further experimental studies of the QC mode. The PCI diagnostic has been recently upgraded to a new CO_2 laser and now should provide reliable data for all C-Mod shots. A new scanning mirror was installed in the imaging optics and should make possible verifying the QC mode wavenumber dependence on the poloidal magnetic field (Eq. 3.5)by scanning the PCI laser beam position.

More numerical studies are desirable. One immediate goal is to study the resistive X-point mode dependence on the edge safety factor q_{95} parameter (this work is already in progress). Dependence of the mode frequency on the edge temperature may also be investigated (the QC mode frequency is very sensitive to the edge T_e changes caused

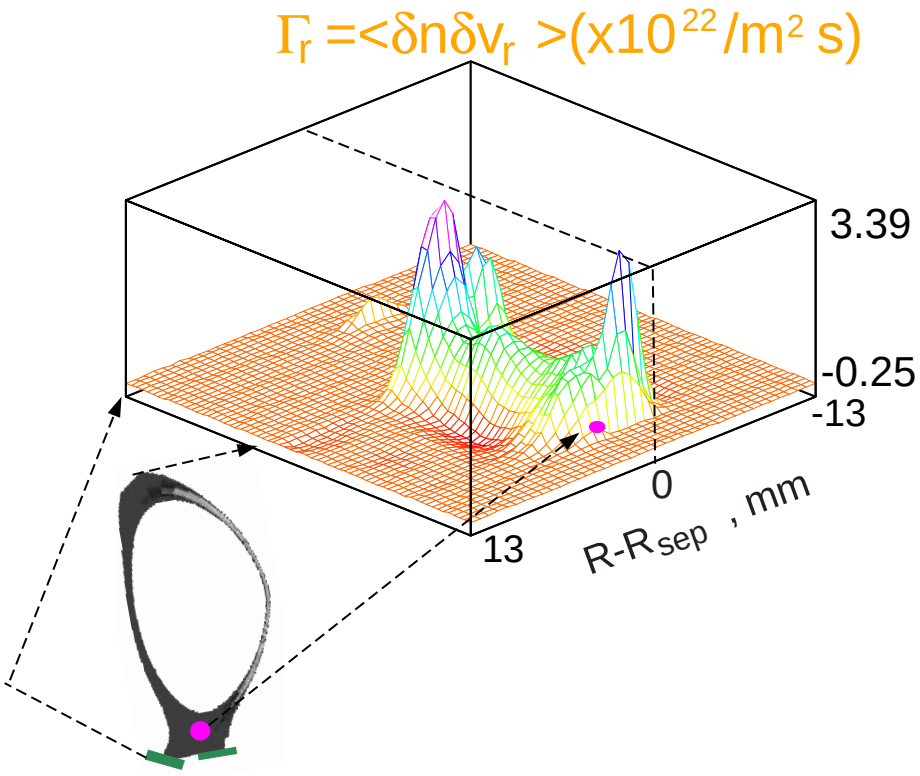

Figure 3-19: Radial particle flux driven by the resistive X-point mode.

by the sawtooth instability).

The BOUT code predicts that the mode fluctuation of the poloidal magnetic field should become zero and change sign near the separatrix (Fig. 3-15). We would also suggest to experimentally check this dependence.

Chapter 4

Optical Heterodyning Upgrade of the PCI System

Ion-cyclotron range of frequencies (ICRF) waves are the major source of auxiliary heating on the Alcator C-Mod tokamak. Detailed understanding of how these waves propagate and get absorbed inside the plasma is needed to improve heating efficiency and to drive plasma current.

One of the goals when building the PCI diagnostic was to directly observe the ICRF waves. The location of the diagnostic was selected in such a way that it would image the plasma in the vicinity of the RF antennas, and the laser beam was made wide enough to detect large (longer ~ 5 cm) wavelength density fluctuations induced by the waves. However, the high operating frequency of the antennas (80 MHz typically) does not allow direct digitizing of the PCI signals, and heterodyning of some sort was needed. Two alternatives are either to use conventional electronic heterodyning (when signals from the detector are electronically mixed with the reference frequency) or to use "optical heterodyning" – an alternative technique based on modulation of the laser beam intensity instead (first suggested by Stefano Coda [26]).

It was decided to upgrade the diagnostic using the optical heterodyning technique. The advantages of this technique over the conventional heterodyning are numerous:

1. No need for a new fast detector array. The detector should only be able to detect

signals at the beat frequency. It is especially beneficial since fast detector arrays are usually of photovoltaic kind and have large fluctuations of responsivity from channel to channel, not to mention higher price. The preamplifiers should not be fast either.

2. Only one set of electronics is needed, whereas in conventional heterodyning a set of electronics is needed for every channel.

3. The system should be much less prone to undesirable RF pickup from nearby multimegawatt antennas, since heterodyning is done optically. This pickup would probably be nearly impossible to eliminate in a conventional heterodyne system, especially since it is additionally magnified by the preamplifiers.

4. The PCI system retains the capability for direct measurement of low frequency plasma fluctuations. The same can be achieved with the conventional heterodyning, but would require an extra amplifier and digitizer for every channel.

All these advantages easily outweight the added requirement for the beam modulation. Basically, the beam modulation is the only modification needed to upgrade an existing low-frequency PCI system to optical heterodyning, although it is not an easy task. This chapter discusses the basic principles of optical heterodyning and its implementation on the Alcator C-Mod PCI diagnostic.

4.1 Optical Heterodyning Technique

As any heterodyning technique, optical heterodyning is applicable to the detection of some narrowband relatively high frequency signal, such as an ICRF wave in the tokamak plasma.

When such wave is present in the plasma and the laser beam is not modulated, the image intensity on a single detector element is expected to look something like Fig. 4-1(a1). In this example, the amplitude of the signal oscillations is varied with time to simulate the real wave behavior. The frequency of these oscillations is too

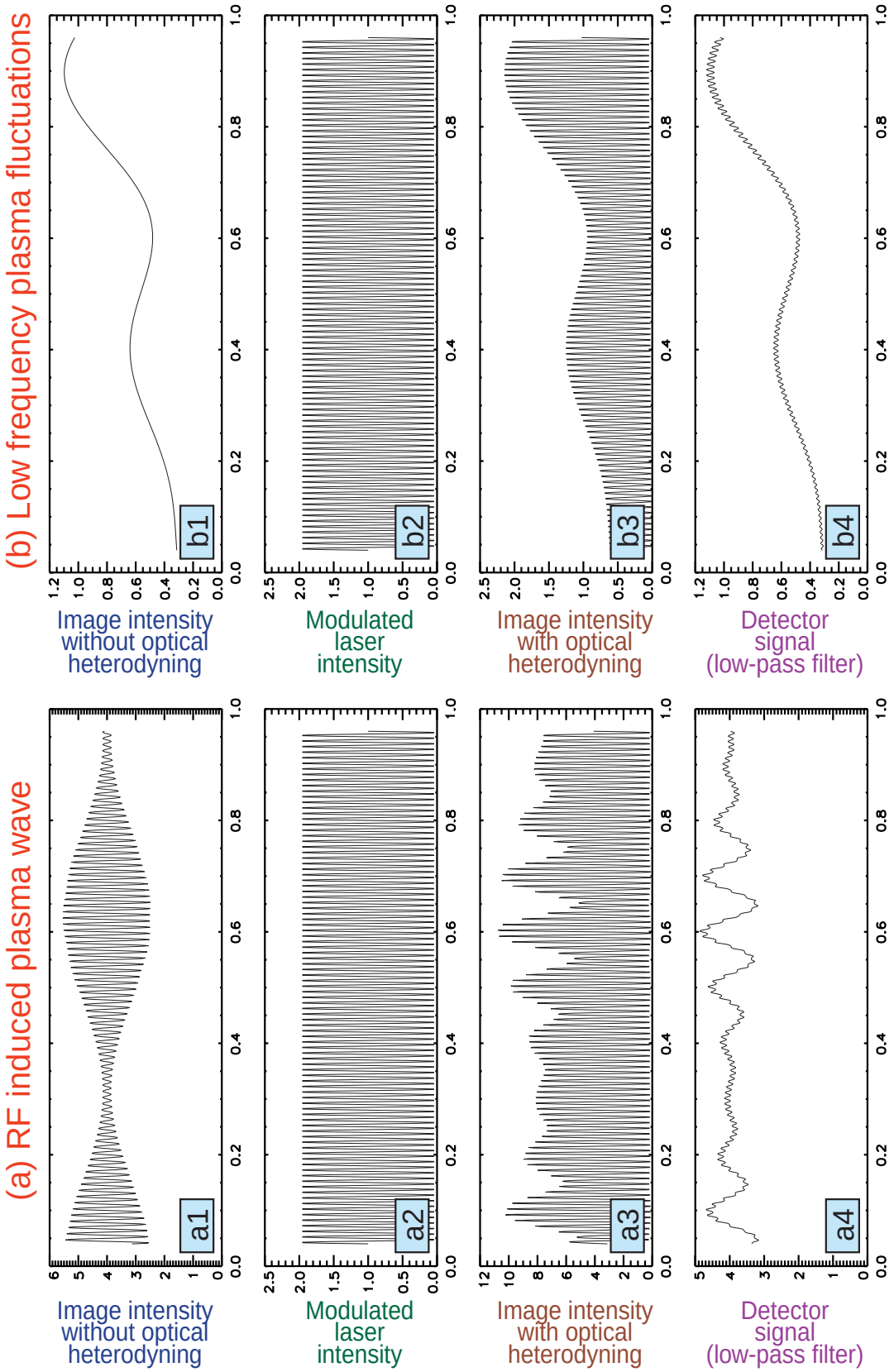

Figure 4-1: Examples of signal transformation by optical heterodyning.

fast to be detected and digitized directly. To make the detection possible, the optical heterodyning technique introduces amplitude modulation of the laser beam intensity at some close frequency. For example, in Fig. 4-1(a2) the laser modulation frequency is 10% higher than that of the RF wave. The image intensity on the detector in then just the product of these two signals (Figs. 4-1(a1) and (a2)) and looks like Fig. 4-1(a3). As one can see, there is still high frequency oscillation in the image, but now its envelope exhibits "beating" at a much lower frequency (about 10 times lower in this example).

The detector and the pre amplifier are too slow to resolve the high frequency component and average it out. Instead, they only observe the lower frequency beat oscillations. In Fig. 4-1(a4) the detector is modeled as an RC low-pass filter and the signal coming out of it is illustrated. Although some high frequency is still leaking through the this filter, it is negligible in the real system since the difference between the beat and the modulation frequencies is more pronounced. To summarize, the optical heterodyning technique converts the high frequency oscillations in the original wave into the beat frequency oscillations in the detector signal (with linear proportionality between the amplitudes of the two).

Figures 4-1(b1) to (b4) illustrate the effect of the optical heterodyning on a low frequency signal. Again, the detector is too slow to observe the laser intensity modulation and detects just the average waveform, which, in this case, is the same as the original signal. This way, the PCI system retains its capability to detect slow fluctuations in addition to heterodyne measurements.

Some simple modeling is needed for more accurate description of the optical heterodyning technique. Let us assume that for a given detector channel the varying part of the plasma phase delay (Eq. 2.19) is described as

$$2\tilde{\Phi} = A_1(t) + A_2(t)\cos(\omega_{rf}t) \ , \tag{4.1}$$

where $A_1(t)$ and $A_2(t)$ are two slow varying functions of time and ω_{rf} is the frequency of the RF antenna. The first term in this equation represents the low frequency broad-

band fluctuations and the second term is the oscillation caused by the propagating RF wave. From Eq. 2.32, the image intensity is

$$I_{image}^{PCI} = I_L(1 + 2\tilde{\Phi}) = I_L\Big[1 + A_1(t) + A_2(t)\cos(\omega_{rf}t)\Big] \ , \tag{4.2}$$

where I_L is the light intensity of the laser. In the optical heterodyning technique, the latter is modulated

$$I_L = I_0\Big[1 + \alpha_m \cos(\omega_m t)\Big] \ , \tag{4.3}$$

where ω_m and α_m are the modulation frequency and efficiency, $\omega_{rf} - \omega_m = \Delta\omega \ll \omega_{rf}$. After combining Eqs. 4.2 and 4.3 and performing some simple trigonometric conversions one can get

$$I_{image}^{PCI} = I_0\Big[1 + A_1 + A_2\cos\omega_{rf}t + (1 + A_1)\alpha_m \cos\omega_m t +$$

$$+\frac{1}{2}\alpha_m A_2\Big(\cos(\omega_{rf} - \omega_m)t + \cos(\omega_{rf} + \omega_m)t\Big)\Big] \ . \tag{4.4}$$

Since the frequency response of the detector is not sufficient to pick up the ω_{rf}, ω_m and $(\omega_{rf} + \omega_m)$ components, the terms with these frequencies are averages out of the detector signal S_d. What left is just

$$S_d \propto I_0\Big(1 + A_1(t) + \frac{1}{2}\alpha_m A_2(t)\cos\Delta\omega t\Big) \ . \tag{4.5}$$

The first two terms in this equation represent the response of the optically heterodyned PCI signal to low frequency plasma fluctuations. They are identical to the response of the non-heterodyned PCI diagnostic, assuming the average laser intensity is the same. The second term, however, is present only due to the laser modulation. It is proportional to the RF wave amplitude, while its frequency is downshifted to be within the detector-preamp range. One should also note that responsivity of the PCI system to high frequency fluctuations is only $\alpha_m/2$ of that for low frequency.

4.1.1 "Strobe Light" Analogy

There is a simple analogy that helps to understand the principles of optical heterodyning. The modulated laser beam may be thought of as a *strobe light* flashing with $\omega_m/2\pi$ frequency. When a strobe light illuminates an object such as a spinning wheel or a traveling wave, the motion of the object may be made to appear very slow. For this to happen, the frequencies of the movement and the strobe light should be very close. The eye of the observer in this case works just as the detector in the optically heterodyned PCI system — it is just not fast enough to distinguish separate flashes and notices the "averaged" slow motion at the beat frequency instead.

The spatial characteristics of the object (wavelength, for example) still appear to be the same regardless of the illumination. Thus, the wave number of the RF wave can be measured directly by PCI. However, the observed direction of the wave phase velocity may change: if $\omega_m > \omega_{rf}$ the wave will appear as moving backwards. Also, a strobe light does not change the visual appearance of slowly moving objects — these would look the same as when illuminated by a continuous light source. This explains how the optically heterodyned PCI diagnostic retains the capability for low frequency measurements.

The strobe light analogy is not perfect — for example, it cannot explain the appearance of 1/2 factor in the PCI responsivity for the heterodyned signal. This is because this analogy represents the laser intensity as a set of equally spaced delta functions, while in reality the modulation is sinusoidal.

4.2 Laser Beam Intensity Modulation

The frequency of the C-Mod ICRF antennas is typically 80 MHz. To observe waves propagating from these antennas, the PCI laser is modulated close to this frequency. This is achieved by using two acousto-optical frequency shifters. A sketch of one of such devices is shown in Fig. 4-2. It consists of 5×8 cm germanium crystal (germanium is transparent to 10.6 μm radiation). A piezo actuator is glued to one side of the crystal. It launches $\sim$40 MHz ultrasonic waves that propagate at 5500 m/sec

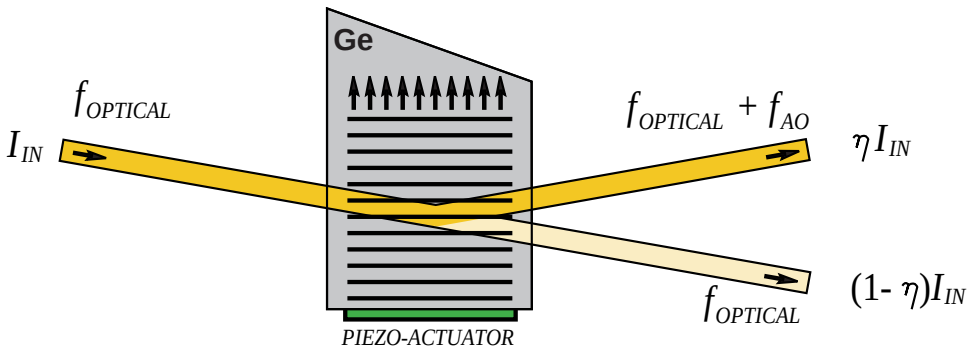

Figure 4-2: Acousto-Optical Frequency Shifter.

($\lambda_{Ge} \approx 138$ μm). The opposite side of the crystal is slanted to eliminate a reflected wave.

The laser beam scatters from the traveling ultrasonic wave. The scattering angle (difference between the directions of the input and scattered beams) is just the ratio of the optical and acoustic wavelengths, about 0.077 rad or 4.4°. Since the scattering is caused by a traveling acoustic wave, the optical frequency of the scattered beam changes due to the doppler effect:

$$f_{optical}^{scattered} = f_{optical}^{input} \pm f_{ao} \ . \tag{4.6}$$

The value of the plus/minus sign depends on the direction of the acoustic wave travel. If it propagates towards the input laser beam (like in Fig. 4-2) the sign is a plus, if away — then it is a minus.

Because of the large volume where the optical and acoustic waves intermesh, their interaction is essentially *Bragg scattering*. Waves scattered from different places in the crystal interfere with each other. The result is that the efficient scattering is possible only under certain orientation (angles of incidence and "reflection" must be equal), but the amount of power going into the scattered beam may be close to 100%.

The acousto-optical frequency shifters normally do not modulate the laser beam intensity, but rather shift its optical frequency. To produce modulation, two shifters should be arranged as shown in Fig. 4-3. The original laser beam is split into two parts which get up- and down-shifted in frequency. The two beams are then recombined

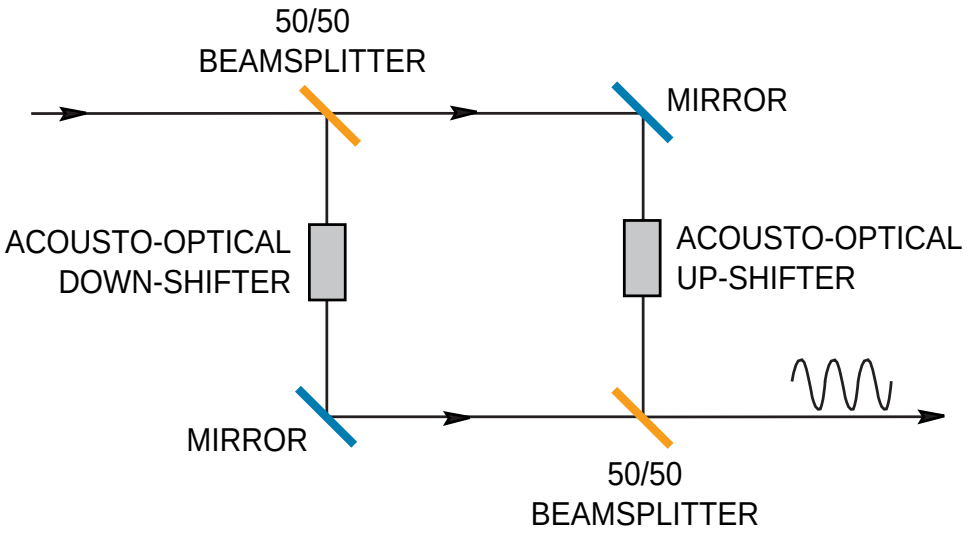

Figure 4-3: Fast modulation of laser intensity by two acousto-optical frequency shifters.

into one. The two frequencies, which are present in the beam, produce "beating" in form of sinusoidal modulation at twice the shifter frequency (i.e. around 80 MHz).

The modulation efficiency α_m would be 1 if powers of the up- and down-shifted beams were equal. However, scattering coefficients η_1 and η_2 (fractions of power going into a scattered beams) for the two shifters used in the C-Mod PCI diagnostic are different (0.8 and 0.25 respectively). This reduces α_m, although not significantly:

$$\alpha_m = \frac{I_{max} - I_{min}}{I_{max} + I_{min}} = \frac{2\sqrt{\eta_1 \eta_2}}{\eta_1 + \eta_2} \approx 0.85 \ , \tag{4.7}$$

where I_{max} and I_{min} are the maximum and the minimal intensities of the combined beam.

Figure 4-4 illustrates the actual acousto-optical frequency shifters used on C-Mod. The shifters are attached to tiltable mounts that allow adjustments for maximum Bragg scattering efficiency. They are powered by about 50 watts of 40 MHz signal each and therefore require water cooling for continuous operation.

The modulation performance was verified by arranging both shifters to increase the optical frequency of the laser, although by a different amount (40.0 and 40.1 MHz). Modulation with right efficiency was then directly observed by a detector at 100 kHz.

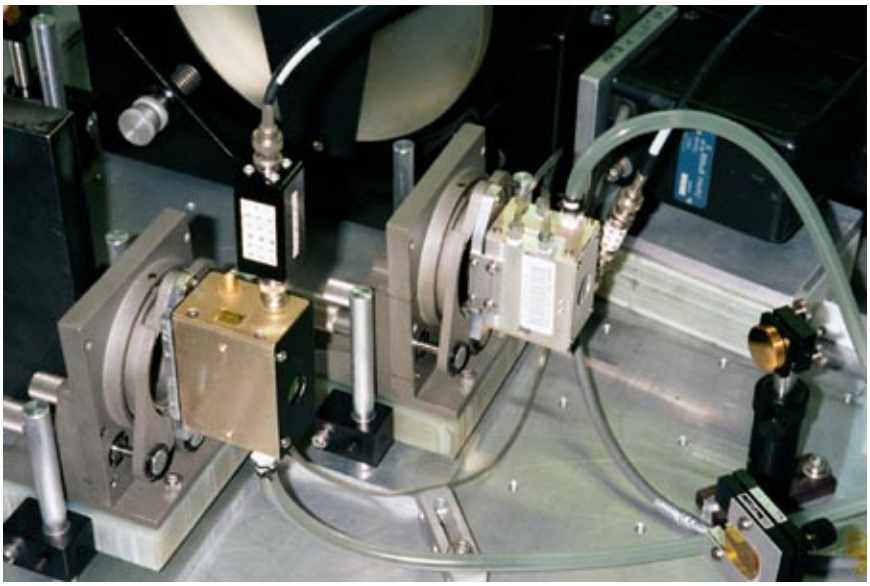

Figure 4-4: Two acousto-optical frequency shifters used in the PCI diagnostic.

4.3 Interpreting the Signal

When running the PCI diagnostic in the optical heterodyning regime, the signals from the 12 channels are directly digitized at 10^6 samples/s, just as they normally are. However, the recorded signal is now different. Figure 4-5 illustrates the spectrum evolution of a single channel signal for a shot where the fast magnetosonic wave was observed. For this shot, the laser modulation frequency was set to 80.2 MHz and the antenna operated at 80.5 MHz. One would expect a heterodyned signal to show up at the beat frequency (around 300 kHz in this case) and, indeed, there is a strong coherent fluctuation present in the signal at 300.9 kHz. It can be seen as a bright horizontal line in frequency-time space or as a sharp peak in the instantaneous spectrum (Fig. 4-5, insert).

To extract information about amplitude and wavenumber of the ICRF wave some additional processing is needed. First, one needs to know the exact value of the beat frequency. The digital readouts of the used frequency synthesizers cannot be trusted because of their limited precision. For example, in the shot described above there is a 0.9 kHz difference between the expected and the actual locations of the heterodyned signal. Instead, the beat frequency can be obtained by looking at a high-resolution

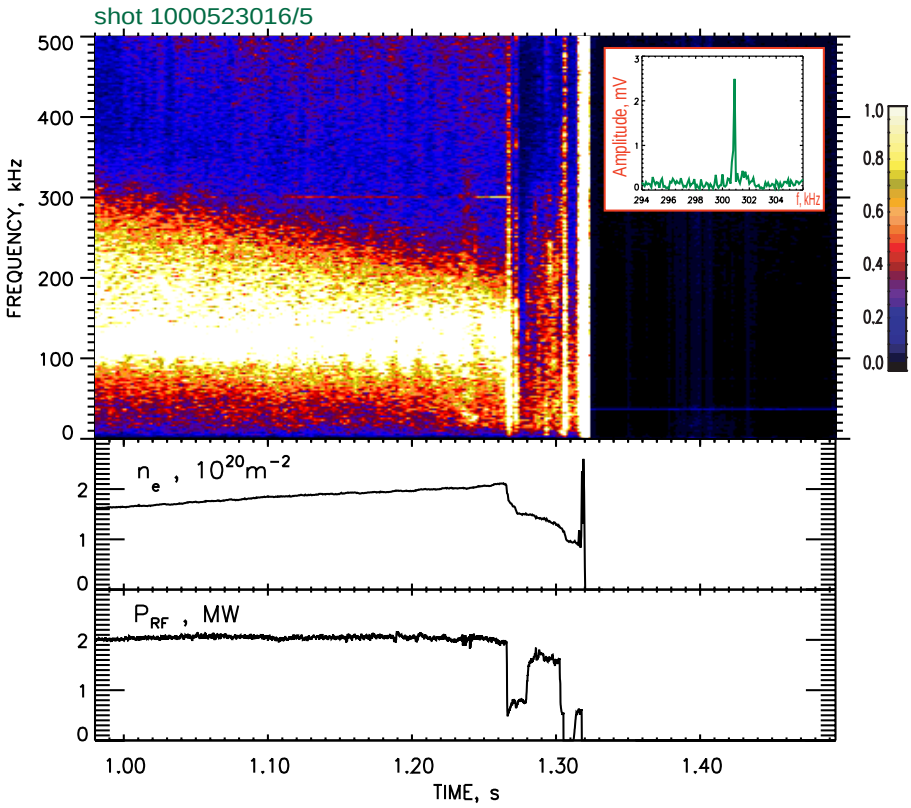

Figure 4-5: PCI signal with optical heterodyning in the frequency-time space. Also the central plasma density and the applied RF power are shown.

(10 Hz or better) spectrum. The heterodyned signal peak is usually easily resolved, and its center frequency should be used for further analysis. In the next step all 12 PCI signals are split into simultaneous time slices, and amplitudes of the beat frequency harmonic are extracted. These are generally complex numbers and carry information about the heterodyne signal phase as well. By performing a spatial Fourier transform of the 12 complex amplitudes one can find the predominant wavenumbers and phase velocity direction for each time slice. It should be noted, that if the laser modulation frequency is higher than the RF wave frequency, the phase velocity direction will appear reversed. The length of the time slices is determined by the required time resolution. Also, it should be close to an integer number multiple of the beat period so that all information about the heterodyne signal would be concentrated in a single harmonic.

The bandwidth of the heterodyne signal is usually very small (50 Hz or less). Normally, it may be filtered out and the rest of the signal can be used to study low frequency fluctuations in the same manner as it was done earlier.

4.4 Sensitivity of the System

The sensitivity of the PCI system to heterodyne measurements of RF waves is quite different from the sensitivity for direct low frequency fluctuation measurements. Due to the diagnostic design, there is no way to distinguish between the RF signal reduced to the beat frequency and the spontaneous plasma fluctuations occurring at this frequency directly. Both signals mix together, although the heterodyne signal is usually dominant. The low frequency plasma fluctuations become the major source of noise for heterodyne measurements.

Figure 4-6 illustrates the relative strength of signals in the typical PCI spectrum. The heterodyne signal is represented by a sharp peak and is easily separated from the rest of the spectrum. It is advantageous to place this peak in the high end of the spectrum (above ~ 300 kHz) where the broadband PCI signal is lower and produces less interference with the RF signal. For example, in Fig. 4-6(a) the broadband

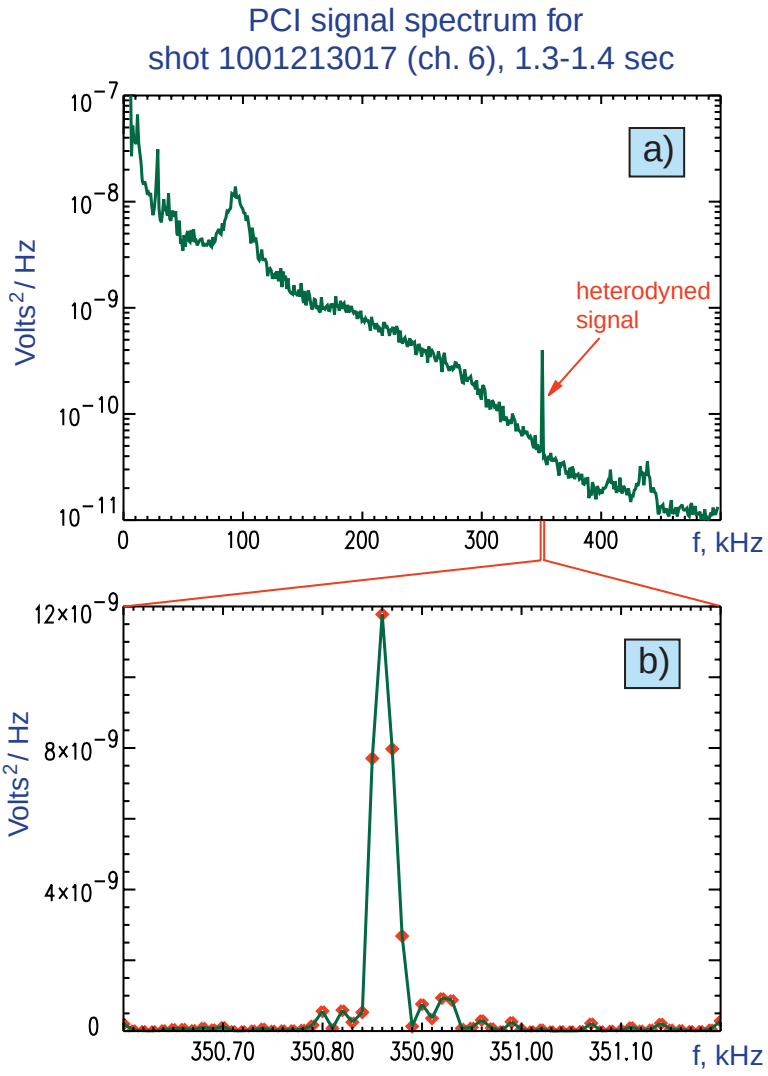

Figure 4-6: The PCI signal spectrum with optical heterodyning; (a) full frequency range, 1 kHz resolution; (b) zoom into the beat frequency range, 10 Hz resolution.

fluctuations amount to $4{\times}10^{-11}$ V^2/Hz in the beat frequency vicinity. Additionally, the sensitivity to RF signal is also determined by the required measurement bandwidth. One should account for factor $\alpha_m/2$ lower responsivity for heterodyned signal (Eq. 4.5) as well. Combined, one can get the sensitivity of about $2.6{\times}10^{13}$ m$^{-2}/\sqrt{\text{Hz}}$ for a shot shown in Fig. 4-6. That is about 0.005% of the core plasma density assuming 10 cm integration length and 1 kHz bandwidth. However, this is just a typical number. The actual sensitivity is individual for every shot.

4.5 Phase Measurements

In its current design, the PCI system does not provide any information about the phase of the observed ICRF wave (relative to the phase of the launching antenna). This is because the frequency synthesizer used to modulate the laser beam operates independently and is not locked to the antenna frequency.

When a wave propagates from the antenna to the point of PCI observation, it gathers the information about those plasma parameters that affect its wavelength (such as plasma density) and stores them in integrated form in its phase. Knowing the phase may help to extract this information. More important, computer codes used to simulate ICRF wave propagation also calculate the wave phase. Development of these codes may benefit from comparing predictions with experimental measurements.

In an attempt to measure the wave phase, the author of this thesis built a special dual stage phase-locked-loop (PLL) circuit (Fig. 4-7). This circuit links together the RF antenna, modulation of the laser beam and the digitizer sampling rate. One period of the beat frequency then corresponds to exactly five digitizer cycles, and the wave phase can be measured through a simple spectral analysis.

The major component of the circuit is a 40.1 MHz voltage controlled crystal oscillator (VCXO). Its operating frequency can be adjusted within a small range by applying external voltage. The VCXO output is mixed with square waveform obtained from the RF antenna reference signal by division by 2 and produces roughly 100 kHz beat signal. The phase of this signal is then compared to the phase of a

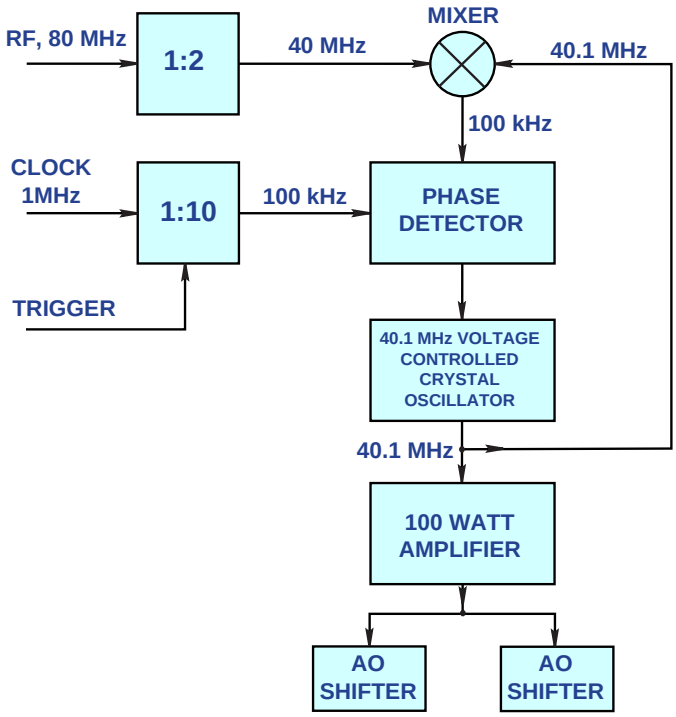

Figure 4-7: Schematic diagram of the dual stage phase-locked-loop circuit for driving acousto-optical frequency shifters.

1/10 clock rate signal. The result of this comparison is then fed back to control the 40.1 MHz VCXO frequency. Eventually, the VCXO frequency is doubled when the two acousto-optical shifters are combined to modulate the laser beam.

Unfortunately, the phase measurement proved to be unsuccessful, although the right frequency was synthesized. The problem is that the high gain (70 dB) amplifier used in conjunction with the circuit is too susceptible to the RF pickup at 80.0 MHz from the nearby megawatt antenna, and it introduces small (less than 0.05%) 200 kHz amplitude modulation in the laser intensity. This modulation is undistinguishable from the smaller heterodyned signal and completely suppresses it. Better shielding of the electronic components may help resolve this issue in the future.

Chapter 5

Fast Wave Detection and Modeling

This chapter covers results of the measurements of the fast wave propagation obtained by the PCI diagnostic using optical heterodyning. The experimental data are then compared with predictions of three dimensional full wave computer modeling.

5.1 Introduction

5.1.1 Fast Magnetosonic Wave

The *Fast Magnetosonic Waves* (also known as the *Compressional Alfvén Waves* or simply the *Fast Waves*) are the primary kind of waves launched by the C-Mod ICRF antennas. These waves propagate mostly perpendicular to the tokamak magnetic field $\mathbf{B}_0$, but can also have a significant wavenumber component along it. The fast wave dispersion relation can be obtained by appropriate manipulation of the Maxwell equations

$$\nabla \times \mathbf{E}_1 = -\frac{1}{c}\frac{\partial \mathbf{B}_1}{\partial t} \tag{5.1}$$

and

$$\nabla \times \mathbf{B}_1 = \frac{1}{c}\frac{\partial \mathbf{E}_1}{\partial t} + \frac{4\pi \mathbf{J}_1}{c} \ , \tag{5.2}$$

where the subscript "1" designates only the perturbed by the wave component. For perturbations of the type $e^{i\mathbf{k}\cdot\mathbf{x}-i\omega t}$, and defining the dielectric plasma tensor $\bar{\mathbf{K}}$ as

follows:

$$\mathbf{E}_1 + i\frac{4\pi\mathbf{J}_1}{\omega} \equiv \bar{\mathbf{K}} \cdot \mathbf{E}_1 \tag{5.3}$$

one can get

$$\mathbf{N}(\mathbf{N} \cdot \mathbf{E}_1) - N^2\mathbf{E}_1 + \bar{\mathbf{K}} \cdot \mathbf{E}_1 = 0 \ , \tag{5.4}$$

where $\mathbf{N} = c\mathbf{k}/\omega$ is the "index of refraction" vector. The plasma current included in the dielectric tensor is

$$\mathbf{J}_1 = \sum_j n_j q_j \mathbf{v}_{j1} \ , \tag{5.5}$$

n_j, q_j and $\mathbf{v}_{j1}$ are the density, the particle charge and the perturbed velocity of the particles "j". In the cold plasma limit the latter can be directly derived from the momentum equation

$$n_j m_j \frac{\partial \mathbf{v}_{j1}}{\partial t} = n_j q_j \left(\mathbf{E}_1 + \frac{\mathbf{v}_{j1} \times \mathbf{B}_0}{c} \right) . \tag{5.6}$$

After a significant amount of algebra, one can derive the fast wave dispersion relation in the form[60]

$$N_\perp^2 = \frac{(R - N_\parallel^2)(L - N_\parallel^2)}{S - N_\parallel^2} \ , \tag{5.7}$$

where

$$R = 1 - \sum_j \frac{\omega_{pj}^2}{\omega^2} \frac{\omega}{(\omega + \Omega_j)} \ ; \qquad L = 1 - \sum_j \frac{\omega_{pj}^2}{\omega^2} \frac{\omega}{(\omega - \Omega_j)} \ ; \qquad S = \frac{R + L}{2} \ ; \tag{5.8}$$

$$\omega_{pj}^2 = \frac{4\pi n_j q_j^2}{m_j} \ ; \qquad \Omega_j = \frac{q_j B_0}{m_j c} \ . \tag{5.9}$$

Note that the "signed" cyclotron frequency Ω_j is negative for electrons while the plasma frequency ω_{pj} is always positive. $N_\parallel$ and $N_\perp$ designate components of the vector $\mathbf{N}$ which are parallel and perpendicular to $\mathbf{B}_0$. For more information on this derivation the reader may refer to the "Waves in Plasmas" textbook by T.H. Stix [60], who has originally introduced this notation in 1962[61].

Equation 5.7 generally applies to many kinds of waves. However, the fast magnetosonic waves exist in the ion cyclotron range of frequencies (ICRF). In this range

the dispersion relation may be farther approximated as simply

$$\frac{\omega^2}{k^2} = v_A^2 \ , \tag{5.10}$$

where v_A is called the Alfvén speed:

$$v_A^2 = \frac{c^2}{1 + \omega_{pi}^2/\omega_{ci}^2} \approx \frac{c^2\omega_{ci}^2}{\omega_{pi}^2} = \frac{B^2}{4\pi m_i n} \ . \tag{5.11}$$

However, this approximation breaks down near the $\omega = \omega_{ci}$ point, where L and S parameters exhibit singularities.

The $\mathbf{E}_1 \times \mathbf{B}_0$ drifts in the fast wave induce variations in the plasma density and therefore allow detection of these waves by the PCI diagnostic. In a hot plasma, changes in density also cause changes in plasma pressure and add "sonic" effects to the dispersion relation:

$$\frac{\omega^2}{k^2} = \frac{v_A^2 + c_S^2}{1 + v_A^2/c^2} \ , \tag{5.12}$$

where $c_S^2 = (\gamma_e K T_e + \gamma_i K T_i)/m_i$ is the plasma sound speed. In a low-β plasma (β is the ratio of plasma pressure to the magnetic field pressure) such as in C-Mod the "sonic" effects are usually negligible. For example, for deuterium plasma with $T_e = T_i = 2$ keV, $B_0 = 5$ T and $n = 5 \times 10^{14}$ cm^{-3} one can get $\beta = 0.032$, $c_S = 570$ km/s and $v_A = 3500$ km/s . The "sonic" effects contribute to only 2% difference in the dispersion relation.

5.1.2 ICRF Antennas

Three ICRF antennas are used to launch fast magnetosonic waves in the Alcator C-Mod tokamak. Fig. 5-1 shows two of these antennas located at the D and E vacuum vessel side ports (there is a total of 10 such ports labeled from A to K). Each antenna is made of a couple of vertical current straps separated from the plasma by a screen of slanted metal rods (called the Faraday shield). The screen is needed to protect the straps from interacting with a plasma. It transmits only the component of electric field perpendicular to the rods; the latter are aligned along the dominant

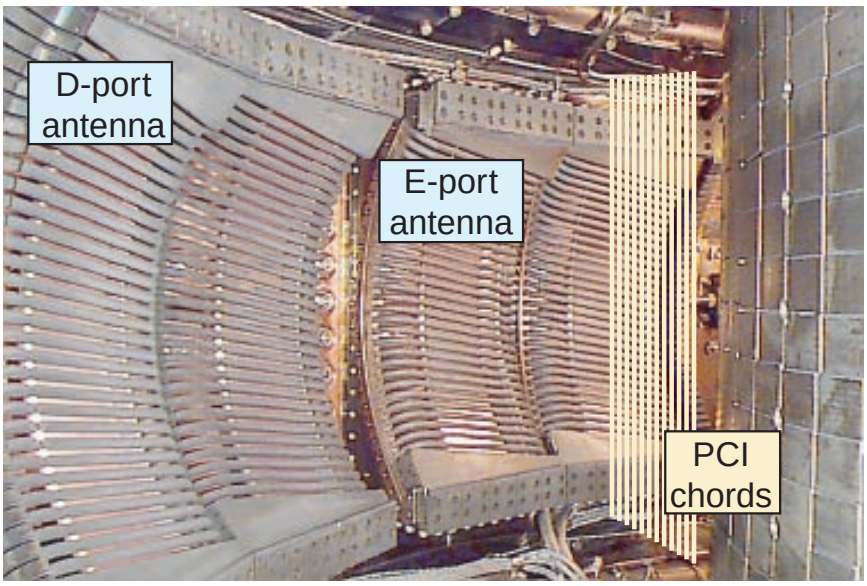

Figure 5-1: Two ICRF antennas used for plasma heating on the Alcator C-Mod tokamak. The PCI laser passes vertically in front of the E-port antenna.

magnetic field. The operating frequencies for the D- and E-port antennas are 80.5 and 80.0 MHz respectively, and the straps are phased (0,π) in both of them. Each antenna is capable of coupling up to about 2 megawatts of power to the plasma which provides a considerable amount of auxiliary heating (ohmic heating typically accounts for only about 1 MW).

The third ICRF antenna is located at the J port. It features a similar design to the D and E antennas but it has a total of four current straps instead of just two. Additionally, the phasing of the straps can be varied. This allows some directionality in the toroidal antenna spectrum, making it possible to launch waves preferentially in the same or opposite direction as the plasma toroidal current. Setting the strap phasing to $(0, \pi/2, \pi, 3\pi/2)$ is expected to drive currents in the toroidal direction (the fast wave current drive). The J-port antenna operates in at 78 MHz and should be able to generate of up to 3-4 MW of auxiliary heating.

The PCI laser beam passes through the plasma vertically in front of the E-port antenna, about 20 cm away from its Faraday shield. The beam is also close to the D-port antenna which is located just 36° away toroidally. The J-port antenna is positioned farther away: 144° from the PCI beam, more than 1/3 of a complete turn

away. Similar operating frequencies of the antennas allow the PCI diagnostic to be sensitive to their launched fast waves with just minor adjustments in the electronics and optics.

5.2 Fast Wave Modeling Using the Full Wave Code TORIC

The fast wave detection by the PCI diagnostic has a relatively complicated geometry. The strongest signal is observed to come from the D-port RF antenna, which is separated by 36° toroidally from the PCI detection plane. Additionally, the measurements are line integrated along vertical lines.

To better interpret the results, the fast wave propagation was modeled using the numerical code TORIC[14, 62]. The model used in this code carefully describes waves in the ion cyclotron frequency range, including the fast magnetosonic wave. Hot plasma effects, such as finite Larmour radius and Landau damping, are also included. Each solution provided by TORIC is only two-dimensional (in the poloidal plane). This section discusses how multiple solutions are assembled to generate a full three dimensional field distribution inside a tokamak plasma, including propagation in the toroidal direction. The obtained electric fields are then converted into expected line integrated density fluctuations.

Figure 5-2 illustrates a single 2D TORIC solution for a typical Alcator C-Mod plasma. An instantaneous value of the E_+ field is shown, which is a circularly polarized component of the electric field perpendicular to $\mathbf{B}$. The fast wave is seen originating near the antenna strap and propagating towards the plasma center. The amplitude of the field increases as the wave gets more focused. On the side of the plasma closer to the tokamak inner wall the amplitudes of the forward and reflected fast waves are approximately equal and a standing wave pattern is formed. Grid size for all modeling done in this thesis was chosen to be 33 points poloidally (15 poloidal modes) and 240 points radially — this is sufficient to resolve relatively long wave-

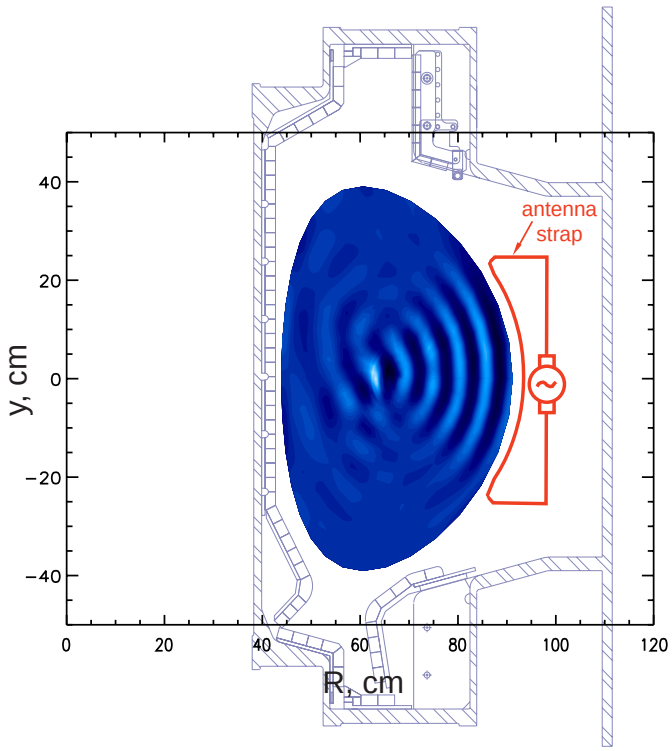

Figure 5-2: A 2D distribution of electric field E_+ generated by a numerical code TORIC.

length fast waves. The simulated plasma shape is set by the real plasma elongation and triangularity. Higher order profile distortions are ignored.

5.2.1 Generating 3D Field Solutions

The particular solution shown in Fig. 5-2 is created for only one of the dominant antenna toroidal mode numbers ($N_\varphi = 10$). In this solution the amplitude of the field is uniformly distributed in toroidal directions while its phase is changing by $2\pi N_\varphi$ over a single toroidal turn. Naturally, in real plasma more than just one toroidal mode is excited. If all present modes are added together then one would obtain a three dimensional distribution of the electric field.

The different N_φ modes should be added with appropriate phase and weight factors. The following model is used to calculate these coefficients. The electric field is assumed to be constant across antenna straps and oriented parallel to them. Since the D- and E-port antenna straps are always phased $(0, \pi)$ the fields of the two straps are

taken to have opposite signs. Finally, the electric field is assumed to change linearly between the two straps and between each strap and the antenna box wall (where it reduces to zero). Figs. 5-3(b) and (c) illustrate this distribution. Taking its Fourier transform then results in the antenna toroidal mode number spectrum (Fig. 5-3(a) shows its absolute value; the phases are not shown). When the multiple TORIC solutions are combined in accordance with this spectrum the electric field is verified to look like Fig. 5-3(b) in the antenna strap plane.

Figures 5-4(a) and (b) illustrate the combined solution away from the antenna. A real part and an absolute value of the complex-number electric field component E_y are shown on the plasma horizontal midplane. These represent an instantaneous field value and its oscillation amplitude respectively. The fast magnetosonic wave is seen originating at the antenna straps and propagating away toward the tokamak center. It gets stronger near the plasma axis because of the poloidal focusing despite the wave toroidal expansion. Node-antinode pattern may be noticed farther toward the tokamak inner wall in Fig. 5-4(b) - an evidence of a standing wave in a plasma region where the forward and the reflected wave amplitudes are approximately equal. In some areas (especially on the right part of Fig. 5-4(a)) the reflected wave dominates. Another important observation is that the field is essentially zero on the line connecting the tokamak and the antenna centers. The destructive interference from the waves driven by two out-of-phase antenna straps effectively eliminates E_y field in this area.

As seen from the antenna N_φ spectrum (Fig. 5-3), most of the wave power is concentrated in the ± 26 range of the toroidal mode numbers. To evaluate the importance of higher mode numbers the solutions were compared for an identical scenario but keeping ± 26, ± 45 and ± 60 modes. No significant changes were detected in the 3D solutions. Two arguments may explain such behavior. First, the high number (> 26) toroidal modes represent only a minor fraction of the antenna spectrum. Second, the higher number mode wavelength is much smaller than the 3.75 m wavelength of the 80 MHz wave in vacuum. Even if taken into account, these modes decay quickly in the near-vacuum region between the antenna straps and the plasma boundary and

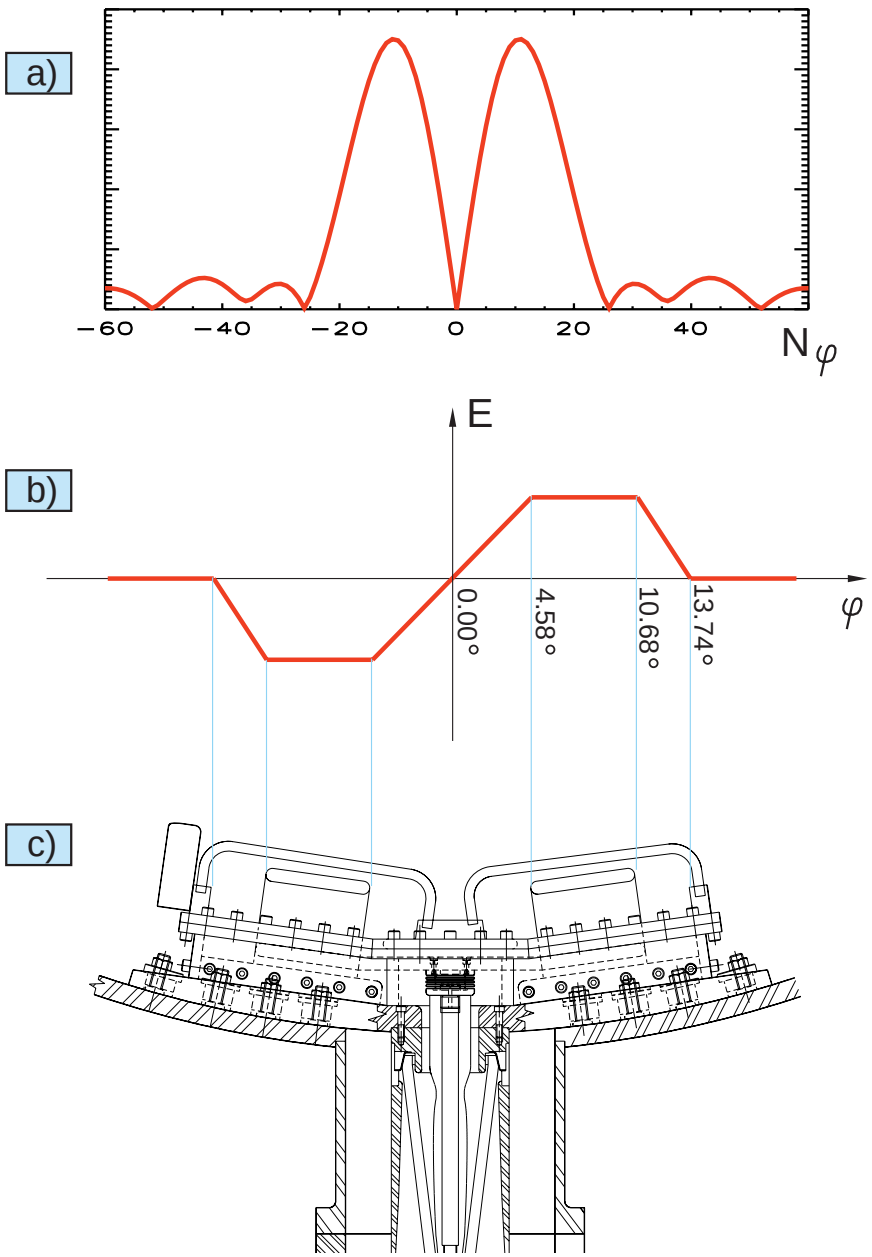

Figure 5-3: (a) Toroidal antenna mode number spectrum; (b) Electric field distribution at the antenna straps; (c) Top view of the D(E)-port ICRF antenna.

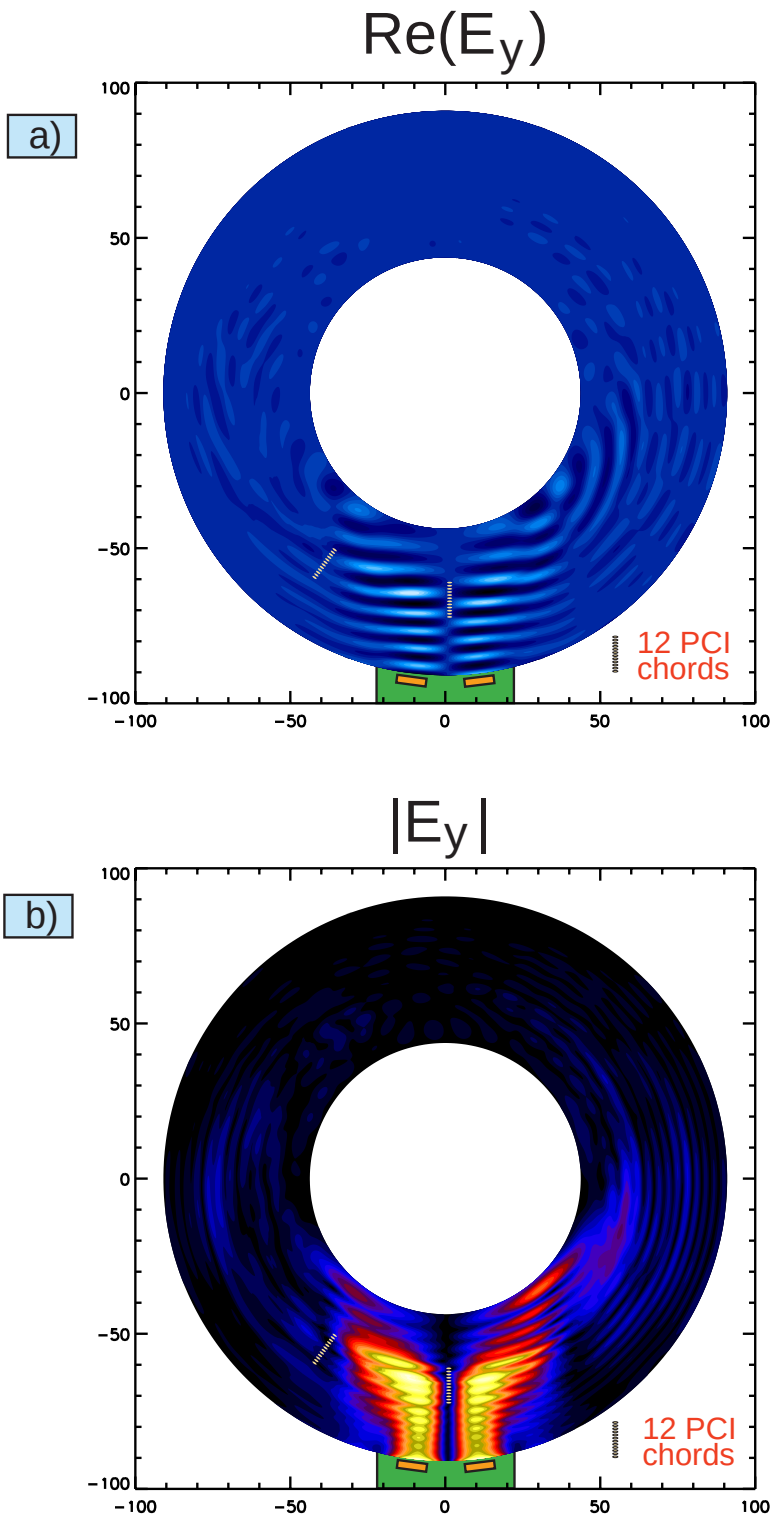

Figure 5-4: A horizontal midplane slice of the TORIC 3D solution. Two locations of the 12 PCI integration chords are shown. For the E-port antenna the chords are located on the antenna midplane; for the D-port they are 36° away. (a) instantaneous E_y distribution; (b) E_y amplitude.

do not affect much the computed field amplitudes in the dense plasma region.

5.2.2 Normalization of the Electric Field Amplitude

Typically, the TORIC solutions are normalized per unit current in the antenna strap plane. Unfortunately, no good estimates of the antenna strap currents are available on the C-Mod tokamak. Even if these measurements were available, one would also need to know current distribution in the walls of the antenna box to assemble a normalized 3D field distribution.

Instead, a well known value of the radiated antenna power is used to normalize the field amplitudes in this thesis. In a plane wave configuration $\mathbf{k} = k_x\hat{\mathbf{x}} + k_z\hat{\mathbf{z}}$, $\mathbf{B}_0 \parallel \hat{\mathbf{z}}$ the time average Pointing vector is given by[60, 63]:

$$\mathbf{P} = \frac{c}{16\pi}\Big(\mathbf{E}^* \times \mathbf{B} + \mathbf{E} \times \mathbf{B}^*\Big) = \frac{c^2}{8\pi\omega}(E_y^2 k_x \hat{\mathbf{x}} + E^2 k_z \hat{\mathbf{z}}) \ , \tag{5.13}$$

$$E_x/E_y = i\omega/\omega_{ci} \ . \tag{5.14}$$

Using this equation, a Pointing vector flux coming from the antenna may easily be computed for a given 3D solution. In this thesis, the integration area for flux calculation was taken to be a portion of the plasma flux surface about 5 cm away from the Faraday shield and of the area slightly exceeding the antenna box dimensions. This surface needs to be sufficiently inside the plasma region so that the fast wave wavenumber does not change radically over a single wave period and can be substituted in Eq. 5.13. By equating the calculated flux with the know radiated power the 3D solution can be normalized in real units. For example, for $P_{RF} = 2$ MW, $B_0 = 4.3$ T, $n = 3 \times 10^{14}$ cm^{-3} the fields where found to peak at about 40 kV/m next to the antenna Faraday shield and 70 kV/m near the plasma axis (where the wave is focused).

5.2.3 Computing the Density Fluctuations in the Fast Wave

The PCI diagnostic is sensitive to changes in plasma density. Therefore, to compare results of experimental wave measurements and TORIC 3D modeling the computed electric field amplitudes must first be converted to line integrals of density fluctuations. In the fast magnetosonic wave, the density fluctuations are caused primarily by divergence of the $\mathbf{E}_1 \times \mathbf{B}_0$ flows[64]. These flows are fairly easy to calculate when the 3D electric field amplitudes are known from TORIC. The results are then interpolated onto a rectangular grid, integrated along the vertical lines and differentiated across the horizontal plane. The result is the line integrated amplitude of density fluctuation caused by the fast wave that can be directly compared to the PCI heterodyned measurements.

5.3 Fast Wave Detection by the PCI

The fast wave has been observed by the phase contrast imaging diagnostic in a number of shots. One of such measurements (shot 1000523016) is illustrated in Fig. 4-5 (page 126) in Chap. 4. In that case, the diagnostic was operated in the optical heterodyning mode with the laser beam intensity modulated at 80.2 MHz. A strong coherent oscillation was observed at approximately 300 kHz which corresponded to a heterodyned signal of the wave launched by the D-port ICRF antenna at 80.5 MHz.

Figure 5-5 illustrates an instantaneous two dimensional spectrum of the PCI signal taken in this shot at $t = 1.26$ s (at this time slice the observed RF signal was especially strong). Two separate peaks are present in the spectrum. Both peaks feature the same frequency of 300.9 kHz which represents waves launched by the D-port antenna. The wavenumbers of the peaks have the same magnitude but different signs (+1.8 and -1.8 cm^{-1}). This can be attributed to two waves governed by the same dispersion relation (fast magnetosonic waves in this case) but traveling in the opposite directions. A stronger peak with a negative wavenumber corresponds to a wave propagating in the direction of the major radius decrease and therefore away from the ICRF antenna. The somewhat weaker second peak represents the fast wave reflected from

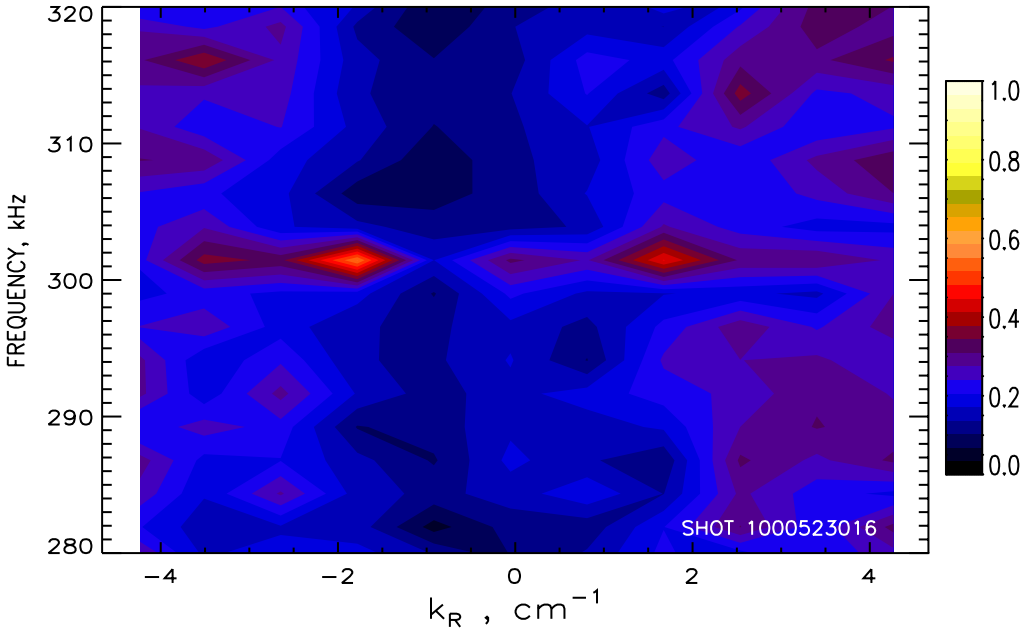

Figure 5-5: Fast wave is detected at the 300 kHz beat frequency. Two peaks correspond to a wave number of $\pm 1.8\ cm^{-1}$.

the tokamak inner wall and moving towards the antenna.

The measured wavenumber may be compared to the one predicted by the cold plasma fast wave dispersion relation (Eq. 5.7). Figure 5-6 shows the density profile and the calculated wavenumber for the shot 1000523016 at $t = 1.26$ s (the same shot and time as used earlier). In this calculation the $N_{\|}$ is taken to vary as $cN_{\varphi}/\omega R$, where N_{φ} is the dominant antenna toroidal mode number ($N_{\varphi} = 10$ for the D-port antenna) and R is the major radius and $B_0 = 4.3$ T on the plasma axis. There is a singularity in the dispersion relation at $R = 56$ cm where the antenna frequency matches the hydrogen ion gyrofrequency (the plasma composition was 95% deuterium and 5% hydrogen for the shot). Overplotted on the same figure are the locations of the PCI integration chords. As one can see, the dispersion relation predicts a wavenumber of about 1.5 cm^{-1} for the fast wave at the location of the PCI viewing, which is in a good agreement with the measured results. The relatively small discrepancy may be attributed to uncertainty in the density measurement and, possibly, simplicity of the model. Later in this chapter results of full three dimensional modeling including all antenna toroidal modes and hot plasma effects will be examined.

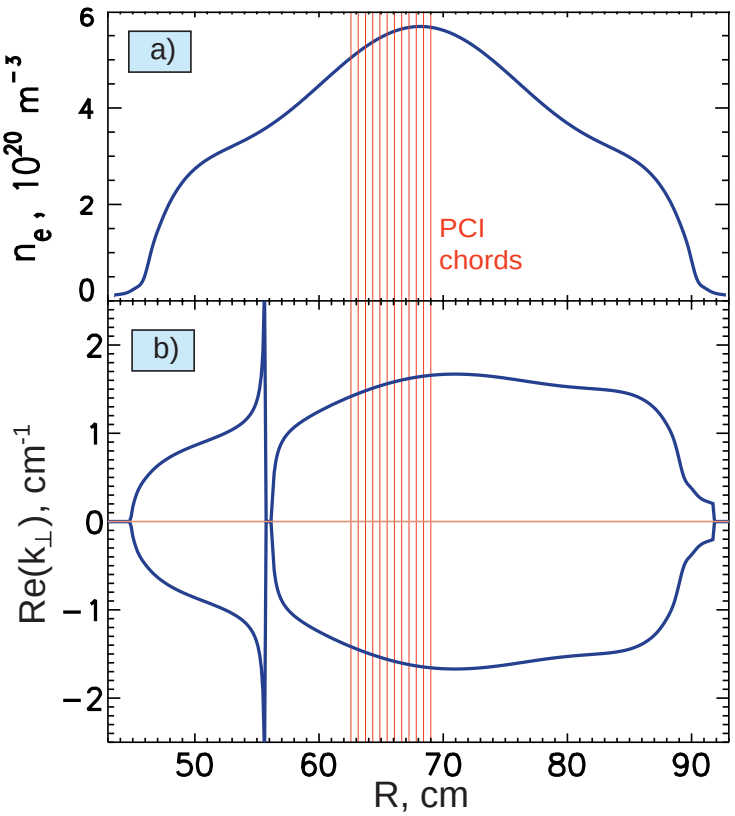

Figure 5-6: Density profile (a) and the fast wave dispersion relation (b) vs. major radius for the shot 1000523016. Also shown are the locations of the PCI integration chords.

Figure 5-7 shows the development of the measured wave spectrum during plasma density peaking in the shot 1001213017. Again, a heterodyned signal corresponding to the D-port RF antenna is shown; the point of observation is 36° away toroidally from the antenna center. Strong fast wave signals appear on the plot at $k_R = \pm 2$ cm^{-1}; positive and negative wavenumbers correspond to the waves propagating towards and away from the antenna. As the central density rises, strong variations in the wave amplitude are observed as well as in the forward/reflected wave balance. Particularly a strong reflected wave signal is detected first around $t = 1.2$ s, followed by a large forward wave signal about 100 ms later. A possible explanation for such behavior is that the rise in density increases the index of refraction of the plasma and causes divergence of the fast waves. First, the waves are concentrated mostly in front of the antenna and do not propagate well to the PCI location. As the pattern diverges, the waves reflected from the tokamak inner wall first come into the PCI view. As it continues to diverge further, the forward proparating wave begins to be detected too, while the reflected wave signal starts to fade. However, detailed 3D computer modeling may provide a better explanation for the observed effects.

The above examples demonstrate the ability of the phase contrast imaging diagnostic to provide localized measurements of amplitude, wavenumber and direction of ICRF waves existing in a tokamak plasma. Multiple waves can be simultaneously detected and identified since the diagnostic measures a complete wavenumber spectrum. As of writing of this thesis, the optically heterodyned PCI is the only non-disturbing diagnostic available for such detailed measurement of fast magnetosonic waves in tokamak plasmas. Of the other diagnostics available, the heterodyned reflectometer at DIII-D[65] was capable of only evaluating a relative amplitude of a fast wave in a single location in a plasma. The scanning magnetic probe setup[66] cannot be used in high density tokamak plasmas.

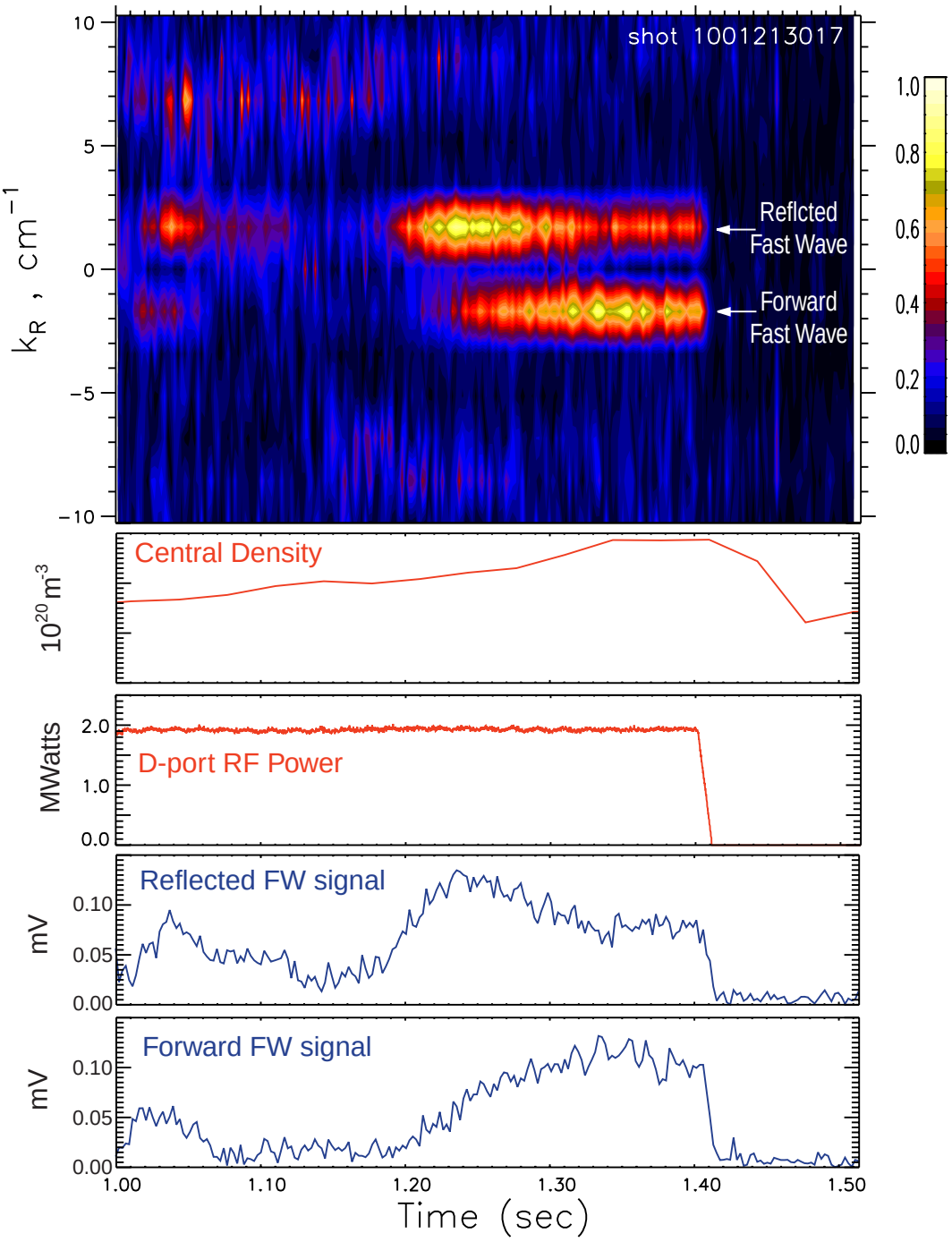

Figure 5-7: Time evolution of the measured wave spectrum during plasma density rise.

5.4 Experimental Measurements vs. Numerical Modeling Results

In the shot 1000523016 shown earlier in Fig. 4-5 (page 126) the observed fast wave signal amplitude changes considerably while the radiated antenna power stays constant at about 2 MW. One important parameter that was changing during that time was plasma density profile, most other parameters were constant. The central density has reached almost 6×10^{14} cm^{-3} before the plasma collapsed. As the density profile was becoming more peaked the fast wave signal grew stronger. In this thesis results of the measurements and the modeling are compared for the two time slices $t = 1.10$ s and $t = 1.26$ s, namely the moments when the observed signal is barely detectable and when it is at maximum. Large amount of computer time needed to compute multiple 2D TORIC solutions for each time slice prevents analysis of more time slices and different shots at this time.

The wave detected in the shot 1000523016 is coming from the D-port antenna, meaning that the measurements are performed 36° away toroidally from the antenna midplane. The density profiles are shown in Fig. 5-8(a). The second profile shows a presence of an internal transport barrier in the plasma (at 60 and 80 cm) caused by off-axis ICRF heating[67]. The magnetic field stayed constant at $B_0 = 4.3$ T in the analysis. The 3D electric field structure (reconstructed as discussed earlier in this chapter) is shown in Fig. 5-8(b). In the case of more peaked density profile the fast wave is seen to diverge less toroidally until it reaches the plasma axis. Then much stronger poloidal focusing causes the electric field amplitude to peak even at the location of the PCI viewing. However, better focusing decreases the effective integration length for the region of high fast wave amplitude. This results in nearly identical magnitude of line integrated density fluctuations in the PCI region for both scenarios (Fig. 5-8(c)). However, the predicted wavenumber spectra are quite different for the two time slices. In the peaked density case the wave is predicted to propagate mostly away from the antenna (negative k_R), while mostly the reflected wave should be seen for the $t = 1.10$ s case (Fig. 5-8(d)). Finally, Fig. 5-8(e) shows the wavenumber

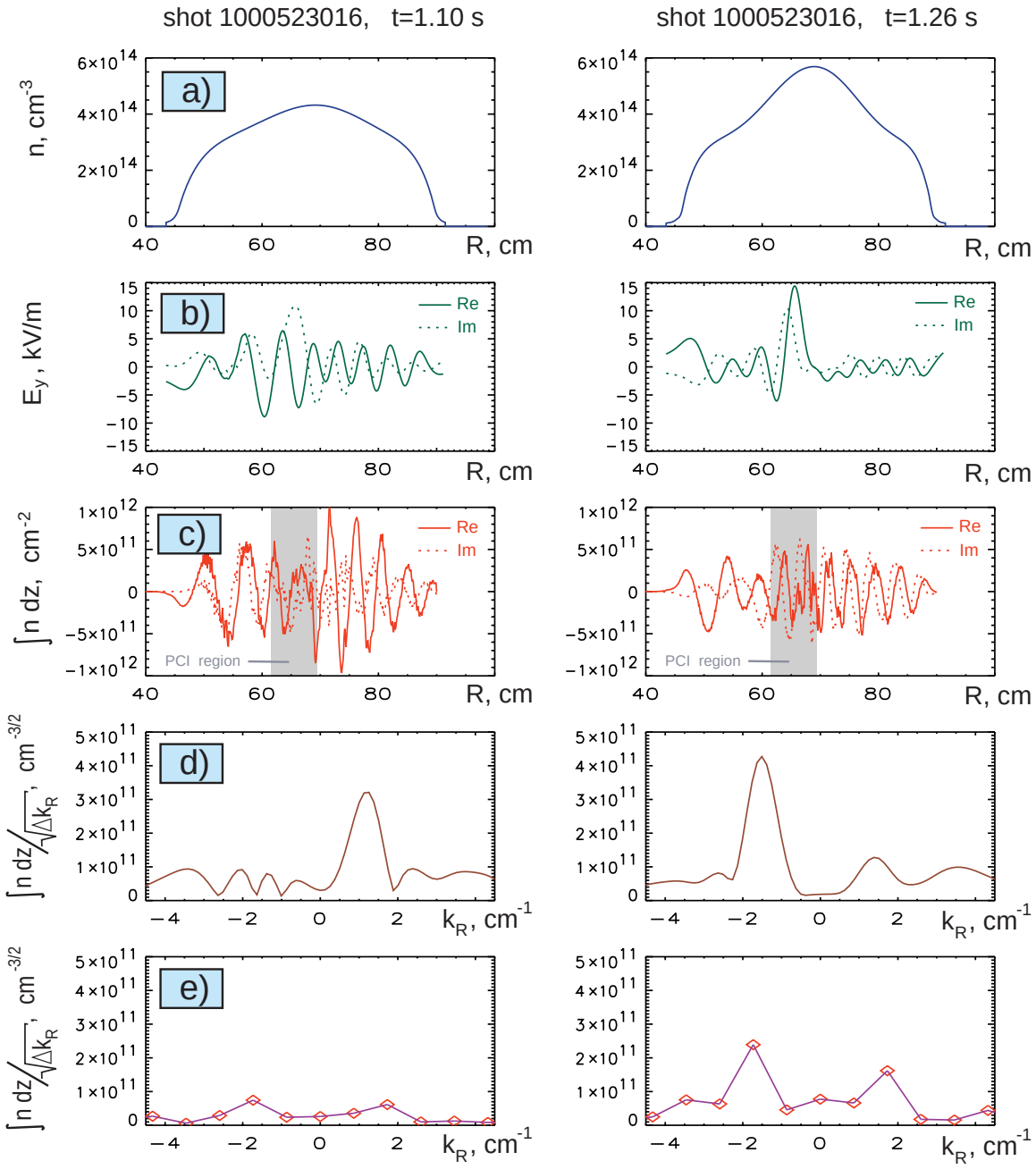

Figure 5-8: Measurements vs. modeling comparison. (a) plasma density profiles; (b) electric field in the horizontal midplane; (c) line integrated amplitude of density oscillations; (d) and (e) wavenumber spectrum of density fluctuations from the modeling and the PCI measurements respectively. (b)-(e) are for the location 36° away from the antenna vertical midplane

spectra measured experimentally by the PCI diagnostic.

The agrement between the predicted and measured spectra is excellent for the $t =$ 1.26 s case. The dominant wavenumbers and forward/reflected ratio agree perfectly, and the absolute magnitudes agree to within less than a factor of 2 (which is very good since there some significant uncertainties in many parameters used in the analysis). The agreement in $t = 1.10$ s is less perfect but still is within an order of magnitude.

An interesting results is that the fast wave launched by the E-port antenna was never detected by the PCI clearly above the noise level. This is in complete agreement with the 3D modeling and simple laws of wave propagation since there should be destructive interference of the fast wave on the vertical midplane of a 2-strap antenna when the straps are driven completely out of phase.

The conclusions that can be made after considering only two modeling cases (with less than perfect agreement in one of them) are of somewhat speculative character and further research will be needed with more detailed measurements and modeling. However, it seems that the model predicts satisfactorily the three dimensional propagation of the fast waves. Focusing effects play an important role in the fast wave propagation. Therefore, even relatively small changes in density profile may cause significant changes in the measured wave amplitude.

5.5 Future Work

The research described in this chapter lays ground to more opportunities both in modeling and experiment. One of the most significant proposals would be to investigate the directionality of the 4-strap J-port antenna. The phasing of the antenna straps is variable and this makes launching the waves preferentially in one direction possible (which is important for non-inductive current drive). The asymmetric location of the PCI laser beam 144° away toroidally is suitable for such measurement. However, the signal magnitude may be a challenge to measure if the wave does not propagate well that far toroidally.

More 3D modeling may be performed, especially when better computers or faster

codes become available. By analyzing many scenarios the better way for combining multiple toroidal modes may be found. Running TORIC with more realistic plasma geometry may also benefit the agreement between the predictions and the experiment.

Chapter 6

Conclusions and Future Work

This chapter provides a brief summary of main results described in the thesis. Then, some suggestions are given for possible future upgrades of the Phase Contrast Imaging diagnostic. Finally, some new possible areas of research are proposed that can be investigated using PCI.

6.1 Conclusions

The following summarizes the main results of this thesis:

- A new diagnostic, Phase Contrast Imaging (PCI), was built from scratch for the Alcator C-Mod tokamak. The diagnostics employs a wide CO_2 laser beam passing vertically through the C-Mod plasma. Special imaging optics is used to convert phase perturbations in the beam (caused by plasma density fluctuations) into image intensity variations on a multichannel detector array. Overall, PCI is capable of providing continuous non-invasive calibrated measurements of density fluctuations in the 2-500 kHz, 0.5-12 cm^{-1} frequency and wavenumber range.

- The Quasi-Coherent fluctuation mode was discovered by the PCI diagnostic in EDA H-mode plasmas. The mode is localized in the density pedestal region, it propagates in the electron diamagnetic drift direction and has frequencies and wavenumbers in the 50-300 kHz and 3-6 cm^{-1} ranges, respectively. The mode

wavenumber scales approximately as $k_\theta \rho_S \approx 0.13$, its observed frequency tends to decrease with temperature and is believed to be doppler shifted by plasma poloidal rotation. The mode is presumed to be responsible for reduced impurity accumulation in the EDA H-mode plasmas and therefore is desirable in future fusion grade plasma operation. By using numerical solutions of the Braginskii equations, we tentatively identify this mode as "resistive X-point mode", a kind of resistive ballooning mode strongly affected by X-point configuration of magnetic field lines.

- The PCI diagnostic was successfully upgraded to include the "optical heterodyning" capability. In this regime, the diagnostic may be used to detect narrowband density perturbations at frequencies as high as ~ 100 MHz by using modulation of the CO_2 laser intensity near the frequency of interest. The main purpose of the upgrade was to observe the propagating ICRF waves during auxiliary plasma heating and current drive.

- Propagation of the Fast Magnetosonic Waves was studied by using the optically heterodyned PCI diagnostic. The wave amplitude, wavelength and direction of propagation have been measured for the first time in dense tokamak plasmas. The measured results are in good agreement with expeected cold plasma dispersion relation. 3D full wave numerical modeling has been performed to study the toroidal propagation characterictics of the fast wave.

6.2 Future Work

Some suggestions for further research of the Quasi-Coherent mode and Fast Magnetosonic Waves have already been given in Chapter 3 and 5, respectively. In this section, we provide some additional recommendations regarding the possible diagnostic upgrades and fluctuation studies using PCI.

6.2.1 PCI Diagnostic Upgrades

The performance of the PCI system may be further improved by implementing certain upgrades. First, we would suggest to increase the number of PCI channels. In the current setup, the diagnostic has only 12 channels, and this limits the resolution in the measured wavenumber spectrum to 12 data points. At the same time, the detector array has a total of 32 channels available. Just by adding preamplifiers and digitizers, the currently unused 20 channels may become available.

The upper limit of the diagnostic frequency range (500 kHz) is determined by the available digitized sampling rate. If faster digitizers are installed (maybe on just a few channels) this limit may be raised up to $\sim$ 10 MHz (limited by the detector bandwidth).

We would also suggest to alter the beam cross section to elliptical shape to better fit the oblong shape of the C-Mod vertical ports (currently the beam is circular). This should produce better uniformity in the channel-to-channel responsivity in experiments requiring a wide beam, i.e. when measuring longer wavelength fluctuations, or if the number of channels is increased. Attention needs to be paid to careful optics alignment since some unavoidable astigmatism distortions may be introduced into the system by cylindrical lenses.

Some modifications can make the system to be completely automated. In the existing configurations, position of the phase plate needs to be adjusted between shots to insure that the diagnostic laser beam is continuously focused on the phase plate groove. Using a stepping motor and some advanced programming of the PLC controller this task can be performed automatically. Adding temperature gauges to the laser and the acousto-optical modulators can reduce the risk of a serious diagnostic breakdown.

6.2.2 Fluctuations Studies

Besides the quasi-coherent mode and the ICRF waves the PCI diagnostic detects large amounts of broadband turbulence. For example, in Fig. 3-1 (page 90), turbu-

lent fluctuations appear first in the 0-200 kHz range in L-mode, then their amplitude significantly increases following the transition to the ELM-free H-mode and their frequency range becomes 100-400 kHz. These fluctuations are also present in the EDA H-mode, although at somewhat lower level compared to the ELM-free period. The observed dispersion relation appears to be linear, with ω/k_R being approximately a factor of two higher in H-mode. The fluctuations appear to originate in the plasma core since the signal associated with them is not detected by the reflectometry diagnostic in dense plasmas (the reflectometry waves penetrate into the plasma core only when the density is relatively low, for example in L-mode, Fig. 3-4).

Thorough studies of these broadband fluctuations may help to evaluate their impact on particle and energy diffusion and overall plasma confinement. Their amplitudes, frequencies and wavenumbers are easily measured by the PCI. The dependence of these parameters on various plasma density and temperature profiles, rotation, etc. awaits to be investigated.

Another area of great interest is the ETG-driven turbulence (Electron Temperature Gradient driven). These fluctuation are expected to have $f \sim$ 5-10 MHz and $\lambda_p \leq 1$ mm. The PCI diagnostic needs to be upgraded to have that high frequency response (as proposed in the previous section). Even then, the short wavelength of the fluctuations will not satisfy the depth-of-focus requirement (Eq. 2.44). Phase scintillation effect will make the diagnostic response dependent on the fluctuation wavelength, and this effect needs to be evaluated carefully. Alternatively, the system may be relatively easily (using the same laser, detector array and most of the optics) converted to the small angle scattering setup to study this type of turbulence.

These topics may be suitable for future thesis projects.

Bibliography

[1] J.A. Snipes, B. LaBombard, M. Greenwald, I.H. Hutchinson, J. Irby, Y. Lin, A. Mazurenko, M. Porkolab. The quasi-coherent signature of enhanced D_α H-mode in Alcator C-Mod. *Plasma Physics and Controlled Fusion*, 43:L23–L30, 2001.

[2] A.E. Hubbard, et al. Pedestal profiles and fluctuations in C-Mod enhanced D-Alpha H-modes. *Physics of Plasmas*, 8(5):2033–2040, May 2001.

[3] *Webster's Electronic Dictionary and Thesaurus*. Random House, Ver. 1.0, College edition, 1992.

[4] J.P. Holdren and R.K. Pachauri. *Energy, An Agenda of Science for Environment and Development into the 21st Century*. Cambridge University Press, 1992.

[5] J.R. Lamarsh. *Introduction to Nuclear Engineering*. Addison-Wesley Publishing Company, 1983.

[6] President's Committe of Advisors on Science and Technology Annual Report. Technical report, 1995.

[7] J. Wesson. *Tokamaks*. Oxford Science Publications, 1987.

[8] I.H. Hutchinson et al. First Results from Alcator C-Mod. *Physics of Plasmas*, 1(5):1511–1518, May 1994.

[9] F. Wagner et al. Development of an Edge Transport barrier at the H-Mode Transition of ASDEX. *Physical Review Letters*, 53(15):1453–1456, October 1984.

[10] M. Greenwald et al. H-Mode Confinement in Alcator C-Mod. *Nuclear Fusion*, 37(6):793–807, 1997.

[11] M. Greenwald et al. Characterization of enhanced D_α high-confinement modes in Alcator C-Mod. *Physics of Plasmas*, 6(5):1943–1949, May 1999.

[12] Eric Nelson-Melby. *Observations of Mode-Converted Ion Bernstein Waves in the Alcator C-Mod tokamak*. PhD thesis, Massachusetts Institute of Technology, 2001.

[13] E. Nelson-Melby, A. Mazurenko, M. Porkolab, P.T. Bonoli, S.J. Wukitch. Phase Contrast Imaging of Ion Bernstein and Fast Waves in Alcator C-Mod. In *Proceedings from the 14th Topical Conference on Radio Frequency Power in Plasmas*, Oxnard, California, May 2001.

[14] M. Brambilla. Electron Landau damping of ion Bernstein waves in tokamak plasmas. *Nuclear Fusion*, 38(12):1805–1818, December 1998.

[15] N.A. Krall, A.W. Trivelpiece. *Principles of Plasma Physics*. McGraw-Hill Book Company, 1973.

[16] I.H. Hutchinson. *Principles of Plasma Diagnostics*. Cambridge University Press, 1987.

[17] M.V. Klein, T.E. Furtak. *Optics*. John Wiley & Sons, 1986.

[18] F. Zernike. Beugungstheorie des Schneidenverfahrens und Seiner Verbesserten Form, der Phasekontrastmethode. *Physica*, 1:689–704, 1934.

[19] F .Zernike. Phase Contrast, a New Method for the Microscopic Observations of Transparent Objects. *Physica*, 9:686–698,974–986, 1942.

[20] H. Presby, D. Finkelstein. Plasma Phasography. *The Review of Scientific Instruments*, 38(11):1563–1572, November 1967.

[21] H. Weisen. The Phase-Contrast Technique as an Imaging Diagnostic for Plasma Density Fluctuations. *Infrared Physics*, 25(3):543–549, 1985.

[22] H. Weisen. *The phase contrast method applied to the observation of density fluctuations in the TCA tokamak*. PhD thesis, Ecole Polytechnique Fédérale de Lausanne, Switzeland, December 1986.

[23] H. Weisen. Imaging Methods for the Observation of Plasma Density Fluctuations. *Plasma Physics and Controlled Fusion*, 28(8):1147–1159, 1986.

[24] H. Weisen, W. Simm, A. Pochelon, Ch. Hollenstein, R. Behn. Observation of Long Wavelength Turbulence in the TCA Tokamak. *Plasma Physics and Controlled Fusion*, 28(8):1161–1165, 1986.

[25] H. Weisen. The phase contrast method as an imaging diagnostic for plasma density fluctuations. *Review of Scientific Instruments*, 59(8):1544–1549, August 1988.

[26] Stefano Coda. *An Experimental Study of Turbulence by Phase-Contrast Imaging in the DIII-D Tokamak*. PhD thesis, Massachusetts Institute of Technology, 1997.

[27] S. Coda, M. Porkolab, T.N. Carlstrom. A phase contrast interferometer on DIII-D. *Review of Scientific Instruments*, 63(10):4974–4976, October 1992.

[28] S. Coda, M. Porkolab. Edge fluctuation measurement by phase contrast imaging on DIII-D. *Review of Scientific Instruments*, 66(1):454–456, January 1995.

[29] K. Matsuo, K. Tanaka, K. Muraoka. Development of Laser Imaging Method for Measurements of Electron Density Fluctuations in Plasmas. *Japanese Journal of Applied Physics*, 30(5):1102–1108, May 1991.

[30] K. Tanaka, K. Matsuo, S. Koda, M. Bowden, K. Muraoka, K. Kondo, T. Furukawa, F. Sano, H. Zushi, T. Mizuuchi, S. Besshou, H. Okada, K. Nagasaki, M. Wakatani, T. Obiki, S. Sudo. Characteristics of Electron Density Fluctuations in Heliotron-E Measured Using a Wide Beam Laser Phase Contrast Method. *Journal of the Physical Society of Japan*, 62(9):3092–3105, September 1993.

[31] R. Chatterjee, G.A. Hallock, M.L. Gartman. Phase contrast imaging system for TEXT-U. *Review of Scientific Instruments*, 66(1):457–459, January 1995.

[32] E. Lo, J. Wright, R. Nazikian. Linear systems description of the CO_2 laser-based tangential imaging system. *Review of Scientific Instruments*, 66(2):1180–1183, February 1995.

[33] A. Mazurenko. Fluctuations and Fast Wave measurements by the Phase Contrast Imaging on Alcator C-Mod. *Bulletin of the American Physical Society.*, 45(7):318, October 2000.

[34] M. Born, E. Wolf. *Principles of Optics*. The Macmillan Company, 1964.

[35] L.E. Sharp. The measurement of large-scale density fluctuations in toroidal plasmas from the "phase scintillation" of a probing electromagnetic wave. *Plasma Physics*, 25(7):781–792, 1983.

[36] U.Ascoli-Bartoli. Plasma diagnostics based on refractivity. In *Plasma Physics. Lectures Presented at the Seminar on Plasma Physics Organized by and Held at the International Centre for Theoretical Physics, Trieste from 5-31 October 1964*, pages 287–321. International Atomic Energy Agency, Vienna, 1965.

[37] R. Nazikian and L.E. Sharp. CO_2 laser scintillation interferometer for the measurement of density fluctuations in plasma confinement devices. *Review of Scientific Instruments*, 58(11):2086–2091, November 1987.

[38] R.E. Slusher and C.M. Surko. Study of density fluctuations in plasmas by small-angle CO_2 laser scattering. *Physics of Fluids*, 23(3):472–490, March 1980.

[39] E. Mazzucato. Small-Scale Density Fluctuations in the Adiabatic Toroidal Compressor. *Physical Review Letters*, 36(14):792–794, April 1976.

[40] E.U. Dereniak and D.G. Crowe. *Optical Radiation Detectors*. John Wiley & Sons, 1984.

[41] *American Institute of Physics Handbook*. McGraw-Hill Book Company, 3rd edition, 1972.

[42] *Handbook of Spectroscopy*. CRC Press, 1974.

[43] I.M. Ryzhik I.S. Gradshteyn. *Table of Integrals, Series, and Products*. Academic Press, 5th edition, 1994.

[44] X.Q. Xu, R.H. Cohen, G.D. Porter, T.D. Rognlien, D.D. Rytov, J.R. Myra, D.A. D'Ippolito, R.A. Moyer, R.J. Groebner. Turbulence Studies in Tokamak Boundary Plasmas with Realistic Divertor Geometry. *Nuclear Fusion*, 40(3Y):731–736, 2000.

[45] W. Suttrop. The physics of large and small edge localized modes. *Plasma Physics and Controlled Fusion*, 42:A1–A14, 2000.

[46] Yijun Lin. *Experimental Application and Numerical Study of Reflectometry in the Alcator C-Mod Tokamak*. PhD thesis, Massachusetts Institute of Technology, 2001.

[47] R.E. Slusher, C.M. Surko, J.F. Valley, T. Crowley, E. Mazzucato, K. McGuire. New Fluctuation Phenomena in the H-Mode Regime of Poloidal-Diverter Tokamak Plasmas. *Physical Review Letters*, 53(7):667–670, August 1984.

[48] J.R. Myra, D.A. D'Ippolito, X.Q. Xu, R.H. Cohen. Resistive X-point Modes in Tokamak Boundary Plasmas. *Physics of Plasmas*, 7(6):2290–2293, June 2000.

[49] J.R. Myra, D.A. D'Ippolito, X.Q. Xu, R.H. Cohen. Resistive Modes in the Edge and Scrape-off Layer of Diverted Tokamaks. *Physics of Plasmas*, 7(11):4622–4631, November 2000.

[50] J.P. Freidberg. *Ideal Magnetohydrodynamics*. Plenum Press, 1987.

[51] L.L. Lao, H.St. John, R.D. Stambaugh, A.G. Kellman, W. Pfeiffer. Reconstruction of Current Profile Parameters and Plasma Shapes in Tokamaks. *Nuclear Fusion*, 25(11):1611–1622, November 1985.

[52] Y. Lin, J.H. Irby, R. Nazikian, E.S. Marmar, A. Mazurenko. Two-dimensional full-wave simulation of microwave reflectometry on Alcator C-Mod. *Review of Scientific Instruments*, 72(1):344–37, January 2001.

[53] I.H. Hutchinson, J.E. Rice, R.S. Granetz, J.A. Snipes. Self-Acceleration of a Tokamak Plasma duriing Ohmic H-Mode. *Physical Review Letters*, 84(15):3330–3333, April 2000.

[54] T. Sunn Pedersen, R.S. Granetz, A.E. Hubbard, I.H. Hutchinson, E.S. Marmar, J.E. Rice, J. Terry. Radial impurity transport in the H-mode transport barrier region in Alcator C-Mod. *Nuclear Fusion*, 40(10):1795–1804, October 2000.

[55] A. Mazurenko, M. Porkolab, X.Q. Xu, W.M. Nevins. On the Physics of Quasi-Coherent Fluctuations in High Density Tokamak Plasma. *Physical Review Letters*, to be submitted, 2001.

[56] X.Q. Xu, R.H. Cohen, T.D. Rognlien, J.R. Myra. Low-to-High Confinement Tranition Simulations in Divertor Geometry. *Physics of Plasmas*, 7(5):1951–1958, May 2000.

[57] O. Sauter, C. Angioni, Y.R. Lin-Liu. Neoclassical conductivity and bootstrap current formulas for general axisymmetric equilibria and arbitrary collisionality regime. *Physics of Plasmas*, 6(7):2834–2839, July 1999.

[58] D. Mossessian, A.E. Hubbard, E.S. Marmar, T. Sunn Pedersen, et al. Measurements and Scalings of the H-mode pedestal on Alcator C-Mod. *Plasma Physics and Controlled Fusion*, 42:A255–A262, 2000.

[59] I.H. Hutchinson, R.S. Granetz, A. Hubbard, J.A. Snipes, T. Sunn Pedersen, M. Greenwald, B. LaBombard and the Alcator Group. Edge transport barrier phenomena in Alcator C-Mod. *Plasma Physics and Controlled Fusion*, 41:A609–A616, 1999.

[60] T.H. Stix. *Waves in Plasmas*. American Institute of Physics, 1992.

[61] T.H. Stix. *The Theory of Plasma Waves*. McGraw-Hill, 1962.

[62] M. Brambilla. *A Full Wave Code for Ion Cyclotron Waves in Toroidal Plasmas*. Max-Plank-Institut Fur Plasmaphysik, 1996.

[63] Chris Rost. *Fast Ion Tails during Radio Frequency Heating on the Alcator C-Mod Tokamak*. PhD thesis, Massachusetts Institute of Technology, 1998.

[64] Y. Takase, J.D. Moody, C.L. Fiore, F.S. McDermott, M. Porkolab and J. Squire. Study of Directly Launched Ion Bernstein Waves in a Tokamak. *Physical Review Letters*, 59(11):1201–1204, September 1987.

[65] J.H. Lee, W.A. Peebles et al. Internal Electric Field Structure of Launched Fast Magnetosonic Waves in the DIII-D Tokamak. *Physical Review Letters*, 80(11):2330–2333, March 1998.

[66] K. Ida, M. Naito, S. Shinohara, K. Miyamoto. Direct measurements of fast magnetosonic wave near the ion-ion hybrid resonance layer by magnetic probes. *Nuclear Fusion*, 23(9):1259–1262, September 1983.

[67] C.L. Fiore, J.E. Rice et al. Internal transport barriers on Alcator C-Mod. *Physics of Plasmas*, 8(5):2023–2028, May 2001.